Spectral-domain optical coherence phase microscopy for quantitative biological studies

by

Chulmin Joo

Submitted to the Department of Mechanical Engineering
in partial fulfillment of the requirements for the degree of
Doctor of Philosophy in Mechanical Engineering
at the
MASSACHUSETTS INSTITUTE OF TECHNOLOGY
February 2008

Author..
Department of Mechanical Engineering
September 6, 2007

Certified by..
Johannes F. de Boer
Associate Professor of Dermatology, Harvard Medical School
Thesis Supervisor

Certified by..
Peter T. C. So
Professor of Mechanical and Biological Engineering
Thesis Committee Chairman

Accepted by..
Lallit Anand
Professor of Mechanical Engineering
Chairman, Departmental Committee on Graduate Students

Spectral domain optical coherence phase microscopy for quantitative biological studies

by

Chulmin Joo

Submitted to the Department of Mechanical Engineering on September 6, 2007
in partial fulfillment of the requirements for the degree of Doctor of Philosophy
in Mechanical Engineering

Abstract

Conventional phase-contrast and differential interference contrast microscopy produce high contrast images of transparent specimens such as cells. However, they do not provide quantitative information or do not have enough sensitivity to detect nanometer-level structural alterations. We have developed spectral-domain optical coherence phase microscopy (SD-OCPM) for highly sensitive quantitative phase imaging in 3D. This technique employs common-path spectral-domain optical coherence reflectometry to produce depth-resolved reflectance and quantitative phase images with high phase stability. The phase sensitivity of SD-OCPM was measured as nanometer-level for cellular specimens, demonstrating the capability for detecting small structural variation within the specimens. We applied SD-OCPM to the studies of intracellular dynamics in living cells and the detection of molecular interactions on activated surfaces as a sensor application.

In the study of intracellular dynamics, we measured fluctuation of localized field-based dynamic light scattering within cellular specimens. With its high sensitivity to amplitude and phase fluctuations, SD-OCPM could observe the existence of two different regimes in intracellular dynamics. We also investigated the effect of an anti-cancer drug, Colchicine and ATP-depletion on the intracellular dynamics of human ovarian cancer cells, and observed the modification in diffusion characteristics inside the cells. Based on the optical sectioning capability of SD-OCPM, quantitative phase imaging was performed to examine slow dynamics of living cells. Through time-lapsed imaging and spectral analysis on the dynamics at the vicinity of cell membrane, we observed the existence of dynamic and independent sub-domains inside the cells that fluctuate at various dominant frequencies with different frequency contents and magnitudes.

SD-OCPM was further utilized to measure molecular interactions on activated sensor surfaces. The method is based on the fact that phase varies as analyte molecules bind to the immobilized probe molecules at the sensing surface and SD-OCPM can measure small phase alteration at any surface with high sensitivity. We have measured a ~1.3 nm increase in optical thickness due to the binding of streptavidin on a biotin-activated substrate in a micro-fluidic device. Moreover, SD-OCPM was extended to image protein array chips, demonstrating its potential as a multiplexed protein array scanner.

Thesis supervisor: Johannes F. de Boer
Title: Associate Professor, Harvard Medical School,
Member of the Faculty of the Harvard-MIT Division of Health Sciences and Technology
Wellman Center for Photomedicine, Massachusetts General Hospital

Acknowledgements

It is my fortune to have Prof. Johannes F. de Boer as my thesis supervisor. I would like to thank him for giving me chance to conduct my thesis work at the great and inspiring environment he established. Besides his encouragement and support, I am most grateful to his passion, patience, and time.

Professors Peter So, Gary Tearney, and George Barbastathis generously took a role of my thesis committee and shared their expertise with valuable suggestions and questions. Their comments and questions helped me improve the quality of this thesis.

Working as a graduate research assistant at Wellman Center for Photomedicine, I have been very lucky to meet and work with not only great colleagues but also dear friends. I spent one year with a good mentor and friend of mine, Prof. Taner Akkin. He was generous in sharing his expertise in fiber optic instrumentation. Chatting with Dr. Micrea Mujat on the matters regarding research as well as family was always delightful and didactic. Dr. B Hyle Park is a respectable friend in many aspects. Besides his invincible knowledge on OCT, his personality and leadership attract people and make his desk crowded all the time. Dr. Ki Hean Kim would be the person that one would go first to discuss about microscopy instrumentation. His presence was a relief for me during SD-OCPM development. It was a pleasure sharing the office with Dr. Charles Kerbage. I would like to thank him for his red pen that makes this thesis more readable. Dr. Conor Evans is already marking his fingers on SD-OCPM, and Wei Sun is taking a closer step to a PhD. I learnt a lot from the *ad hoc* discussions with Drs. Alberto Bilenca and Reza Motaghian. Life at Wellman was more pleasant because of the presence of Alyx Chau, Brian Goldberg, and Alt Clement.

I had many collaborators to thank as well. Dr. Thomas Stepinac and Prof. Tayyaba Hasan provided incessant support for our work, and were available to give us a hand in cell preparation. From Japan, Dr. Keiji Itaka gave us a chance to work with his gene delivery agents. Prof. Selim Unlu and Emre Ozkumur provided us with beautiful silicon oxide and protein chip for our sensor application.

I also appreciate the encouragement and support by KGSAME members and KAIST alumni at MIT – especially, Euiheon Chung, Soon-Jo Chung, Eun Suk Suh, Yoonsun Chung, Juhyun Park, Junsang Doh, Jae Jeen Choi, and Hyungsuk Lee. Thanks to them, my graduate life at MIT was just great.

On a more personal note, I cannot thank enough to my wife, Mihwa Lee. Mihwa has given me the courage and motivation to get through the obstacles and frustration. Without her unconditional love, support, and encouragement, I would not be able to finish this thesis. Thank you for being there with me all this time. My son, Luke, is such a great gift to us from God, and through his eyes, I am always amazed by how wonderful life can be. Lastly, but mostly, I am eternally grateful to my parents for a lifetime of love and support. To them, I wish to dedicate my dissertation.

The work documented in this thesis was supported in part by Wellman Graduate Program, Hatsopoulos Innovation Award, research grants from National Institute of Health (R01 RR19768, EY14975), the U.S. Department of Defense (F4 9620-01-1-0014), and the Center for Integration of medicine and Innovative Technology.

TABLE OF CONTENTS

LIST OF FIGURES

Chapter 1:
Introduction

1.1. Optical microscopy for cellular imaging

Cells are complicated structural and functional units for all living organisms, and the visualization of their morphological structures and dynamics *in vitro* and *in vivo* is of great importance to understand their functions and roles in life [1]. These creatures, however, become problematic for visualization because they are optically transparent and small on the order of tens of microns, exhibiting extra- and intra-cellular dynamics down to the nanometer range. In order to observe and understand their morphology and functions, cellular imaging methods are therefore required to have enough resolution, contrast, and sensitivity to unveil the secrets of these small and profound living units.

Optical microscopy is an imaging technique widely employed for observation of cellular specimens, which are often stained with dyes for visualization. As light waves traverse a stained cellular specimen, the localized pigment absorbs some of the light, and the amplitude of the light wave emerging from specific regions of the specimen is thus altered relative to the background or medium. This modulation enables visualization by the human eye or detectors, and the differences in amplitude offer a contrast for visualization.

With respect to imaging cellular structures with specificity, it is common to introduce exogenous fluorescent molecules to tag the structures of interest. The fluorescent molecules transit to the excited molecular state by absorbing the excitation laser beam, and generate fluorescence emission light as they decay back to the ground state. Detecting this emission, one can visualize the distribution of particular structures of interest inside the cells. The development of 3D fluorescence imaging techniques such as confocal [2] and multiphoton microscopy [3] has enabled 3D section view of the cellular specimen, opening up exciting chances to observe morphological changes in 3D.

Optical microscopic techniques based on exogenous stains and fluorescent labeling together with the development of various fluorophores have advanced remarkably over the past decades. They have found numerous applications in biological and medicine mainly because of their ability to generate high-resolution and high-contrast images. Major disadvantage of the current methods, though, is that they require the specimen to be labeled, which is time-consuming and may influence the dynamics of the specimen of interest.

For unstained and unlabeled cellular structures, there is little change in the amplitude of the light as the light traverses the specimen, since the unlabeled specimen does not have substantial absorption properties in the visible wavelengths usually employed for microscopy. A lack of amplitude modulating structure renders the sample translucent and morphology difficult to discern. However, light propagating through a translucent sample is altered relative to surrounding medium *in phase*.

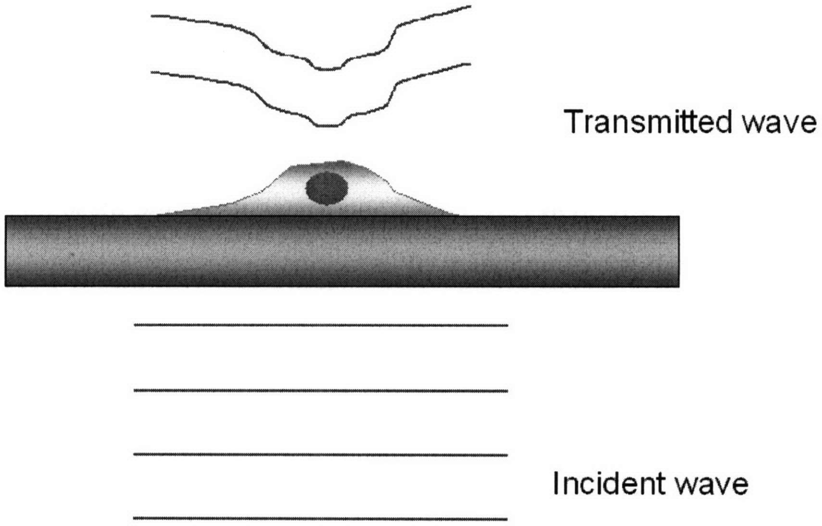

Figure 1.1: Incident 'in-phase' wave is altered by passing through the cellular specimen, generating phase variation in the transmitted wave.

Such an alteration in phase is termed phase shift or phase delay, and it simply reflects the extent to which light wave propagation is slowed down by passage through the sample. Waves passing through a thick sample will be slowed to a greater degree than those passing through a thin sample. This effect is illustrated in Figure 1. Incident light waves are initially 'in phase', and as sample regions of different thickness and refractive index influence the passage of light, a variable degree of phase shift is induced. The extent to which the emergent wave becomes 'out of phase' with each other is termed the relative phase shift and is measured in radians. Unlike the amplitude variations, differences in phase cannot be perceived by the eye or by photographic film, and so our desire to visualize this phase difference led to the development of various optical phase microscopes.

1.2. Optical phase microscopy

Over the past decades, the development of various optical phase microscopes has been sought to visualize transparent cellular specimens without staining. In effect, the phase contrast technique employs an optical mechanism to translate minute variations in phase into corresponding changes in amplitude, which can be visualized as differences in image contrast. Different forms of optical phase microscopy utilize various optical schemes that change the way light is refracted and transmitted, and these have served for many years as useful tools for examination of live cells.

Zernike phase microscopy

The well-known and more widely applied optical phase microscopic method is Zernike phase microscopy, or phase-contrast microscopy (PCM) [4]. Frits Zernike discovered the concept of phase contrast microscope even before the invention of the laser, and indeed, his contribution was recognized by the Nobel Prize in physics in 1953.

This form of microscopy forms images by phase-shifting the light field scattered from the specimen and interfering it with the unscattered field. The phase shift between scattered and unscattered light fields is typically introduced by rings etched accurately onto glass plates so that they introduce the required phase shift when inserted into the optical path of the microscope. When these components reach the image plane, they interfere accordingly, and so variations in the phase of scattered transmitted light from the sample plane are traslated into intensity variations.

Phase contrast microscopy is able to render subcellular structrues visible without staining. However, it can be only applied to specimens that scatter a significant amount of light, and generates the appearance of light halos at the edge of the specimen components where the phase shift gradient is most steep.

Differential interference contrast

Differential interference contrast (DIC) microscopy was invented in the 1950's by the French optical theoretician, George Normarski [5]. It forms images by splitting and interfering of incident light waves, which traverse different regions of the sample. The typical equipment needed for DIC microscopy includes a polarizer, a beam-splitting modified Wollason prism below the condenser, and another prism above the objective, and an analyzer above the upper prism. The prisms allow for splitting of the incident light in the optical path before reaching the specimen and re-combination of the separated beams beyond the specimen. As a result, the paths of the parallel beams are of unequal length and when re-combined give constructive and destructive interference in each location, resulting in the differences in intensity to be discern. Under DIC conditions, one side of the specimen appears bright while the other side appears dark, conferring a three-dimensional 'shadow relief' appearance.

A major advantage of DIC is that it permits focus in the thin plane section of a thick specimen, with reduced contributions from specimen regions above or below the planes of focus. This DIC provides superior resolution to Zernike phase contrast microscopy. Unfortunately, DIC is highly sophisticated, expensive to set up due to the cost of the accessory optical components, and requires significant expertise to operate. These reasons prevented the method from supplanting phase-contrast microscopy as the cell biologist tool of choice for examining unstained microscope sections.

1.3. Quantitative phase contrast microscopy

It is important to emphasize that the optical phase imaging techniques summarized above, while very useful in many different observational and imaging situations, generally only provide qualitative information about cellular morphology and dynamics. Elaborate and detailed study on cellular structures and dynamics requires quantitative knowledge, and various innovative approaches to quantitative phase imaging have been pursued. In this Section, a few of the state-of-art quantitative phase image techniques are reviewed.

Quantitative phase-amplitude microscopy

Quantitative phase-amplitude microscopy (QPM) [6, 7] is based on mathematically derived information about specimen phase modulating characteristics. It combines the useful qualitative attributes of previous phase imaging approaches with the additional advantage of quantitative representation of specimen phase parameters. The implementation of QPM involves the calculation of a phase map from a triplicate set of images captured under standard bright field microscopy. A computational algorithm is applied to the analysis of an in-focus image and a pair of equidistant positive and negative de-focus images. The mathematical processes involved have been described in detail elsewhere [7], but essentially the procedure entails calculation of the rate of change of light intensity ("transport of intensity" equation) between the three images in order to determine the phase shift induced by the specimen. Both the image acquisition and the computational processes for QPM can be performed by commercially available hardware and software (QPm software).

Digital holographic phase microscopy

Digital holographic phase microscopy (DPHM) is one of the most established techniques for quantitative phase imaging. It is based on the holographic surface profiling for reflective surfaces in metrology except that the hologram is recorded by a digital image sensor e.g., CCD or CMOS camera, and the subsequent reconstruction of object wave is carried out numerically by a computer [8]. In general, the hologram is the interference between scattered light from the specimen and the reference plane wave recorded at the Fourier plane. To reconstruct the information of the object wave, the reference wave is numerically assumed based on the experimental setup, and the reconstruction methods (typically with the Fresnel-transformation) generate not only the information contained in the object but also the intensity of the reference wave and a "twin image".

Advantages of DPHM are its simple geometry to set up and the single-shot nature, which makes the system stable and fast. The acquisition speed is limited to the exposure time of the recording device. However, it is computationally expensive and the accuracy of the object wave is highly dependent on the numerically approximated reference wavefront.

Fourier phase microscopy

Fourier phase microscopy demonstrated by Popescu *et. al.* [9], is similar to the implementation of PCM except that it uses a programmable phase modulator in the Fourier plane to introduce phase differences between scattered and unscattered light waves by the specimen. For quantitative phase determination, it records four interferograms with different phase differences, and obtains the phase distribution of the sample as in phase-shifting interferometry:

$$\tan\Delta\phi = \frac{I_3 - I_1}{I_0 - I_2} \tag{1.1}$$

where

$$I_n = I_r + I_s + 2\sqrt{I_r I_s}\cos(\Delta\phi + n\pi/2) \tag{1.2}$$

FPM is also a full-field imaging technique, so it has high phase stability. However, it requires a sophisticated device for phase modulation, and necessitates at least four interferograms for phase determination.

Hilbert phase microscopy

Ikeda and Popescu *et. al.* also developed a phase imaging technique referred to as Hilbert phase microscopy [10]. It is similar to DPHM, but it permits direct observation of the specimen because the interference signal is detected at the image plane. In order to obtain quantitative phase information, HPM utilizes the Fourier fringe analysis in two-dimensional space reported in Ref. [11]. Basically, the tilt of the reference wave provides a carrier spatial frequency, which enables the measurement of the amplitude and phase information in the spatial frequency domain.

Compared to their earlier method, Fourier phase microscopy, HPM is faster due to its "single shot" nature, but requires external phase stabilizer because of the separate reference and measurement beam paths.

The efforts for the development of novel quantitative phase imaging modalities are still underway. All those techniques have their own attractive features in terms of sensitivity and speed of acquisition. However, most of the above-mentioned methods are based on the light transmitted through the specimen, and measure phase distribution accumulated through the specimen. Therefore, the images do not provide the information about the incremental phase delay between arbitrary section planes inside the sample.

1.4. Optical coherence tomography and quantitative phase contrast imaging

Optical coherence tomography (OCT) is a highly sensitive non-invasive imaging technique capable of measuring the information of light back-scatttered from biological specimen [12]. With high lateral (10-30 μm) and axial (1-10 μm) resolution, OCT enables depth-resolved cross sectional *in vivo* imaging of tissue morphology. The depth range (typically 1-2 mm in skin) depends on the absorption and scattering characteristics of the tissue specimen, and the axial resolution is determined by the coherence gate, which is inversely proportional to the bandwidth of the source.

About a decade ago, Fercher [13] noticed that the same measurement can be performed by measuring the spectrally dispersed interference signal between sample and reference light, which is referred to as Spectral/Fourier-domain OCT. Spectral-domain OCT (SD-OCT) is identical to conventional time-domain OCT (TD-OCT) except that it obtains depth-resolved reflectance by taking an inverse Fourier transformation of spectrally dispersed interference signals. The development of SD-OCT [14] has demonstrated improved mechanical stability and acquisition speed compared to TD-OCT techniques mainly due to the absence of mechanical scanning during the measurement.

With the development of OCT, numerous researchers in the OCT community have explored the intrinsic phase information in the OCT interferogram for various functional extensions such as polarization-sensitive OCT [15, 16] and Doppler OCT [14, 17, 18]. Among those efforts, the use of phase information to produce quantitative phase-contrast images formed one stream, noting a great potential for visualization of structures and dynamics of thin biological specimen. Hitzenberger [19] pioneered this area by demonstrating depth-resolved differential phase contrast imaging, and later observation of the sub-wavelength optical path-length distribution of the cellular structures were reported with time-domain OCT systems [7, 20, 21]. Yang *et. al.* also proposed to use harmonically related light sources to generate phase dispersion images of transparent specimens [22].

Even though OCT provides depth-resolved phase information, the phase imaging of cellular specimen has been limited to 2D imaging. In fact, Hitzenberger [19] and Yang [23] demonstrated the exciting possibility of 3D phase imaging in their early works, but were limited to material inspection.

1.5. Statement of work

This dissertation describes our efforts to realize quantitative 3D phase imaging modality by use of the state-of-art SD-OCT technology, and to explore its opportunity to the quantitative biological studies. The technology is termed spectral domain optical coherence phase microscopy (SD-OCPM).

Conceptually, SD-OCPM is the functional extension of SD-OCT, where depth-resolved phase information is acquired along the optical axis to generate 3D phase contrast images. By use of combined coherence and confocal gates, SD-OCPM offers optical sectioning capability with high spatial resolution, where the phase information at the focal volume can be examined through the SD-OCT depth scan. Therefore, the phase differences in a three-dimensional space can be drawn by scanning a beam in volume and taking difference of the phase maps of any section planes in depth.

This dissertation is organized mainly in three parts: implementation, analysis, and applications of SD-OCPM to quantitative biological studies.

Detailed description on the principle of operation and implementation of SD-OCPM is described in Chapter 2. The method on the amplitude and phase retrieval from SD-OCT interferograms, in addition to the details on the hardware and software are discussed. We also present the performance characteristics such as spatial resolution and phase stability, along with the quantitative phase images obtained on calibrated phase object and biological specimen.

The development of SD-OCPM will be followed by detailed discussion on the noise sources in SD-OCPM (Chapter 3). Two kinds of noise sources will be discussed: the noise in the SD-OCPM detection and the external disturbance caused by the lateral and axial scanners. We also show that the phase stability is described as a function of the signal-to-noise ratio, and demonstrate the agreement between the theory and the experiments.

In Chapter 4, we describe a new multi-modal imaging technique by integrating multi-photon fluorescence microscopy (MPM) into SD-OCPM. This work was motivated to facilitate understanding of the information content provided by the SD-OCPM phase images. As in Chapter 2, the details on the implementation and performance characteristics for MPM are presented, and simultaneous imaging capability is demonstrated by presenting images obtained on fluorescently labeled cells.

Chapter 5 and 6 are devoted to the applications of SD-OCPM to cellular and molecular biology. In Chapter 5, we describe the application of SD-OCPM for cellular dynamics investigation. We first demonstrate the use of SD-OCPM to measure mechanical properties of the intracellular environment by use of a fast point detection scheme. We show the existence of active transport in living cells, and the change of mechanical properties of cells in different physiological situations. Later, we explore the 3D imaging capability of SD-OCPM by examining phase images of the top surface and inside of living cells. Using the spectral analysis, we quantify the slow dynamics of living cells.

The potential of SD-OCPM as a novel molecular sensing platform is described in Chapter 6. Owing to its high phase sensitivity and its ability to identify a sensor surface of interest selectively, SD-OCPM enables highly sensitive detection of molecular interaction. Various experiments conducted to demonstrate the feasibility of SD-OCPM molecular sensor will be presented.

In the last Chapter, we conclude this dissertation by a summary of the achievements and comments on the future directions and applications of SD-OCPM.

1.6. Reference

1. W.K. Purves, D. Sadava, G.H. Orians, and H.C. Heller, *Life: The Science of Biology*. 7 ed. 2004, Sunderland: Sinauer Associates, Inc.

2. J.B. Pawley, *Handbook of Biological Confocal Microscopy*. 3 ed. 2006, Berlin: Springer.

3. W. Denk, J.H. Strickler, and W.W. Webb, "*Two-photon laser scanning fluorescence microscopy,*" Science. **248,** 73-76 (1990).

4. F. Zernike, "*How I discovered phase contrast,*" Science. **121,** 345-349 (1955).

5. K.F.A. Ross, *Phase contrast and interference microscopy for cell biologists*. 1967, New York: St. Martin's Press.

6. A. Barty, K.A. Nugent, D. Paganin, and A. Roberts, "*Quantitative optical phase microscopy,*" Optics Letters. **23,** 817-819 (1998).

7. D. Paganin and K.A. Nugent, "*Noninterferometric phase imaging with partially coherent light* " Physical Review Letters. **80,** 2586-2589 (1998).

8. E. Cuche, F. Bevilacqua, and C. Depeursinge, "*Digital holography for quantitative phase-contrast imaging,*" Optics Letters. **24,** 291-293 (1999).

9. G. Popescu, L.P. Deflores, J.C. Vaughan, K. Badizadegan, H. Iwai, R.R. Dasari, and M.S. Feld, "*Fourier phase microscopy for investigation of biological structures and dynamics,*" Optics Letters. **29,** 2503-2505 (2004).

10. T. Ikeda, G. Popescu, R.R. Dasari, and M.S. Feld, "*Hilbert phase microscopy for investigating fast dynamics in transparent systems,*" Optics Letters. **30,** 1165-1167 (2005).

11. S. Kostianovski, S.G. Lipson, and E.N. Ribak, "*Interference microscopy and Fourier fringe analysis applied to measuring the spatial refractive-index distribution,*" Applied Optics. **32,** 4744-4750 (1993).

12. D. Huang, E.A. Swanson, C.P. Lin, J.S. Schuman, W.G. Stinson, W. Chang, M.R. Hee, T. Flotte, K. Gregory, C.A. Puliafito, and J.G. Fujimoto, "*Optical coherence tomography,*" Science. **254,** 1178-1181 (1991).

13. A.F. Fercher, C.K. Hitzenberger, G. Kamp, and S.Y. El-Zaiat, "*Measurement of intraocular distances by backscattering spectral interferometry,*" Optics Communications. **117,** 43-48 (1995).

14. B. White, M. Pierce, N. Nassif, B. Cense, B. Park, G. Tearney, B. Bouma, T. Chen, and J.F. de Boer, "*In vivo dynamic human retinal blood flow imaging using ultra-high-speed spectral domain optical coherence tomography,*" Optics Express. **11,** 3490-3497 (2003).

15. J.F.de Boer, T.E. Milner, M.J.C.v. Gemert, and J.S. Nelson, "*Two-dimensional birefringence imaging in biological tissue by polarization-sensitive optical coherence tomography,*" Optics Letters. **22,** 934-936 (1997).

16. J.F.de Boer, T.E. Milner, and J.S. Nelson, "*Determination of the depth-resolved Stokes parameters of light backscattered from turbid media by use of polarization-sensitive optical coherence tomography,*" Optics Letters. **24,** 300-302 (1999).

17. Z. Chen, T.E. Milner, S. Srinivas, X. Wang, A. Malekafzali, M.J.C.v. Gemert, and J.S. Nelson, "*Noninvasive imaging of in vivo blood flow velocity using optical Doppler tomography,*" Optics Letters. **22,** 1119-1121 (1997).

18. S. Yazdanfar, A.M. Rollins, and J.A. Izatt, "*Imaging and velocimetry of the human retinal circulation with color Doppler optical coherence tomography,*" Optics Letters. **25,** 1448-1450 (2000).

19. C.K. Hitzenberger and A.F. Fercher, "*Differential phase contrast in optical coherence tomography,*" Optics Letters. **24,** 622-624 (1999).

20. M. Sticker, M. Pircher, E. Götzinger, H. Sattmann, A.F. Fercher, and C.K. Hitzenberger, "*En face imaging of single cell layers by differential phase-contrast optical coherence microscopy,*" Optics Letters. **27,** 1126-1128 (2002).

21. C.G. Rylander, D.P. Davé, T. Akkin, T.E. Milner, K.R. Diller, and A.J. Welch, "*Quantitative phase-contrast imaging of cells with phase-sensitive optical coherence microscopy,*" Optics Letters. **29,** 1509-1511 (2004).

22. C. Yang, A. Wax, I. Georgakoudi, E.B. Hanlon, K. Badizadegan, R.R. Dasari, and M.S. Feld, "*Interferometric phase-dispersion microscopy,*" Optics Letters. **25,** 1526-1528 (2000).

23. C. Yang, A. Wax, R.R. Dasari, and M.S. Feld, "*Phase-dispersion optical tomography,*" Optics Letters. **26,** 686-688 (2001).

Chapter 2:

Spectral-domain optical coherence phase microscopy

2.1. Introduction

Spectral-domain optical coherence phase microscopy (SD-OCPM) is an interferometric microscopy technique based on a fiber-based common-path SD-OCT interferometer. The common-path topology enables us to achieve nanometer-level phase sensitivity for biological specimen investigation. In this Chapter, the basic principle and the implementation of SD-OCPM will be described. The performance characteristics such as spatial resolution and phase stability will be presented, followed by the demonstration of SD-OCPM imaging capability on a calibrated phase target and various cellular specimens.

2.2. Principle of SD-OCPM

1.1.1. SD-OCT

The basic principle of SD-OCPM is identical to that of SD-OCT. For detailed information on the theory and implementation of SD-OCT, one is referred to Refs. [1, 2].

Briefly, the SD-OCT is based on a low-coherence spectral interferometer [3] in which interference of reference and measurement light is spectrally dispersed, detected, and converted into the depth-resolved information of a specimen. Consider a simple Michelson interferometer illuminated by a broadband light source (Figure 1). After the division of the light beam at the beamsplitter, the light reflected from the reference mirror and the sample structures combine and interfere, and the spectrometer at the detection arm measures spectrally dispersed interference at each wave number, k. The measured spectrum, $P(k)$, can be described as:

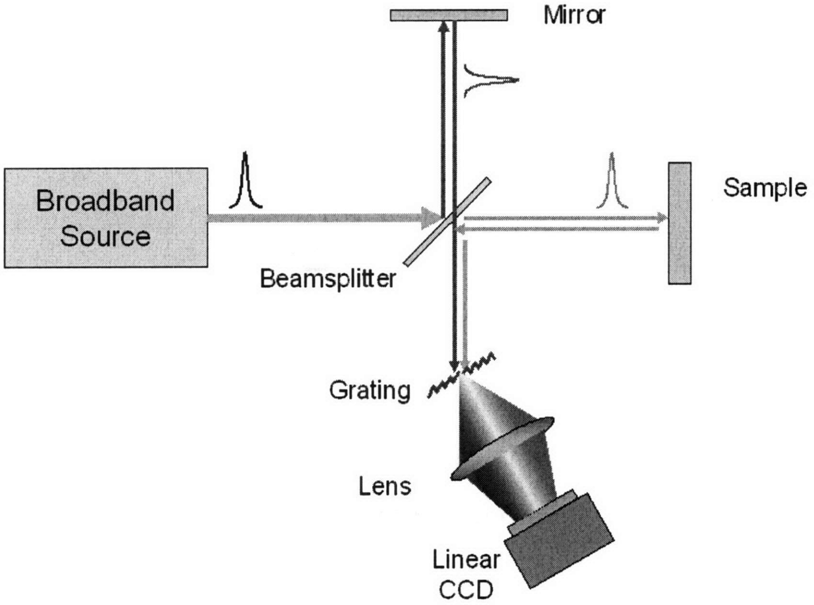

Figure 2.1: Basic schematic of a typical SD-OCT interferometer. Broadband light source illuminates a Michelson interferometer, and the interference between back-reflected beams from a reference mirror and sample is spectrally separated and measured by linear CCD detector.

$$P(k) = P_r(k) + \sum_n P_{s,n}(k) + 2\sqrt{P_r(k)}\sum_n \sqrt{P_{s,n}(k)}\cos(2k\Delta p_n) \qquad (2.1)$$

where $P_r(k)$ and $P_{s,n}(k)$ are the k-dependent powers reflected from the reference and sample, respectively. The third term on the right hand side of Eqn. (2.1) represents the interference of the reflected beams from the reference and specimen surfaces at an optical path-length difference, Δp_n. For simplicity, we define the reflectance of the reference and sample surfaces as $|r_R|^2 \equiv P_r(k)/S(k)$ and $|r_{S,n}|^2 \equiv P_{S,n}(k)/S(k)$, respectively, with source power spectral density function, $S(k)$. Eqn. (2.1) then becomes:

$$P(k) = S(k)\left[|r_R|^2 + \sum_n |r_{S,n}|^2 + 2|r_R|\sum_n |r_{S,n}|\cos(2k\Delta p_n)\right]. \tag{2.2}$$

A complex-valued depth-resolved information, $F(z)$, is obtained by taking an inverse Fourier transform of the spectral interferogram with respect to $2k$, which is given by

$$\begin{aligned} F(z) &= \Gamma(z) \otimes \left\{ \left(|r_R|^2 + \sum_n |r_{S,n}|^2\right)\delta(z) + r_R\sum_n r_{S,n}^{*}\delta(z - z_n) + r_R^{*}\sum_n r_{S,n}\delta(z + z_n) \right\} \\ &= \left(|r_R|^2 + \sum_n |r_{S,n}|^2\right)\Gamma(z) + r_R\sum_n r_{S,n}^{*}\Gamma(z - z_n) + r_R^{*}\sum_n r_{S,n}\Gamma(z + z_n) \end{aligned}. \tag{2.3}$$

The first term in the braces on the right hand side describes the autocorrelation (or self-interference) of the reference and sample reflections, and the second and third terms are due to the interference of the back-reflected beams from reference and sample surfaces and its complex conjugates. $\Gamma(z)$ is referred to as the complex coherence function, directly related to the inverse Fourier transform of the source spectrum, $S(k)$. For a Gaussian source centered at k_0 with a full width at half maximum (FWHM) bandwidth Δk, the complex coherence function is given by [1, 4]

$$\Gamma(z) \propto e^{i2k_0 z} e^{-4\ln 2 (z/\Delta z)^2} \tag{2.4}$$

and the coherence gate, Δz, defined by the FWHM of $\Gamma(z)$ is evaluated as

$$\Delta z = \frac{2\ln 2}{\pi}\frac{\lambda_0^2}{\Delta\lambda}. \tag{2.5}$$

Figure 2.2 shows an example of depth-resolved reflectance map measured with a coverslip placed in the sample arm. The two high peaks, 1 and 2, account for the interference between the reference and back-reflected beams from the front and back surfaces of the glass slide, respectively. The peak 3 is due to the interference between the reflections from the front and back surfaces.

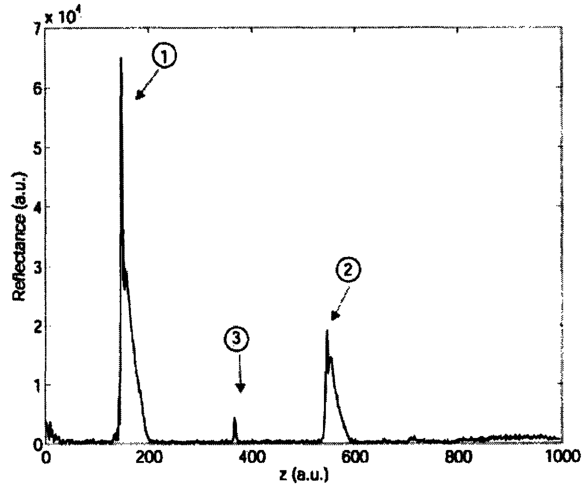

Figure 2.2: Measured reflectance of a cover glass. Two high peaks represent the front and back reflective surfaces in the sample, respectively.

1.1.2. SD-OCPM imaging method

Unlike typical SD-OCT imaging, SD-OCPM employs a common-path SD-OCT interferometer in which the beam reflected from a surface in the sample arm is used as a phase reference. Such a common path interferometer has superior rejection of common mode phase noise compared to the conventional interferometer setup where reference and measurement arms are separate. Figure 2.3 depicts a typical imaging method for cellular specimen where the reflection from the bottom surface of a coverslip serves as a phase reference, whereas the measurement beam is scattered from the focal volume inside the specimen. Since the thickness of the coverslip is larger than that of the cellular monolayer (< 50 μm), the interference signal referenced to the bottom surface of the coverslip can be distinguished from those referenced to other surfaces in the depth-resolved reflectivity map. The depth-resolved phase can then be evaluated as

$$\Delta\phi(z)\Big|_{(x,y)} = \tan^{-1}\left[\frac{\mathrm{Im}(F(z))}{\mathrm{Re}(F(z))}\right]_{(x,y)} . \tag{2.6}$$

Measurements of intensity and phase are performed as the beam scans in 2D or 3D space across the specimen, and the images at a sectioning plane of z are determined by the physical properties (physical size and the refractive index) and the dynamics of scatterers inside the focal volume.

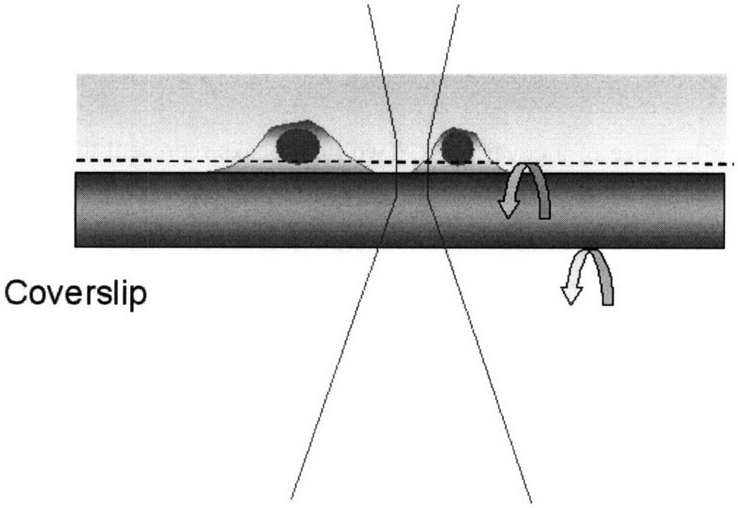

Figure 2.3: SD-OCPM imaging scheme. SD-OCPM employs a common mode SD-OCT interferometer where the reflection from the bottom surface of a coverslip serves as a phase reference, whereas the scattered waves from the focal volume is the measurement beam.

2.3. SD-OCPM experimental setup: hardware

1.1.3. SD-OCPM interferometer

The SD-OCPM interferometer setup is depicted in Figure 2.4. A broadband light source (superluminescent diode laser or Ti:Sapphire mode-locked laser) illuminates a single-mode fiber-based 2×2 coupler (Corning flexcore 780 fiber, AC Photonics, Inc.), of which the reference arm is not used for SD-OCPM imaging. The light coupled to the sample arm is delivered to the specimen via an integrated laser-scanning microscope, and the back-reflected beams are re-coupled to the fiber and measured by a custom-built spectrometer in the detection arm.

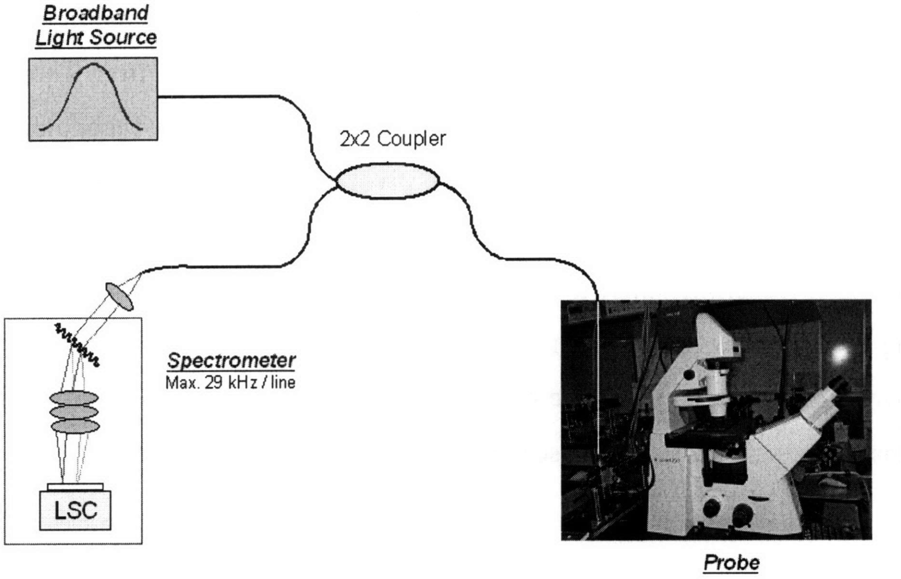

Figure 2.4: Schematic for SD-OCPM interferometer. A broadband light source illuminates a fiber-based common-path interferometer. The light coupled to the sample arm is delivered to specimen via an integrated inverted microscope, and the backscattered waves are re-coupled to the fiber interferometer for the subsequent interference spectrum measurement at the detection arm. LSC: line scan camera.

1.1.4. SD-OCPM probe arm

Microscope setup

An inverted microscope (Axiovert 200, Zeiss) is integrated as a probe at the sample arm (Figure 2.5). The beam emitted from the fiber is collimated by the collimator (C) with a $1/e^2$ diameter of ~3.4 mm, and passes through the XY beam scanner equipped with a 4-*f* telescope (magnification: 1) and galvanometer-driven scanners (6220M, 7122-1*675, Cambridge Technology, Inc., MA). The back port of the microscope is used to introduce the laser beam into the microscope and finally to deliver the beam to the specimen. Inside the microscope, a telescope composed of scan (f_{SL} = 60 mm) and tube lenses (f_{TL} = 150 mm) magnifies the beam diameter by a factor of 2.5 to overfill the back-aperture of the objective to fully utilize the NA of the microscope objective. The lenses employed in the telescope are achromatic doublets purchased from Thorlabs, Inc. The beam is then deflected by a dichroic mirror (650dcspxr, Chroma Technology Corp.), and incident on the microscope objective. The pivot axes of all the scanner mirrors are relayed to the back focal plane of the objective to minimize the image curvature at the specimen plane. Experimentally, the back focal plane of the objective can be found by examining the power reflected from a mirror at the specimen plane as the beam scans laterally over the mirror surface. The objective is mounted on a piezo-electric transducer (Physik Instrumente, P-725.2CL) to scan the focal volume along the optical axis.

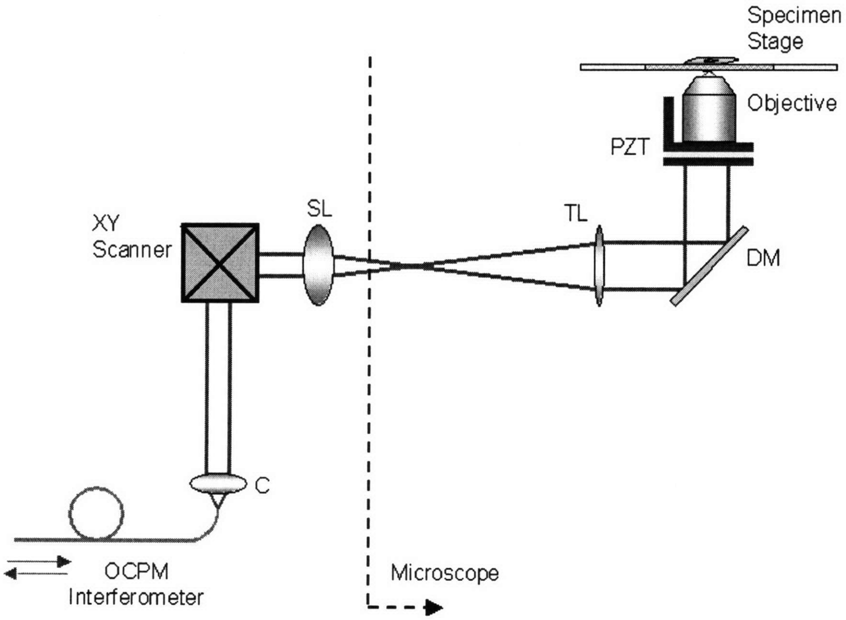

Figure 2.5: Schematic of SD-OCPM probe: (C) collimator; (SL) scan lens; (TL) tube lens; (PZT) piezo-electric transducer; (DM) dichroic mirror.

XY beam scanner

The galvanometer-driven scanners (6220M, 7122-1*675, Cambridge Technology, Inc., MA) are selected for small motion jitter to achieve high phase stability. The scanners have a relatively slow transient response with a settling time of ~2 msec, but it was found that it exhibits undershoot within ~5% of the steady-state position spanning another ~2 msec. The scanners have an angular jitter of $A \sim 1.7$ μrad in amplitude with a frequency of $f_0 \sim 1$ kHz for a constant input voltage. This jitter of the galvanometers causes the beam to oscillate laterally at an amplitude of $s(t) = f_{OBJ} \cdot \tan(\theta(t)/M)$ at the focal plane, where $\theta(t) = A \cdot \sin(2\pi f_0 t)$ and M is the magnification ratio in the optical setup. The beam displacement over the focal plane can then be approximated as $s(t) \sim f_{OBJ} A \cdot \sin(2\pi f_0 t / M)$. For an objective lens (Plan-NEOFLUAR 20×/0.5, Zeiss) using the magnification ratio of 2.5 in our SD-OCPM setup, $f_{OBJ} = 8.225$ mm and $|s(t)| <$ 0.015 μm, which is much smaller than beam scan displacement for imaging during the integration. Chapter 3 is devoted to the analysis of phase noise in SD-OCPM, where the reader can find that the phase noise due to the intrinsic motion jitter of the scanners is negligible compared to that caused by beam scanning.

1.1.5. SD-OCPM detection arm

Spectrometer setup

A custom-built high-speed spectrometer was used to acquire the cross-spectral density of reference and sample arms. The beam emitted by the detection arm fiber is collimated by a lens with a focal length of 100 mm, and incident on a volume holographic phase grating (1200 lines/mm, Wasatch Photonics, Inc.) at a Bragg angle. The spectrally dispersed beams are then focused by a three-element air-spaced lens onto CCD arrays of a 2048-element line scan camera (L-104k, Basler, Germany, 10 μm ×10 μm pixel size). The maximum read-out rate of the camera is 29.2 kHz and the acquired spectra could be transferred continuously to the host computer by CameraLink at a resolution of 10 bits/pixel. A frame grabber (PCI-1428, National Instruments) installed in the host computer manages the acquisition of spectra.

Spectrometer calibration

Since the complex-valued depth-resolved information of a specimen is obtained by taking an inverse Fourier transform of the spectrum of interference evenly spaced in the k – domain, it is of importance to perform the correct mapping of wavelength on the detector array and to interpolate the spectrum in the k – domain from the λ – domain. Using the experimental geometry of the transmission spectrometer depicted in Figure 2.6 and the paraxial approximation, one can approximate the distribution of wavelengths on the detector array as:

$$\lambda(x) = 2\Lambda \sin\left[\tan^{-1}\left(\frac{x - x_0}{f}\right) + \tan^{-1}\left(\frac{\lambda_0}{2\Lambda}\right)\right] \tag{2.7}$$

where x is the pixel location for λ on the detector array, Λ is the period of the transmission grating, f is the focal length of the lens, and x_0 is the pixel location for the center wavelength, λ_0.

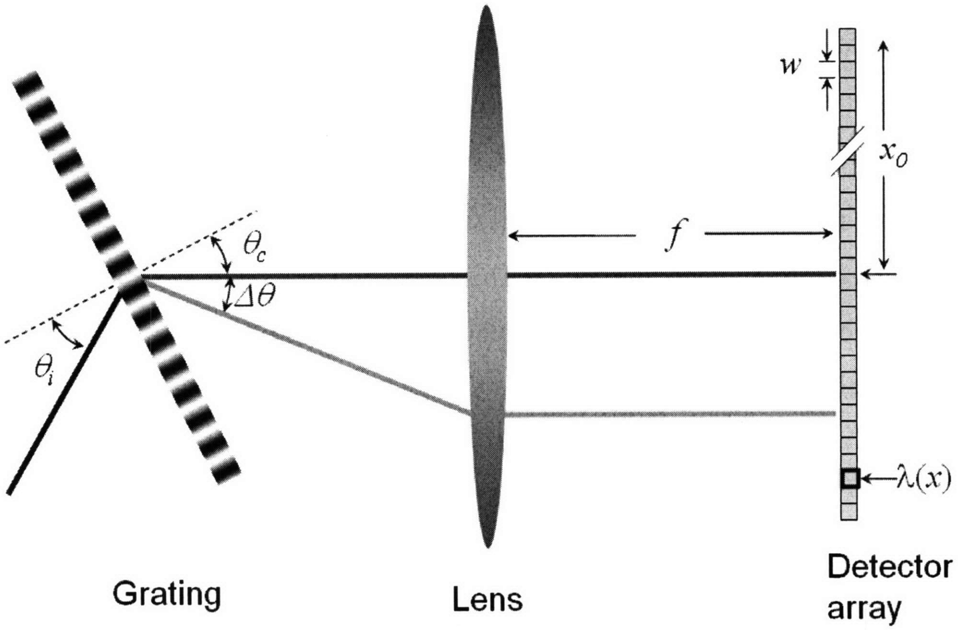

Figure 2.6: Schematics of the custom-built high-speed spectrometer. The collimated beam incident on a transmission grating is dispersed and focused on a linear CCD array.

In reality, however, any discrepancy of the experimental setup with the paraxial approximation made in Eqn. (2.7) results in the incorrect mapping of wavelengths on the detector array, and significantly influences the intensity and phase information of the sample. The errors due to the improper calibration of the spectrometer are extensively discussed by Dorrer [5].

For SD-OCT imaging, Mujat and de Boer [6] developed an auto-calibration method for the spectrometer, which does not require separate calibration procedure for *in-vivo* imaging. Basically, the auto-calibration method utilizes a calibration target that creates a perfect sinusoidal modulation in the $k-$domain. For instance, an air-spaced glass cavity with a gap of d placed in the one of the interferometer arms creates spectral modulation by combining the beam passing directly through the cavity with that internally reflected twice before transmission. The interference is of the form $\sim \cos(2kd)$, and its phase dispersion curve should be linear in $k-$space. If the spectrometer is not calibrated properly and the spectrum is incorrectly interpolated into $k-$space, the phase dispersion function becomes nonlinear, distorting the information in $z-$space. In the auto-calibration method, one makes an initial guess for the correct mapping of λ (typically using the relationship in Eqn. (2.7)), and tries to find and correct the phase offset from the linear fit. The nonlinear phase offset, $\Delta(k)$ from the linear fit is used to correct wavelength mapping function $\lambda(x)$ by $k(x) = 2\pi / \lambda(k) = k(x) + \Delta(k) / d$, which is re-calculated for new mapping for λ. This correction procedure is iterated until the offset is minimized. Once the correct mapping is found, and it is saved and used for the subsequent image processing.

2.4. SD-OCPM experimental setup: software

A multi-threaded program implemented in VC++ and running on Windows 2000 dual-processor computer manages data acquisition. Figure 2.7 shows a screen capture of the user interface of SD-OCPM acquisition program. Software initialization performs the D/A boards (NI PCI-6110, PCI-6773s) and frame grabber (NI PCI-1428) initialization and loads the waveforms to drive the line scan camera and the beam scanners. At the START of the program, it creates the main thread that handles the acquisition of the spectrum, which is subsequently saved into a node structure in a linked-list during the acquisition process. Separate threads were created to process the spectra in real-time and to save them to the hard disk as a binary format as desired. A thread priority was given to these threads so that the data could be saved at the highest speed of the line scan camera. Three separate display windows update spectrum, depth-resolved reflectance image, and *en-face* image at a plane in depth specified in the main front panel.

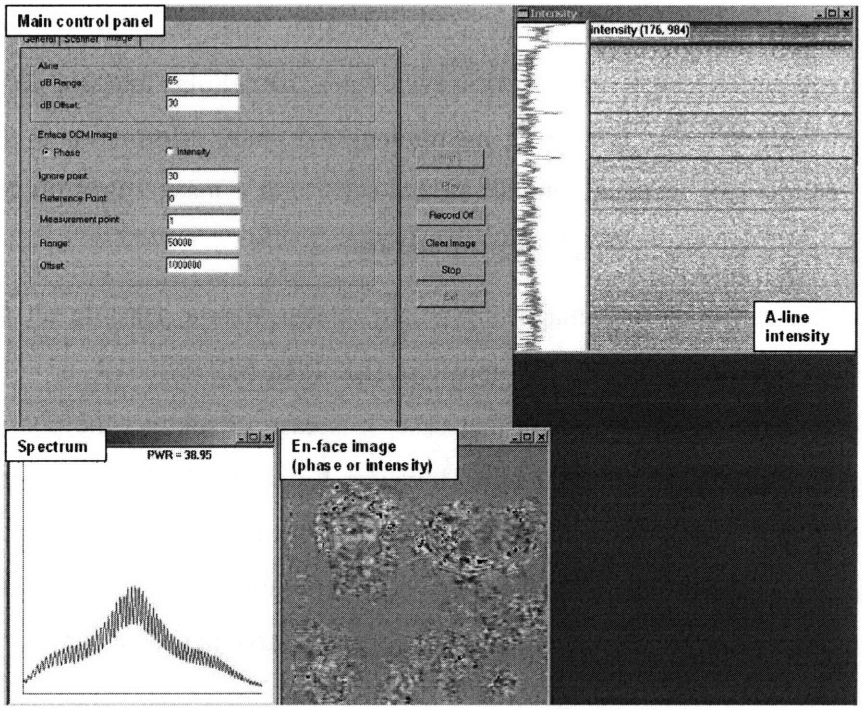

Aline
dB Range: 65
dB Offset: 30

Enface OCM Image
● Phase ○ Intensity
Ignore point: 30
Reference Point: 0
Measurement point: 1
Range: 50000
Offset: 1000000

Figure 2.7: A screen capture of SD-OCPM data acquisition program. The four displays are the main control panel, unprocessed spectrum, en-face phase or intensity image, and depth-resolved intensity information obtained by an inverse FFT of the spectra, respectively.

2.5. SD-OCPM image processing

SD-OCPM image processing is similar to that for typical SD-OCT processing, and was performed by code written in MATLAB. After the interpolation of the spectrum from λ to k space, an inverse Fourier transform of each A-line is performed to generate complex-valued depth information for a specimen. With prior knowledge of the depth location of interest, the phase for that location is obtained by taking the argument of the corresponding complex value. Typically, the phase distribution in the 2D plane of interest is wrapped, so Flynn's minimum discontinuity algorithm [7] is employed to unwrap the phase distribution.

For a reflective surface such as a glass or SiO_2 layer, the SNR is high, and the phase over the entire image is valid. However, for a 3D cellular imaging (especially as the beam is focused inside the cell or membrane), the phase information is not valid at low SNR regions (for instance, outside of the cell), and a mask based on the SNR or intensity map is used before the phase unwrapping.

The unwrapped phase image is typically planar with a possible tilt for a small FOV or the image obtained with the objective (LD Plan-NEOFLUAR, 63×/0.75, Zeiss) that I used for FOV optimization. In that case, it is easy to subtract the phase offset by estimating the plane based on the image. However, for a large FOV image with a size of more than 1 mm × 1 mm, the phase image is obscured by higher order aberrations such as hyperbolic phase offset. Several studies have been reported on the methods to correct this aberration, thereby improving the contrast in the quantitative phase images [8, 9].

2.6. Performance characterization

1.1.6. Field of View (FOV)

As in all point-scanning imaging techniques, SD-OCPM has a trade-off between the speed of acquisition and the FOV at the specimen plane. The larger image one acquires, the longer it takes. Using a simple paraxial approximation, the FOV can be estimated as $\Delta s = 2 f_{OBJ} \tan\left(\frac{\Delta\theta}{M} \times \frac{\pi}{180^\circ}\right)$, where f_{OBJ} is the effective focal length of the objective, $\Delta\theta$ is the deflection angle of the galvanometer scanners, and M is the magnification ratio, which is 2.5 in our case. This relationship rests on the assumption that the pivot point of the scanners is relayed to the back-focal plane of the objective.

In order to calibrate the FOV for SD-OCPM experimentally, we used an USAF resolution target, of which the feature size is already calibrated and available at http://www.edmundoptics.com/onlinecatalog/displayproduct.cfm?productid=1790.

After taking the image of the USAF target by SD-OCPM, the number of pixels on a known feature is counted and the FOV is estimated by

$$FOV = \frac{feature\ size}{\#of\ pixels\ \ on\ the\ feature} \times [total\ \#of\ pixels\ in\ image] \tag{2.8}$$

Figure 1 shows the FOV calibration curve for the objective (LD Plan-NEOFLUAR, 63×/0.75, Zeiss) obtained by varying the input voltage for the scanners.

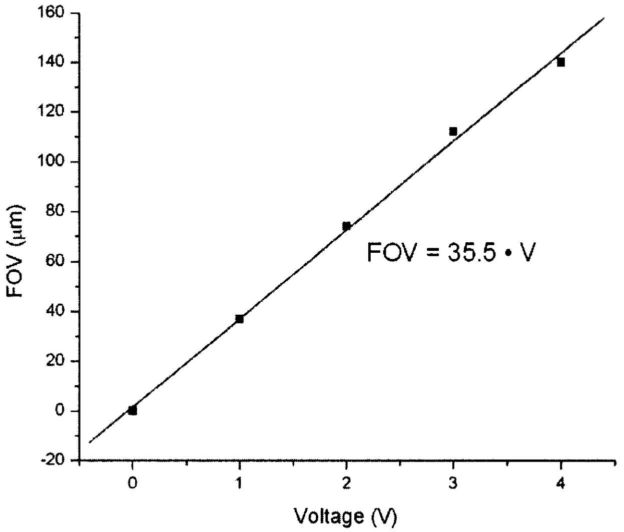

Figure 2.8: FOV calibration for SD-OCPM for the objective (LD Plan-NEOFLUAR, 63×/0.75)

1.1.7. Resolution

In imaging systems, resolution refers to the ability to distinguish, detect, and record physical features of an object. In a fiber-based implementation of SD-OCPM, the core in the single-mode fiber acts as a pinhole as in confocal microscopes, and the diffraction-limited lateral resolution can thus be predicted by [10]

$$I(v)=\left(\frac{2J_1(v)}{v}\right)^4 \tag{2.9}$$

where $v=k\cdot r\cdot NA$ and $J_1(v)$ is the Bessel function of the first kind. Using the center wavelength of 800 nm, the lateral resolution can be obtained as 1.83 μm and 4.13 μm for objectives with an NA of 0.75 and 0.5, respectively.

The lateral resolution in SD-OCPM was experimentally characterized by imaging an USAF resolution target (USAF 1951, Edmund Optics, NJ). The chromium step in the USAF target enables us to obtain a step response of the imaging setup, and the point spread function (PSF) can thus be calculated by taking the derivative of the step response. Figure 2.9 and 2.10 present the SD-OCPM intensity images of the USAF target, and the calculated lateral PSFs for the objectives with NAs of 0.75 and 0.5, respectively. The FWHM lateral resolutions were measured as 0.42 μm and 0.75 μm with the difference with the predicted values of ~8 % and ~27 %, respectively.

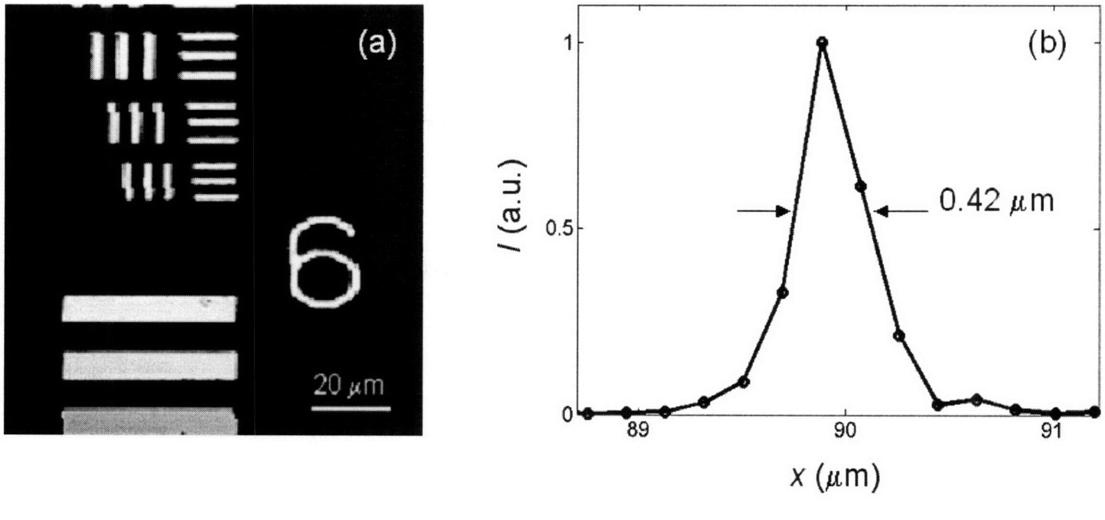

Figure 2.9: USAF target image (a) and lateral PSF (b) for SD-OCPM with NA=0.75

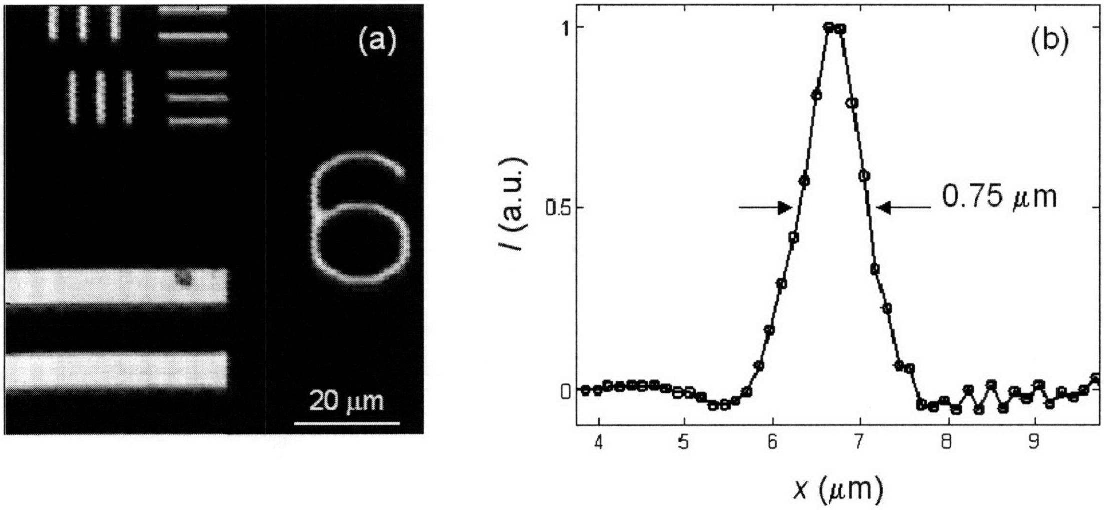

Figure 2.10: USAF target image (a) and lateral PSF (b) for SD-OCPM with NA=0.5

Unlike conventional confocal microscopes, the axial resolution of SD-OCPM is determined by the combination of confocal and coherence gatings [11]. Since the confocal and coherence gating are independent physical confinements for focal volume, their PSFs are multiplicative, leading to an improvement in the longitudinal resolution. The coherence gate for 130-nm bandwidth Ti:Sapphire source is roughly 2~3 μm, and the confocal gating is given by [10]

$$I(u) = \left(\frac{\sin(u/4)}{u/4} \right)^4 \tag{2.10}$$

where $u = k \cdot NA^2 \cdot z$. In order to appreciate the improvement in the axial resolution due to the combined confocal and coherence gating, a numerical simulation was performed for the objective with a NA of 0.5 (Figure 2.11). In the simulation, the center wavelength and the FWHM bandwidth were assumed to be 800 nm and 130 nm, respectively. Figure 2.11 (a) shows the axial PSFs for confocal and coherence gates. The multiplicative PSF is shown in Figure 2.12 (b). The confocal gate itself gives ~ 4.13 μm axial resolution, but the combination with the coherence gate improves the longitudinal resolution down to ~1.94 μm.

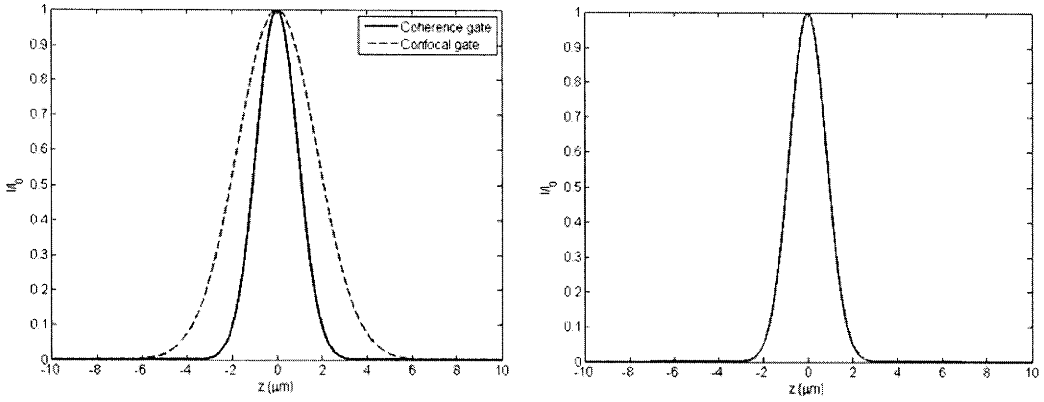

(a)

(b)

Figure 2.11: (a) Longitudinal PSFs for confocal and coherence gate; (b) Effective longitudinal PSF; The PSFs were calculated for an objective with NA=0.5 and the wavelength=800 nm.

The axial resolution of SD-OCPM was experimentally investigated by measuring the power reflected from the surface of a coverslip as the objective scans along the optical axis. Figure 2.12 presents the longitudinal PSFs measured for the objectives with NAs of 0.75 and 0.5, respectively.

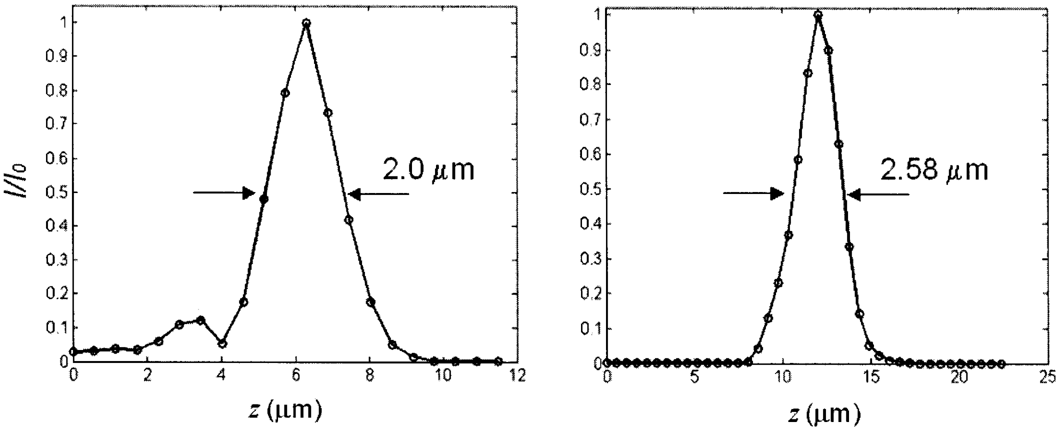

(a)

(b)

Figure 2.12: Measured longitudinal PSFs for SD-OCPM: (a) NA=0.75; (a) NA=0.5

A notable improvement can be observed in the case of the objective with a NA of 0.5, with the measured longitudinal resolution of 2.58 μm.

1.1.8. Phase stability

Phase sensitivity is a crucial performance factor in SD-OCPM, since it determines the ability of the system to detect minute phase changes spatially and temporally. The spatial phase changes are induced by spatial refractive index gradients and the variations of geometric size of the structures, and the temporal phase sensitivity is defined as the ability to detect minute changes in reflector (or scatterer) position in time. The phase sensitivity can be characterized by the variance (or the standard deviation) of the phase fluctuation, and has an explicit relationship with signal-to-noise ratio as $\sim 1/(2SNR)$, as described by Choma [12] and Park [13]. The detailed derivation of the relationship between phase stability and SNR will be described in Chapter 3.

In order to quantify SD-OCPM phase sensitivity, we measured the phase fluctuation of the interference between the reflections from the top and bottom surfaces of a coverslip with the scanners ON and OFF. Figure 2.13 shows the experimental phase fluctuation recorded as the scanners are OFF. The acquisition rate was 29 kHz, and the phase stability was measured as 25 pm in air. The measured SNR was 100.4 dB, under which condition the theoretical prediction gives ~0.4 pm. The discrepancy between the theoretical and experimental phase stability may be in part due to the external disturbances such as temperature gradient and vibration during the measurement.

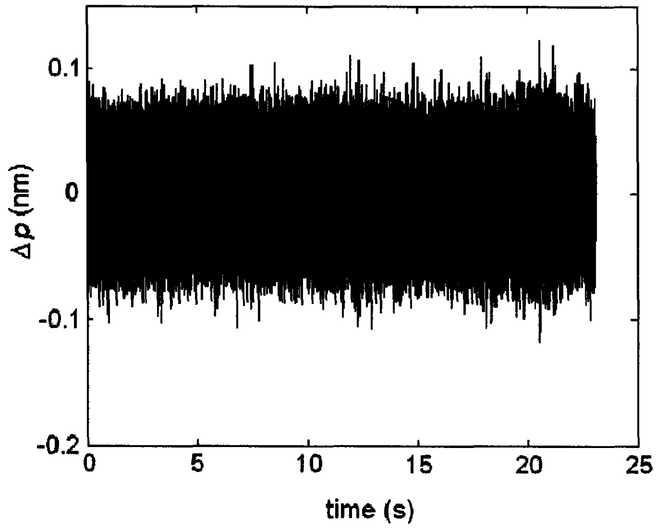

Figure 2.13: Measured phase stability with all the scanners powered OFF. The measurement was performed for ~21 seconds, and standard deviation was measured as ~25 pm at a measured SNR of 100.4 dB.

With all the scanners powered ON, we also investigated the spatial and temporal phase stability (Figure 2.14). In order to examine the spatial phase stability, we obtained two phase images of a coverslip, and took the difference between those maps to obtain repeatability of our phase measurement. Figure 2(a) shows the phase repeatability map, of which FOV is 42 μm x 42 μm with 100 x 100 pixels. The standard deviation across the FOV was measured as ~0.5 nm in air, which may be in part attributed to the motion jitter and repeatability of the scanners. For the temporal phase stability, the phase fluctuation was recorded as all X, Y, and Z scanners are set to a fixed value (0 V) (Figure 2(b)). The measured phase stability was ~53 pm in air at a SNR of 63.4 dB. The theoretical sensitivity is expected to be ~30 pm at the measured SNR.

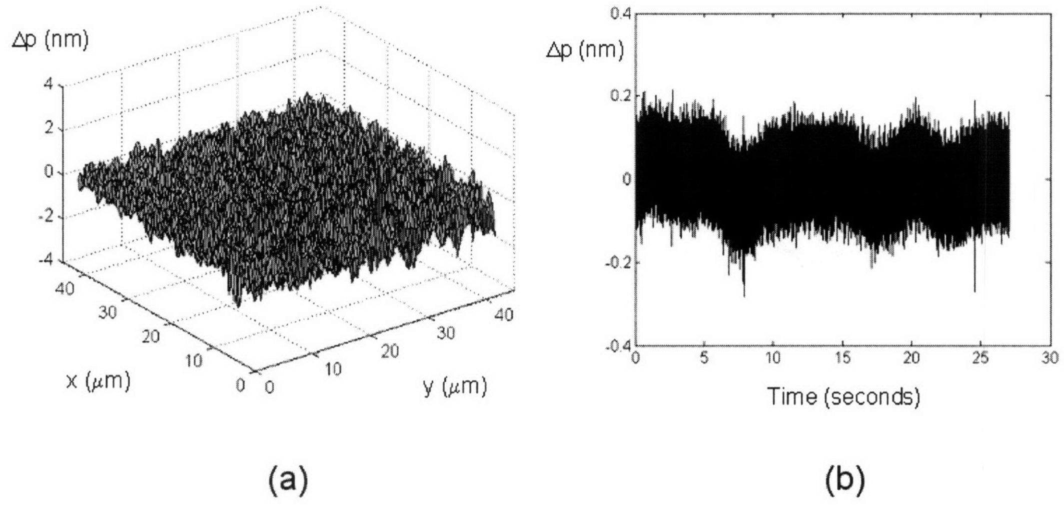

Figure 2.14: Spatial and temporal phase stability with all the scanners powered ON.

2.7. Experimental results

1.1.9. Calibrated phase specimen

To assess the imaging performance of SD-OCPM, a phase specimen with a known feature was first examined. The specimen was an "MGH" etched coverslip prepared by a standard photolithographic technique. After the photoresist was exposed to UV light and cleaned from the coverslip, the "MGH" letters were etched into the coverslip in a Buffered Oxide Etch solution for ~ 15 seconds. The height and width of each letter in the original mask were 125 μm and 25 μm, respectively, but the possible contamination of the specimen, the imperfect process in exposure, and more importantly, isotropic etching characteristic in the BOE process broadened the feature size. For imaging, the phase of the interference between the reflections from the top and bottom surfaces of the etched coverslip was measured as the beam scans laterally. The measured phase was converted to the optical path-length difference in air. Figure 2.15 shows the images of the specimen recorded by Nomarski microscope (10×, NA=0.3) and SD-OCPM (NA=0.2). The grayscale to the right of the SD-OCPM image denotes the etch depth with reference to the flat (not etched) surface in nanometers. One can note the improved contrast in the SD-OCPM image. Figure 2.15(c) shows the etch depth profile of the coverslip in 3D.

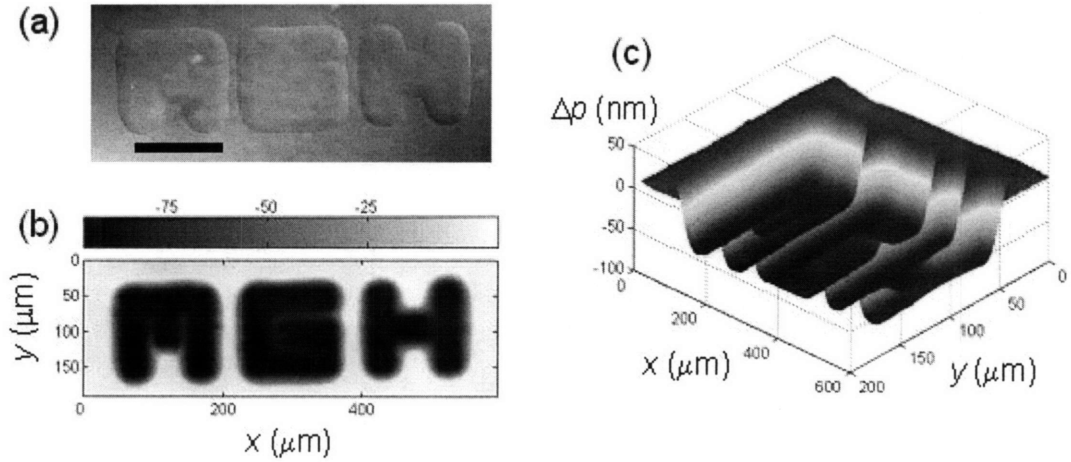

Figure 2.15: Images of an "MGH" etched coverslip. (a) Image recorded by Nomarski microscope (10×, NA: 0.3). The solid bar corresponds to 125 μm. (b) Image taken by SD-OCPM. Gray scale represents the etch depth in nanometers. (c) Three-dimensional etch depth representation for the "MGH" patterned coverslip.

To evaluate the accuracy and to compare SD-OCPM measurement with other methods, a surface profiler (Dektak 3030) was used to measure the same sample. The profiler scanned the "MGH" etched surface in the direction shown in Figure 2.16(a), and the result is shown in Figure 2.16(b), along with the result measured by SD-OCPM. The SD-OCPM measurement was converted into physical dimension using the refractive index of the coverslip of 1.51. The difference between the two measurements may be due to the different lateral resolution and the different sample condition in two separate measurement. However, the measurements were in a good agreement, and the difference was less than 5 nm.

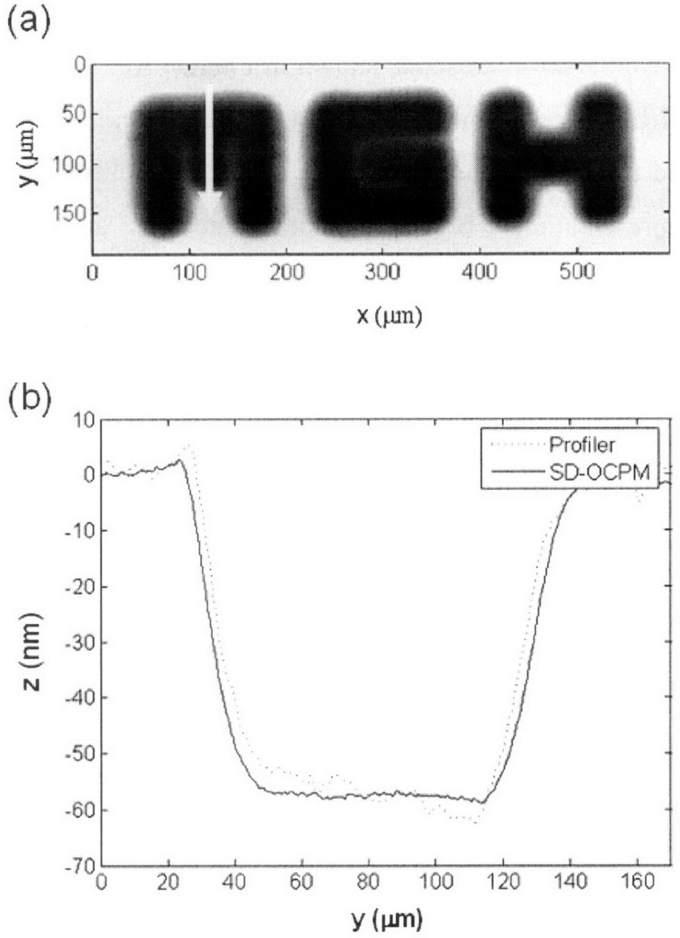

Figure 2.16: Comparison of phase measurement between SD-OCPM and a surface profiler (Dektak 3030). The surface profiler scanned the "MGH" etched coverslip along the direction shown in (a), and the result is presented in (b), along with the phase measurement by SD-OCPM in the same region. The difference between two measurements was less than 5 nm.

1.1.10. Human epithelial cheek cells

SD-OCPM was then applied to image human epithelial cheek cells. The cells were placed between a glass slide and a coverslip, and the microscope measured the phase of the interference between the top surfaces of the coverslip and the glass slide to examine *en-face* phase distribution. Figure 2.17 shows the cellular images obtained by

Nomarski microscope (NA=0.3) and SD-OCPM (NA=0.2), respectively. Note that the cell imaged by Nomarski microscope shown in Fig. 2.17(a) is not of the same epithelial cell in Fig. 2.17(b). In addition to the *en-face* phase image, the surface map of the phase image is plotted to show the optically thick nuclei and subcellular structures in a three dimensional representation. The cell membrane, nucleus, and some other sub-cellular structures are visible. Two cheek cells seem to be superimposed based on two nuclei in the image. The image contains 350×300 pixels, and the total acquisition time was 3.6 seconds.

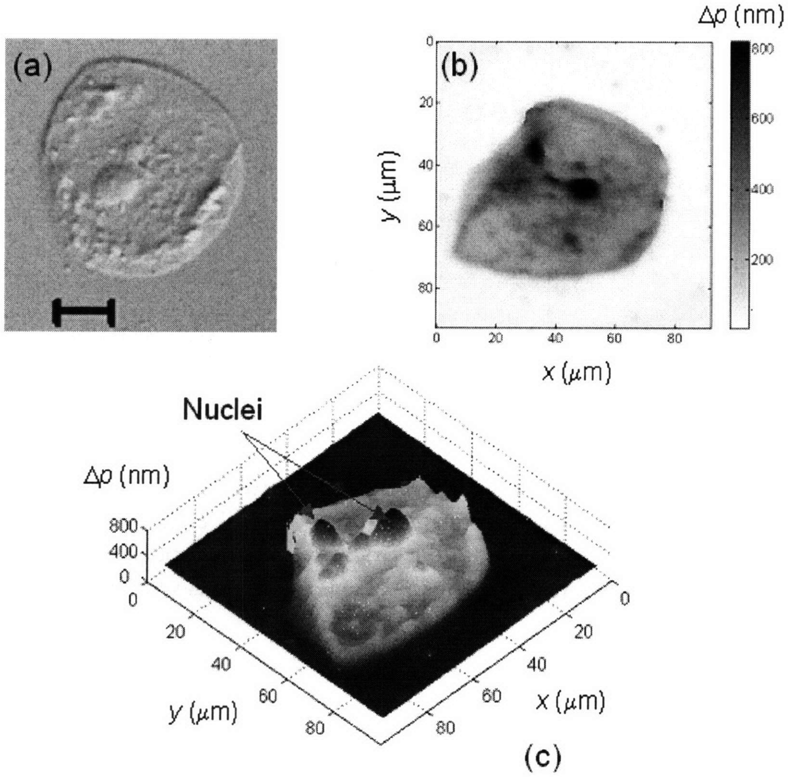

Figure 2.17: Images of human epithelial cheek cells. The image (a) is recorded by Nomarski microscope (10×, NA: 0.3), and the bar represents 20 μm. The SD-OCPM image is also shown along with the gray scale denoting OPL in nanometers in (b). The image (c) is a surface plot of (b), showing optically thick structures such as nucleus and subcellular structures in the cell. The nuclei and subcellular structures are visible, and two cells seem to be overlapping, based on the two nuclei in the image.

1.1.11. Fixed and stained muntjac skin fibroblast

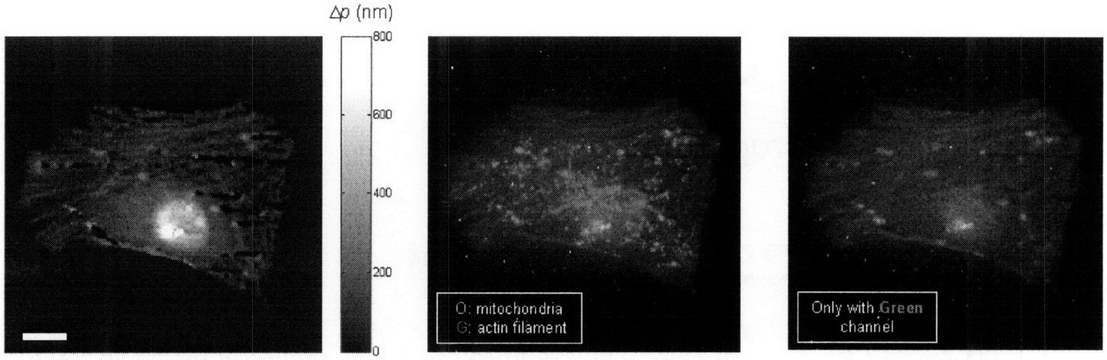

(a) (b) (c)

Figure 2.18: Images of a fixed and stained muntjac skin fibroblast. The image (a) is recorded by SD-OCPM (NA: 0.5), is shown along with the grayscale bar denoting OPL in nanometers. The same specimen was imaged by a fluorescence microscope. The image (b) is the fluorescence image obtained with RGB channels open, and the image (c) is only with green channel. The comparison between SD-OCPM and fluorescence images demonstrates a great correlation in terms of the visualization of nucleus and actin filament distribution inside the cell. The scalebar represents 10 μm.

We also performed SD-OCPM imaging on fixed and fluorescently labeled muntjac skin fibroblasts. The sample was purchased from Invitrogen Corp. (FluoCells #6). For SD-OCPM imaging, the focal volume was positioned at ~2 μm above the top surface of the coverslip, and the phase of the interference between the reflections from the focal volume and the bottom surface of the coverslip was recorded. Figure 2.18(a) shows the quantitative phase image obtained by SD-OCPM. The cell boundary, nucleus, and other cellular structures are clearly visible. The grayscale bar to the right of the phase image represents the phase in nm. In order to interpret and identify the structures observed in the SD-OCPM phase image, the same specimen was examined with a fluorescence microscope. Figure 2.18(b) and 2.18(c) show the fluorescence images with all fluorescence (red, green, and blue) channels open and with green channel only, respectively. One can see that the distribution of actin filaments inside the cell showed a great correlation between the SD-OCPM and the fluorescence images. This feature becomes more obvious by comparing SD-OCPM phase image with the green channel fluorescence image (Figure 2.18(c)).

1.1.12. Living macrophages

SD-OCPM live cell imaging was conducted with macrophages inside an imaging chamber (48-Q-0.1, Starna Cells, Inc.). For imaging, the phase of the interference between the reflections from the interfaces inside the chamber was measured. The actual image acquisition time was ~6.5 seconds with an image size of 256×256 pixels, but the SD-OCPM data acquisition program acquired an image at every minute.

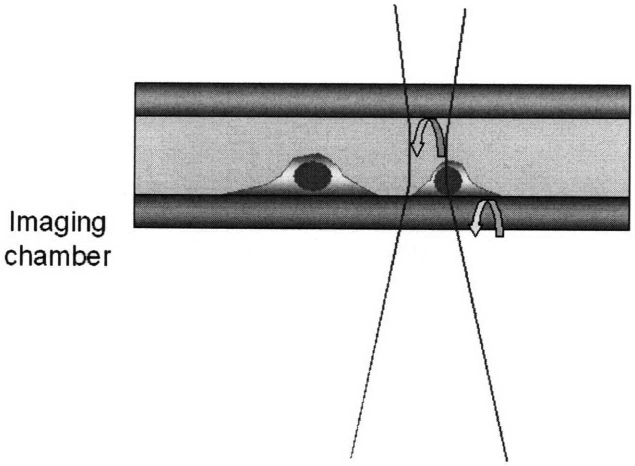

Figure 2.19: The live macrophages inside an image chamber were imaged by measuring the phase of the interference between the reflections from the interfaces inside the chamber.

Figure 2.20 shows representative SD-OCPM images at every 15 minutes. The images on the first column are the 3D representation of quantitative phase image, and those on the second column are the corresponding phase difference images. The phase difference image was obtained by taking two-dimensional gradient of the phase image and showing the horizontal components of the vectors in each pixel, thereby giving a projection view at 0 degree. In some sense, the phase difference scheme is similar to the conventional DIC method, except that it is quantitative, computationally obtained, and can provide phase difference in any direction by manipulating the vectors. It clearly shows that the cells exhibited dynamic movements such as protrusion and retraction during the imaging time, and the arrow in the phase difference image points to pseudopods, characteristic structures of the macrophages. The color bar to the right of the first column images denotes the phase distribution in radians, and the scalebar in the phase difference image represents 50 μm.

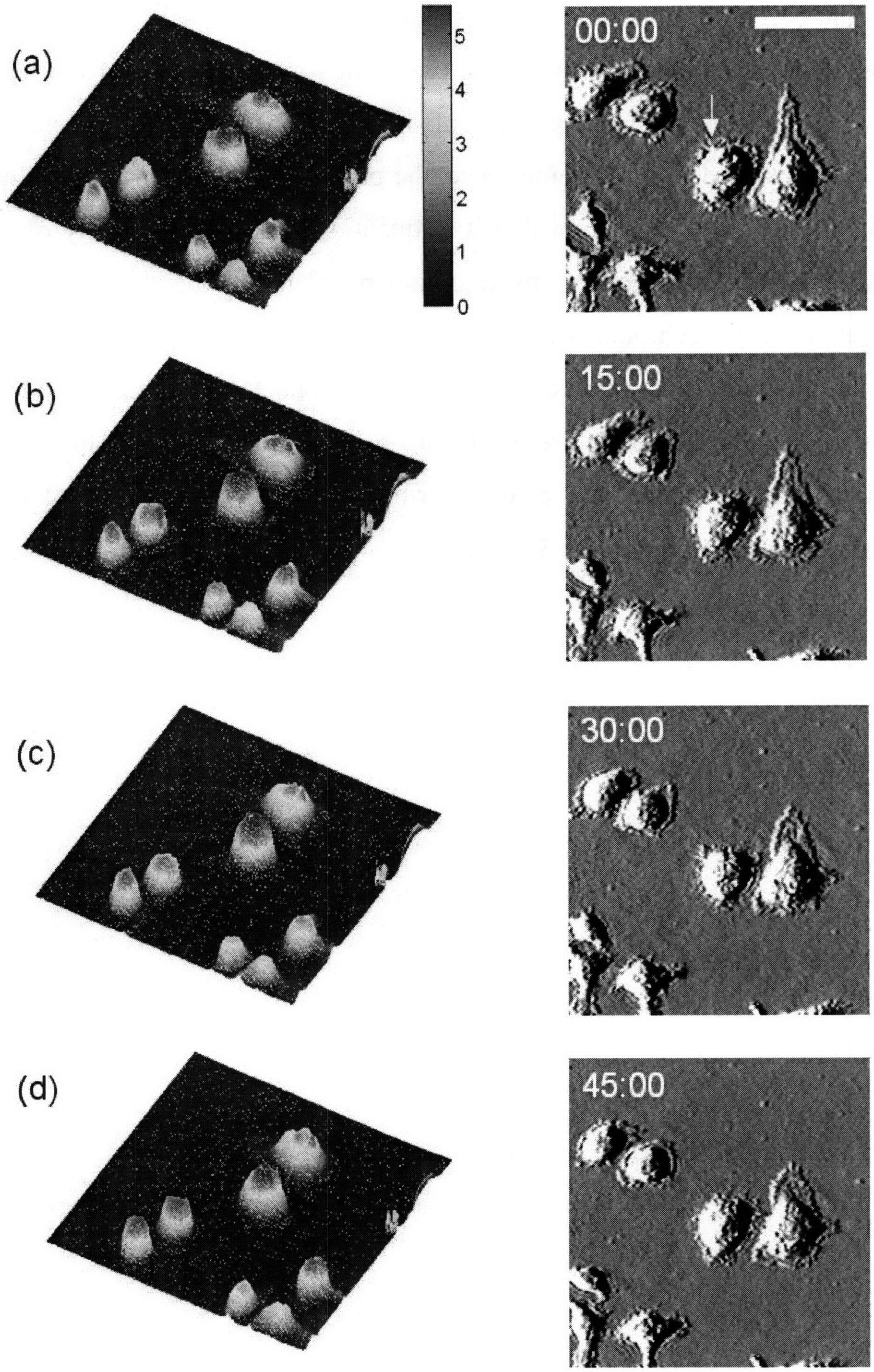

Figure 2.20: Time-lapsed SD-OCPM phase images of living macrophages inside an imaging chamber. Shown are the images taken at 0(a), 15(b), 30(c), and 45(d) minutes, respectively. The arrow in the DPI image (a) indicates pseudopods of the macrophages. The color bar to the right of the first column images denotes the phase in radians, and the scalebar in the differential phase image represents 50 μm.

2.8. Summary

Based on the features of a common-path SD-OCT interferometer, SD-OCPM was developed for quantitative phase imaging of transparent specimens. SD-OCPM can record spatial and temporal phase alteration with sub-nanometer sensitivity. The performance measures of SD-OCPM such as spatial resolutions and FOV were characterized, and its phase stability extended into the sub-nanometer regime, following the theoretical prediction. As an initial demonstration for SD-OCPM phase imaging, various transparent specimens were examined. As a calibrated phase target, an "MGH" patterned coverslip was measured, and its accuracy was confirmed within nanometer-level accuracy by a measurement with a surface profiler. SD-OCPM was also applied to image biological specimens: human epithelial cheek cells and fixed and stained muntjac skin fibroblast cells. The images provided high contrast details on the subcellular structures, and for the stained cellular imaging, we could observe a good correlation for the actin filament distribution between SD-OCPM phase and fluorescence images. The time-lapsed SD-OCPM imaging on live macrophages was also conducted, and observed the dynamic movements of cellular membranes and the peusopods.

2.9. Reference

1. Fercher, A.F., et al., *Optical coherence tomography - principles and applications.* Reports on Progress in Physics, 2003. **66**: p. 239-303.

2. Nassif, N., et al., *In vivo human retical imaging by ultrahigh-speed spectral domain optical coherence tomography.* Optics Letters, 2003. **29**(5): p. 480-482.

3. Fercher, A.F., et al., *Measurement of intraocular distances by backscattering spectral interferometry.* Optics Communications, 1995. **117**: p. 43-48.

4. Bouma, B.E. and G.T. Tearney, *Handbook of Optical Coherence Tomography.* 2002, New York: Marcel Dekker.

5. Dorrer, C., et al., *Spectral resolution and sampling issues in Fourier-transform spectral interferometry.* Journal of Optical Society of America B, 2000. **17**(10): p. 1795-1802.

6. Mujat, M., et al., *Auto-calibration of spectral-domain optical coherence tomography spectrometers for in-vivo quantitative retinal nerve fiber layer birefrigence determination.* Journal of Biomedical Optics, 2007.

7. Ghiglia, D.C. and M.D. Pritt, *Two-dimensional phase unwrapping: theory, algorithms, and software.* 1998, New York: John Wiley & Sons, Inc.

8. Ferraro, P., et al., *Compensation of the inherent wave front curvature in digital holographic coherent microscopy for quantitative phase-contrast imaging.* Applied Optics, 2003. **42**(11): p. 1938-1946.

9. Miccio, L., et al., *Direct full compensation of the aberrations in quantitative phase microscopy of thin objects by a single digital hologram.* Applied Physics Letters, 2007. **90**: p. 041104.

10. Wilson, T., *Confocal Microscopy.* 1990, London: Academic Press.

11. Izatt, J.A., et al., *Optical coherence microscopy in scattering media.* Optics Letters, 1994. **19**: p. 590-592.

12. Choma, M.A., et al., *Spectral-domain phase microscopy.* Optics Letters, 2005. **30**: p. 1162-1164.

13. Park, B.H., et al., *Real-time fiber-based multi-functional spectral-domain optical coherence tomography at 1.3 μm.* Optics Express, 2005. **13**(11): p. 3931-3944.

Chapter 3:

SD-OCPM Noise Analysis

3.1. Introduction

SD-OCPM is a highly sensitive imaging technique capable of measuring nanometer-level phase fluctuations of transparent specimens. The sensitivity of SD-OCPM is influenced both by intrinsic noise in the SD-OCPM interferometer and by other external factors such as disturbances from the environment and the equipment employed in SD-OCPM implementation. As with other phase measurement methods, the noise contributions from an environment can be minimized by enclosing the instrument inside an environment-controlled chamber. However, this is usually expensive and impractical. This Chapter is devoted to the analysis of the noise performance of SD-OCPM, with a focus on the contributions from the SD-OCPM interferometer and other equipment, more specifically the scanners.

We begin the discussion with an analysis of the noise components in the SD-OCPM interferometer, and demonstrate that SD-OCPM operation is shot-noise limited. The analysis based on the description presented in Ref. [1]. Based on this observation, the factors that contribute to the signal-to-noise ratio (SNR) are examined. The importance of SNR to phase measurement is elucidated by showing its relationship with the phase probability density function, which is further emphasized by experimental confirmation.

The scanners employed in SD-OCPM phase detection are another source of noise. We theoretically model the contributions from the scanners in both the lateral and axial directions, and demonstrate the validity of the model with comparison to the experimental results.

3.2. SD-OCPM interferometer noise performance

Sorin and Baney considered the contributions of thermal noise (detector noise), shot noise, and relative intensity noise (RIN) to the noise density in the detection of optical low-coherence interferometers [2]. Using the notations in Ref. [2], the noise in each frequency is expressed as:

$$N = \frac{4k_B T}{R} + \frac{2\eta e^2 (P_r + P_s)}{E_v} + 2\left(\frac{\eta e (P_r + P_s)}{E_v}\right)^2 \tau_{coh} . \tag{3.1}$$

where each term on the right hand side represents thermal noise, shot noise, and RIN noise, respectively. Here, a degree of polarization of 1 was assumed, and k_B is the Boltzmann's constant, T is the temperature, R is the value of the transimpedance amplifier feedback resistor, E_v is the photon energy, and τ_{coh} is the coherence time of the source. The coherence time is related to the FWHM spectral width, $\delta\lambda$ equal to $\tau_{coh} = (2\ln 2/\pi)\lambda_0^2 / c\delta\lambda$ [3].

3.2.1. Shot noise vs. RIN

From Eqn. (3.1), it can be seen that the shot-noise contribution is dominant over the RIN noise if

$$\frac{E_v}{\eta(P_r + P_s)\tau_{coh}} >> 1. \qquad (3.2)$$

The examination of sensitivity decay as a function of scan depth reveals that the spectral resolution is $\delta\lambda \sim 0.139$ nm [1], which gives the source coherence time per pixel element, $\tau_{coh} \sim 6.7$ psec. Based on these values, evaluation of Eqn. (3.2) leads to

$$(P_r + P_s) << \frac{36.7}{\eta} \qquad [\text{nW}] \qquad (3.3)$$

for a center wavelength of 800 nm. Practically, the efficiency of the spectrometer, η, is the combination of the transmission efficiency of all the optical components employed in the spectrometer and the quantum efficiency of the CCD array. Even with the highest efficiency from the vendors' specifications, it cannot be more than 50 % (In Ref. [1], we reported the efficiency of our spectrometer as ~28 %). That is, even at the highest efficiency achievable, the shot noise becomes dominant over RIN if the power at the pixel element is smaller than ~73.4 nW. For the SD-OCPM spectrometer, the CCD line scan camera with 2048 pixel elements is saturated at ~10 μW measured at the detection fiber tip, which means that the detector element is saturated at ~4.8 nW. This level is already smaller than 73.4 nW, so in the current SD-OCPM detection, shot-noise is always dominant over RIN noise.

3.2.2. Shot noise vs. Dark and readout noise

Shot noise, by definition, is the noise caused by the statistical fluctuations in the number of discrete carriers in a measurement, and its variance at i detector element is equal to the mean:

$$\sigma_{i,SN}^2 = \left\langle \left(N_i - \overline{N_i}\right)^2 \right\rangle = \overline{N_i} \qquad [\text{\# of electrons}] \qquad (3.4)$$

where the $\langle \ \rangle$ brackets represent the ensemble average, and N_i denotes the number of electrons at i detector element. The CCD line scan camera employed in SD-OCPM setup (L-104k, Baslers, Germany) measures the number of detected electrons as a 10-bit pixel value, i.e., 0~1023. An analog-to-digital (A/D) conversion resolution, Δe, is thus introduced, defined as the number of electrons required to increase a level of one in pixel value:

$$I_i = \frac{N_i}{\Delta e} \qquad \text{[pixel value]} \qquad (3.5)$$

where I_i indicates the pixel value at i element. The noise variance in each pixel, σ_i^2, can then be given by:

$$\begin{aligned} \sigma_i^2 &= \left(\frac{\sigma_{i,SN}}{\Delta e}\right)^2 + \sigma_{i,r+d}^2 \\ &= \frac{\overline{N_i}}{\Delta e^2} + \sigma_{i,r+d}^2 \qquad \text{[pixel value]} \qquad (3.6) \\ &= \frac{\overline{I_i}}{\Delta e} + \sigma_{i,r+d}^2 \end{aligned}$$

in pixel value (0~1023). The first and second terms on the right hand side represent the shot-noise and the read-out and dark noise contributions to the total noise, respectively. RIN noise contributions are not considered because it is never dominant over shot noise as discussed previously. Figure 3.1 shows the measured shot-noise and read-out + dark noise at 34.1 μsec/A-line with a coverslip at the specimen plane. The noise was determined by calculation of the unbiased variance at each camera pixel for 1024 spectra, and the dark noise measurement was conducted with no incident light. From the measured noise variance, the A/D conversion resolution was obtained as 174e (electrons), and the full-depth was estimated as 178176e, respectively. The average read-out and dark noise was found as 1692e, which demonstrates that the shot noise is dominant at the level of light more than 1.5 % of the full well depth of the pixel.

In a typical SD-OCPM operation, the power level incident on the detector element is more than 5 % of full pixel depth. Therefore, based on the previous discussions, SD-OCPM operates in shot-noise limited regime.

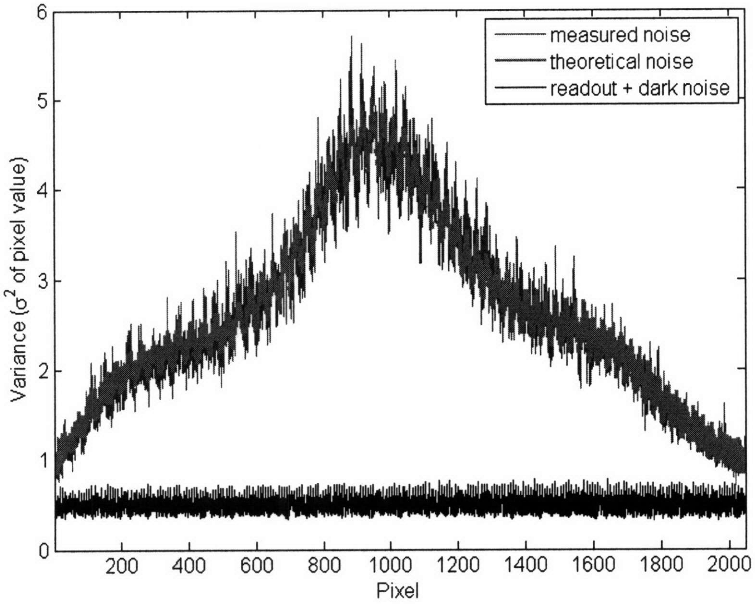

Figure 3.1. Noise components in the spectrometer measured with a coverslip at the specimen plane. The shot noise level was used to determine the A/D resolution of the detector. The theoretical shot noise curve was fit using Eqn. (3.5) to the measured average spectrum, giving an A/D conversion Δe of 174 electrons and a corresponding well depth of 178176 electrons.

3.3. SD-OCPM phase sensitivity vs. SNR

In the previous section, we demonstrated that SD-OCPM operation is shot-noise limited. Based on this observation, this section describes the importance of SNR to obtain high phase sensitivity.

3.3.1. SNR in SD-OCPM interferometer

Before we discuss the relationship between SNR and phase sensitivity, it would be of interest to consider the factors that contribute to SNR in the SD-OCPM measurement.

In the shot-noise limited SD-OCT setup, the interference signal and noise are spectrally dispersed across the pixels on the CCD array, with each pixel receiving only a fraction of the detection beam. Therefore, the shot-noise contribution is reduced by a factor proportional to the number of detectors on the CCD array (due to the incoherent characteristic of noise). Indeed, the noise is given by [4]

$$N = \frac{2\eta e^2\left(P_r + \sum_n P_{s,n}\right)}{E_v}\frac{BW}{M}, \tag{3.7}$$

where P_r and $P_{s,n}$ represent the back-reflected power from the reference and the n^{th} interface in the sample, respectively, BW denotes the frequency bandwidth, and M is the number of pixels on the detector array [4]. In the case of the signal, it is coherently summed as performing an inverse Fourier transform of the spectrum to give

$$S = \frac{2\eta^2 e^2 \left(P_r P_{s,n}\right)}{E_v^2}. \tag{3.8}$$

SNR can then be calculated by taking the ratio of Eqn. (3.7) to Eqn. (3.6):

$$\frac{S}{N} = \frac{\eta M}{E_v BW}\frac{P_r P_{s,n}}{P_r + \sum_n P_{s,n}}. \tag{3.9}$$

By use of Nyquist's theorem, the bandwidth per detector element (BW/M) is replaced by $1/2\tau_i$, where τ_i is the integration time of the array. Since fully parallel SD-OCPM measures only the real part of the complex cross-spectral density, the signal is reduced by a factor of 2, resulting in

$$\frac{S}{N}=\frac{\eta\tau_i}{E_v}\frac{P_r P_{s,n}}{P_r+\sum_n P_{s,n}}. \tag{3.10}$$

Eqn. (3.10) states that *SNR* is mainly determined by the integration time and reference power for a given spectrometer efficiency and sample structure. The integration time is set by the CCD acquisition speed, and one can improve SNR by increasing the integration time if it meets the requirement of speed. The noise is affected by the reference arm power as well as all the reflections from the sample surfaces. Therefore, SNR will be reduced for samples with multiple layers such as biological tissues, in which all the reflections from the sample contribute to the noise level. However, one can minimize this SNR reduction with high reference arm power, in which case, SNR is only determined by the sample reflection of interest.

3.3.2. Phasor diagram analysis

The importance of SNR in the phase measurement can be seen by noting its role in the phase determination. The relationship between the phase stability and SNR can be easily derived based on a phasor diagram.

Consider complex information, $F(z)=ae^{j\theta}$ obtained by an inverse Fourier transform of the SD-OCPM interference spectrum. $F(z)$ is essentially the superposition of the signal and noise, and can thus be expressed by $F(z)=se^{j\phi}+ne^{j(\theta-\phi)}$, where s and n denote the magnitude of the signal and noise, respectively (Figure 3.2). One can decompose and map the real and imaginary components into the phasor plane, and using a simple trigonometry, can find

$$\Delta\varphi\equiv\theta-\phi=\tan^{-1}\left(\frac{n\sin(\Delta\theta)}{s+n\cos(\Delta\theta)}\right), \tag{3.11}$$

which becomes $\Delta\varphi = (n/s)\sin(\Delta\theta)$ for a high SNR (s/n>>1). The variance of the phase error is then calculated by the time-average of the squared as

$$\left\langle \Delta\varphi^2 \right\rangle = \left\langle \frac{n^2}{s^2} \right\rangle \left\langle \sin^2 \Delta\theta \right\rangle = \frac{1}{2}\frac{1}{SNR}. \tag{3.12}$$

where SNR is defined as $\left\langle s^2/n^2 \right\rangle$. It can be noted that the phase sensitivity of SD-OCPM is inversely proportional to SNR; the higher SNR, the higher phase precision one can achieve [5, 6].

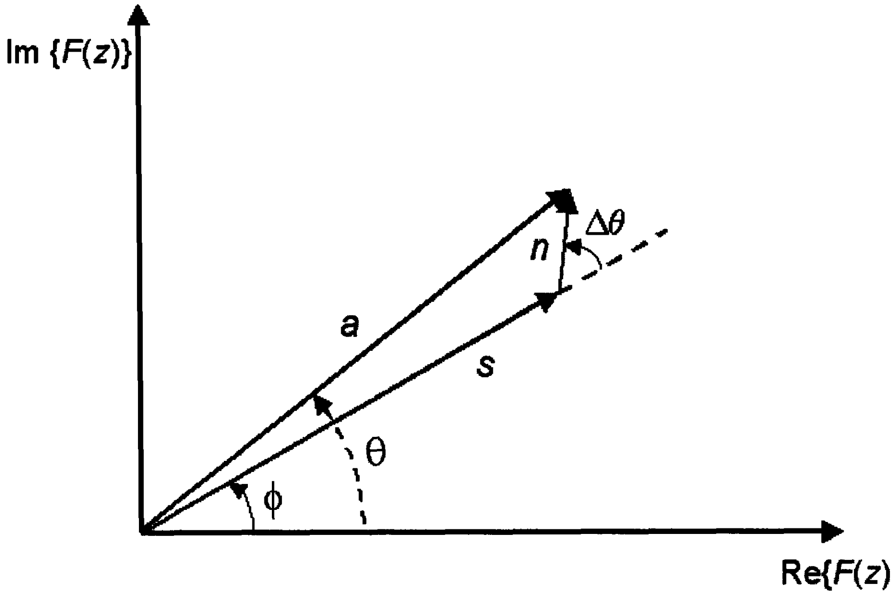

Figure 3.2. Phasor diagram for SD-OCPM signal and noise

3.3.3. Probability density function for phase determination

In the previous Section, an explicit functional relationship of phase stability and SNR was obtained using the simple trigonometry in the phasor diagram. For a high SNR, the variance of the phase stability is simply given by $1/(2SNR)$.

In the case of phase measurement with low SNRs, however, the prediction for the phase stability described earlier is not valid any more. Here, a general expression for the probability density function (PDF) of the phase is derived that can be applied to a low SNR regime. The analysis is based on the first-order statistics of Gaussian random variables [7].

The complex information obtained by SD-OCPM data processing is the superposition of the signal and noise, and can be decomposed into the real and imaginary components:

$$r = s_R + n_R \tag{3.13}$$

$$i = s_I + n_I \,. \tag{3.14}$$

Assuming that the noise is circularly Gaussian, the joint probability density function of the real and imaginary parts of the total phasor becomes

$$p_{RI}(r,i) = \frac{1}{2\pi\sigma^2}\exp\left[-\frac{(r-s_R)^2+(i-s_I)^2}{2\sigma^2}\right]. \tag{3.15}$$

In order to obtain the first-order statistics of the phase of the resultant, one must apply the transformation of the random variables. The desired joint density function in amplitude and phase domain is expressed in terms of the joint density function for r and i as

$$p_{A\Theta} = p_{RI}(a\cos\theta, a\sin\theta)\|J\| \tag{3.16}$$

where $\|J\|$ is the Jacobian of the transformation:

$$\|J\| = \begin{Vmatrix} \dfrac{\partial r}{\partial a} & \dfrac{\partial r}{\partial \theta} \\ \dfrac{\partial i}{\partial a} & \dfrac{\partial i}{\partial \theta} \end{Vmatrix} = a \tag{3.17}$$

and $\|\cdots\|$ denotes the modulus of the determinant. Substituting Eqn. (3.15) in (3.16), one obtains

$$p_{A\Theta}(a,\theta) = \begin{cases} \dfrac{a}{2\pi\sigma^2}\exp\left[-\dfrac{(a\cos\theta - s_R)^2 + (a\sin\theta - s_I)^2}{2\sigma^2}\right] & a > 0, -\pi < \theta \leq \pi \\ 0 & \textit{otherwise.} \end{cases} \tag{3.18}$$

The PDF for the phase can then be evaluated by integrating Eqn. (3.18) over the amplitude space,

$$\begin{aligned} p_\Theta(\theta) &= \int_0^\infty p_{A\Theta}(a,\theta)da \\ &= \frac{1}{2\pi\sigma^2}e^{-\frac{s^2}{2\sigma^2}\left[1-\cos^2(\theta-\phi)\right]}\int_0^\infty a\exp\left[-\frac{\left[a - s\cos(\theta-\phi)\right]^2}{2\sigma^2}\right]da \end{aligned} \tag{3.19}$$

where

$$s^2 = s_R^2 + s_I^2 \tag{3.20}$$

$$\phi = \tan^{-1}\left(\frac{s_I}{s_R}\right) \tag{3.21}$$

For further evaluation of the integral, let us define the intermediate variables as:

$$b = \frac{s}{\sigma}\cos(\theta - \phi) \tag{3.22}$$

$$y = \frac{a}{\sigma} - b \tag{3.23}$$

then the integral becomes

$$p_{\Theta}(\theta) = \frac{1}{2\pi} e^{-\frac{s^2}{2\sigma^2}\sin^2(\theta-\phi)} \int_{-\infty}^{b} (y+b) e^{-y^2/2} dy . \tag{3.24}$$

Defining $SNR = s^2/(\sigma_R^2 + \sigma_I^2) = s^2/2\sigma^2$, Eqn. (3.24) becomes

$$p_{\Theta}(\theta) = \frac{e^{-SNR}}{2\pi} + \sqrt{\frac{SNR}{\pi}} \cos(\theta-\phi) e^{-SNR\sin^2(\theta-\phi)} \Phi\left[\sqrt{2SNR}\cos(\theta-\phi)\right] \tag{3.25}$$

where

$$\Phi(b) = \frac{1}{\sqrt{2\pi}} \int_{-\infty}^{b} e^{-y^2/2} dy . \tag{3.26}$$

Eqn. (3.25) represents a general expression for the phase PDF that describes the phase noise characteristics as a function of SNR. For $SNR >> 1$, $\Delta\varphi = \theta - \phi << 1$, Eqn. (3.25) becomes Gaussian as:

$$p_{\Theta}(\Delta\varphi) = \sqrt{\frac{SNR}{2\pi}} e^{-SNR\Delta\varphi^2} \tag{3.27}$$

where the variance for $\Delta\theta$ is given by

$$\sigma_{\Delta\varphi}^2 = \frac{1}{2SNR} . \tag{3.28}$$

This expression is identical to Eqn. (3.10) and the expression presented in Refs. [5, 6]

In order to confirm the theoretically derived PDF with the experimental result, the phase fluctuation of the interference between the reflected beams from the top and bottom surfaces of a coverslip was measured as a function of SNR. The SNR was varied by controlling the integration time of the line scan camera, and all the scanners were off during the measurement. The comparisons between theoretically estimated and experimentally measured PDFs showed excellent agreement (Figure 3.3). The experimental PDFs were obtained by dividing the histograms by the total area such that the integration of the PDFs over the phase space is equal to 1. Based on the measured PDFs, the phase variances were calculated and compared with the theoretical estimation (Figure 3.4). It showed a great correlation, underscoring the importance of SNR for high phase stability.

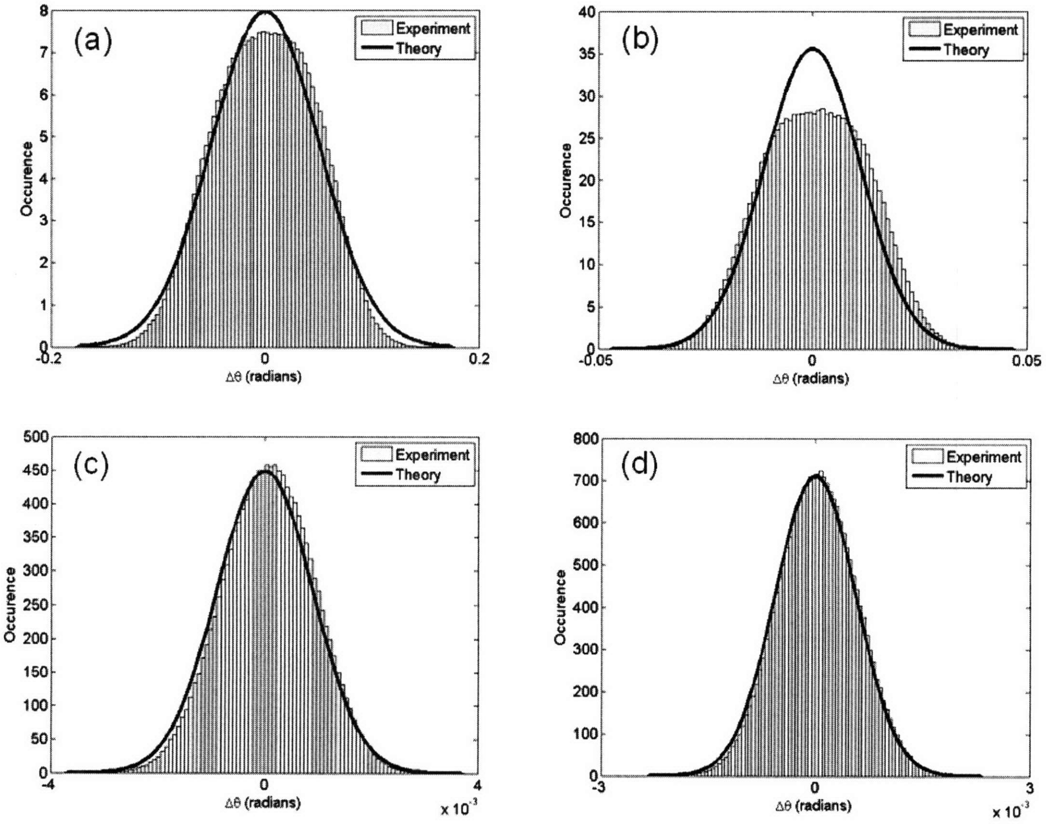

Figure 3.3: Theoretically derived and experimentally measured probability density functions of phase for various SNRs; (a) SNR = 23 dB, (b) SNR = 36 dB, (c) SNR = 58 dB, (d) SNR = 62 dB. The measured PDFs agreed well with the theoretical prediction calculated by Eqn. (3.25).

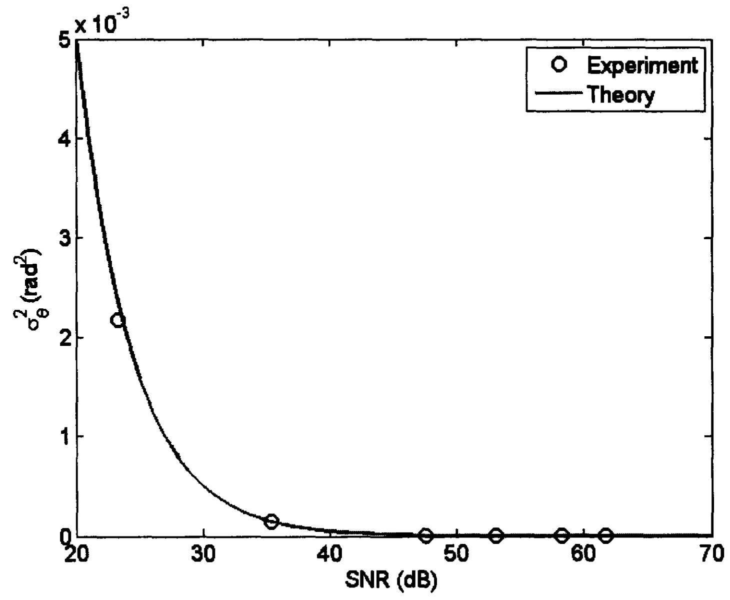

Figure 3.4: The phase noise variance vs. SNR. Excellent agreement between the theory and experimental results can be noted.

We also examined the difference between the generalized phase PDF (Eqn. 3.25) and the Gaussian PDF (Eqn. 3.27). The variance was calculated by

$$\sigma_\theta^2 = \int_{-\pi}^{\pi} \theta^2 p_\Theta(\theta)\,d\theta - \left[\int_{-\pi}^{\pi} \theta\, p_\Theta(\theta)\,d\theta\right]^2 \qquad (3.29)$$

in each case. Figure 3.5(a) shows the calculated phase variance as a function of SNR, along with the percent error in Fig. 3.5(b). As can be seen, at low SNR (SNR < 10 dB), the difference becomes apparent in phase variance, and the percent error is ~5 % at the SNR of 10 dB. In optical path-length, it corresponds to ~0.35 nm difference out of ~14 nm phase sensitivity.

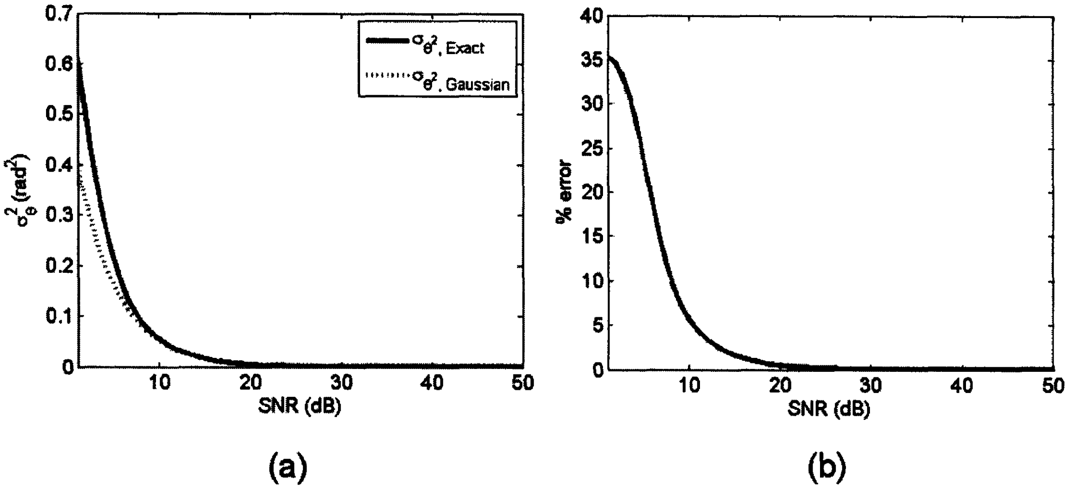

Figure 3.5: The phase noise variance vs. SNR based on the generalized (Eqn. 3.25) and Gaussian (Eqn. 3.27) phase PDFs. The error becomes apparent at SNR < 10 dB.

3.4. SD-OCPM phase stability vs. lateral scanning

In SD-OCPM imaging, the beam continuously raster-scans over a specimen to obtain the amplitude and phase images in the plane of interest. For better phase stability, the stepping mode for phase measurement may be desirable where the beam is stationary during the integration time. However, this scheme requires lateral scanners that exhibit fast transient time response to meet the speed requirement. The galvanometer-driven scanners employed in SD-OCPM have a settling time of ~2 msec, so the stepping mode is not used for typical cellular imaging. Instead, the beam continuously scans over the specimen. Since the beam is not stationary during the measurement, the scanner motion contributes to the noise in the phase measurement.

In order to appreciate the effect of lateral scanning on the phase determination, let us consider the SD-OCPM imaging geometry as illustrated in Figure 3.6, where a Gaussian beam scans by Δx over a random scattering medium during the integration time. The effective beam distribution on the sample, $G(x,y)$ can then be modeled as the convolution of the Gaussian beam function and rect function:

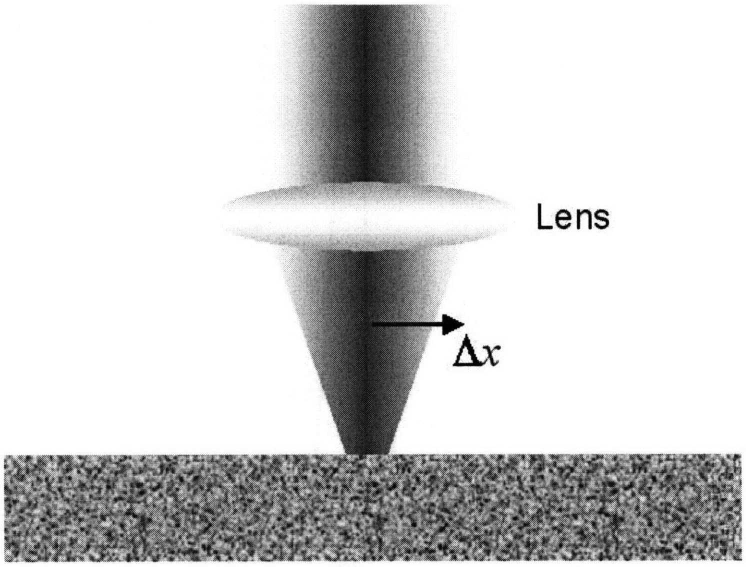

Figure 3.6: SD-OCPM raster-scans across the specimen to acquire the amplitude and phase images of the specimen.

$$G(x,y) = A(\Delta x) \cdot \left[g(x,y) \otimes rect\left(\frac{x}{\Delta x} \right) \right] \tag{3.30}$$

where $g(x,y) = \exp\left[-4\ln 2\left(x^2 + y^2\right)/d_0^2\right]$ with a FWHM diameter of d_0 defined in its intensity distribution. $A(\Delta x)$ is introduced such that

$$S = \int_{-\infty}^{\infty}\int_{-\infty}^{\infty} G(x,y)dxdy = \int_{-\infty}^{\infty}\int_{-\infty}^{\infty} g(x,y)dxdy\,. \tag{3.31}$$

The intensity distribution $g(x, y)$, rather than the field distribution of the probe beam is used to take into account the effect of the mode function imposed by fiber coupling. The amplitude of the back-scattered light received by the fiber is determined by an overlap integral between the scattered field and the mode function, resulting in the dependence on the intensity profile.

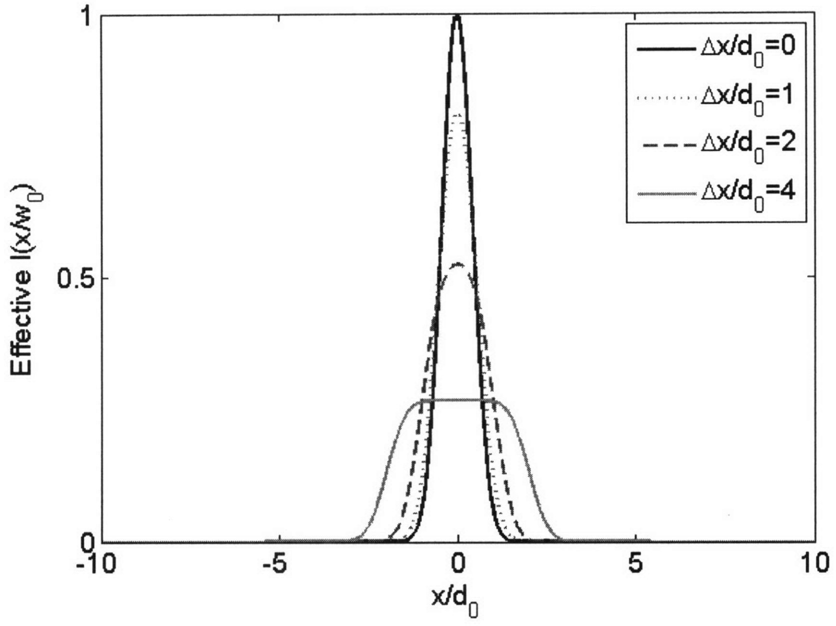

Figure 3.7: Effective beam distributions on the sample for four different normalized displacements.

As noted by Yun *et. al.* [8], the effect of the scanner lateral motion (or equivalently the motion of the specimen) is a modification of the beam profile on the sample from $g(x)$ to $G(x)$. Physically, $G(x)$ represents an enlarged illumination area by the probe beam during the integration time. Figure 3.7 shows examples of the effective intensity distribution of the beam for four different values of normalized displacement, $\Delta x / d_0$. This result implies both the degradation of spatial resolution and the SNR reduction. The spatial resolution degradation is obvious by looking at Figure 3.7. The FWHM diameter is increased by a factor of 1.25 for $\Delta x / d_0 = 1$. The SNR is also expected to decrease because the signal from a particular scatterer in the sample is illuminated and collected during only a fraction of integration time. More rigorously, using the modified beam profile and the expressions in Eqns. (2.3) and (3.10), SNR can be written as

$$\frac{S}{N}=\frac{P_r P_{s,n}}{P_r+\sum_n P_{s,n}} \propto \frac{\left|\Gamma(z-z_n)\left\{|r_R||r_{S,n}|\int_{-\infty}^{\infty}\int_{-\infty}^{\infty}G(x,y)e^{j\theta(x,y)}dxdy\right\}\right|^2}{\left|\Gamma(z)|r_R|^2\right|^2+\left|\Gamma(z)\sum_n |r_{S,n}|^2\right|^2} \tag{3.32}$$

Here, it was assumed that the reference and sample have a spatially independent reflectivity, and the sample has a random phase variation across the space, i.e, $\langle\theta(x,y)\theta(x',y')\rangle=\frac{\pi^2}{3}\delta(x-x',y-y')$. For $P_R/P_s>>1$ and $P_R\sim const$, one can see

$$\frac{S}{N}\propto|\Gamma(z-z_n)|^2\left\{|r_R|^2|r_{S,n}|^2\int_{-\infty}^{\infty}\int_{-\infty}^{\infty}G^2(x,y)dxdy\right\} \tag{3.33}$$

i.e,, the SNR is directly proportional to $\int_{-\infty}^{\infty}\int_{-\infty}^{\infty}G^2(x,y)dxdy$.

Figure 3.8 shows the SNR reduction due to the lateral beam scanning obtained by the theory and the experiment. For measurement, a scattering medium made of Titanium oxide mixed amorphous glass was imaged, and the SNR was calculated based on the average of 100 A-line profiles. It can be seen that there is a great correlation between the theory and experimental results.

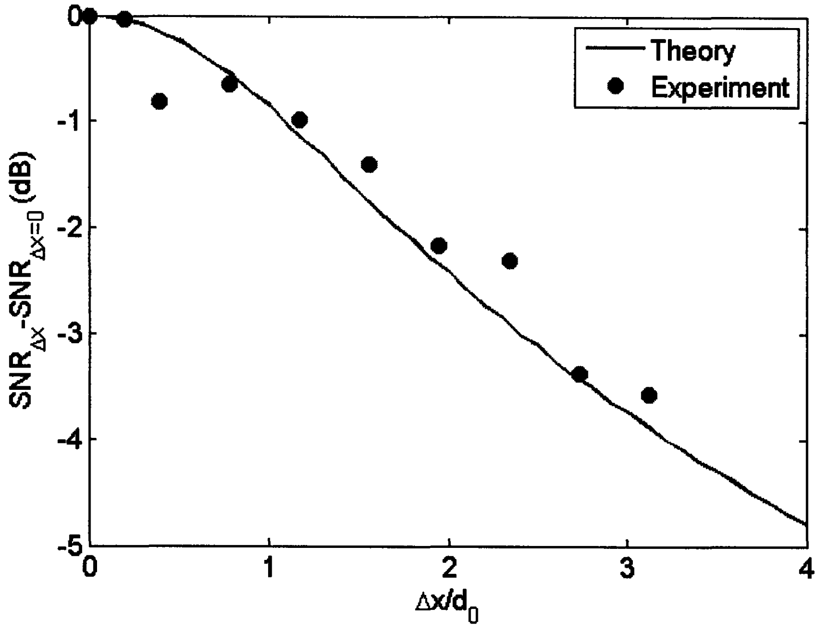

Figure 3.8: SNR reduction cause by the lateral scanning. The SNR was calculated based on the average of 100 A-line profiles for each normalized displacement. It can be noted that the theory and experimental results agreed well.

In a typical SD-OCPM cellular imaging (FOV: 86 μm × 86 μm, 256 × 256 pixels, NA: 0.75), the beam is scanned by $\Delta x / d_0 \sim 0.8$ during the integration time as a compromise between the spatial resolution, the acquisition speed, and SNR. As discussed in Chapter 2, this displacement is larger than the intrinsic motion jitter of the galvanometer scanners, so the main noise source in SD-OCPM imaging is the beam displacement during the integration time.

3.5. SD-OCPM phase stability vs. axial scanning

For high-resolution 3D imaging of transparent specimen, SD-OCPM raster-scans a focal volume at a depth location acquiring a two-dimensional image, and positions the focal volume to another depth of interest for the subsequent imaging. The position of the focal volume along the optical axis is controlled by a piezo-driven transducer (PZT) with an axial range of 250 μm. Unlike the lateral scanning which involves the continuous displacement of the beam, the axial position of the focal volume is supposed to be stationary during the integration time, so the relative motion jitter between the objective and the specimen is the main noise source.

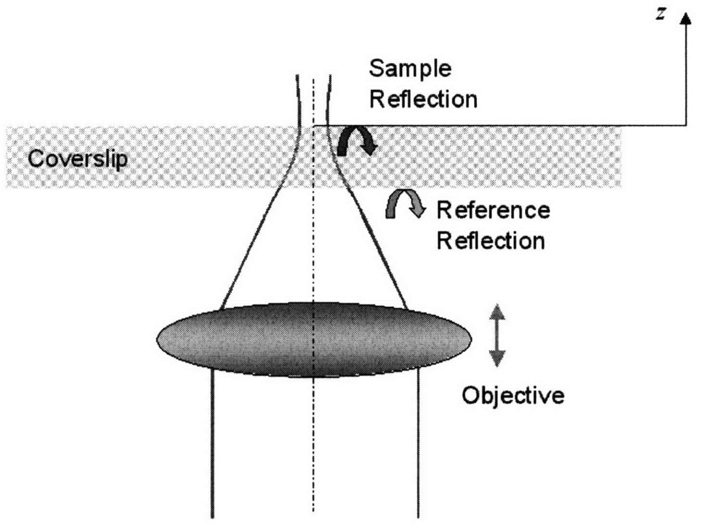

Figure 3.9: A Gaussian beam is focused on the top surface of a coverslip, and SD-OCPM interferometer measures the phase of the interference of light reflected from the top and bottom surfaces of the coverslip as scanning the objective.

To understand the phase change caused by the relative motion jitter in the axial direction, we consider the case depicted in Figure 3.9, where a Gaussian beam is focused onto the top surface of a coverslip. The reference and measurement electric fields reflected from the surfaces can be modeled easily by use of the Gaussian beam solution to the Maxwell's equations. The fundamental Gaussian-beam solution in the homogeneous medium is given by [9]

$$E(x,y,z) = E_0 \frac{w_0}{w(z)} \exp\left\{-i[kz-\eta(z)] - \left(x^2+y^2\right)\left(\frac{1}{w^2(z)} + \frac{ik}{2R(z)}\right)\right\} \quad (3.34)$$

where the parameters are defined as

$$w^2(z) = w_0^2\left(1 + \frac{z^2}{z_0{}^2}\right) \tag{3.35}$$

$$R(z) = z\left(1 + \frac{z_0^2}{z^2}\right) \tag{3.36}$$

$$\eta(z) = \tan^{-1}\left(\frac{z}{z_0}\right) \tag{3.37}$$

$$z_0 = \frac{1}{2}kw_0^2. \tag{3.36}$$

Here, z denotes the distance from the focal plane where the wavefront is planar, and w_0 is the $1/e^2$ radius of the intensity distribution at the focal plane.

In a fiber-based SD-OCPM implementation, the reflected beams from the surfaces are coupled back to the single-mode fiber, so the reflected fields are superimposed by the mode function given by

$$f(x,y) = E_0 \exp\left[-\frac{\left(x^2 + y^2\right)}{w_0^2}\right]. \tag{3.38}$$

Therefore, the mode-coupled reference and measured fields are

$$U_R = \int_{-\infty}^{\infty}\int_{-\infty}^{\infty} E_R(x, y, z_R) \cdot f(x, y) dxdy \tag{3.39}$$

$$U_S = \int_{-\infty}^{\infty}\int_{-\infty}^{\infty} E_S\left(x', y', z_S\right) \cdot f\left(x', y'\right) dxdy, \tag{3.40}$$

and further evaluation of these integrals gives us

$$U_R = E_0^2 \frac{\pi w_0}{w(z_R)}\left(\frac{1}{w^2(z_R)} + \frac{1}{w_0^2} + \frac{ik}{2R(z_R)}\right)^{-1} \exp\{-i[kz_R - \eta(z_R)]\} \tag{3.41}$$

$$U_S = E_0^2 \frac{\pi w_0}{w(z_S)} \left(\frac{1}{w^2(z_S)} + \frac{1}{w_0^2} + \frac{ik}{2R(z_S)} \right)^{-1} \exp\{-i[kz_S - \eta(z_S)]\}. \tag{3.42}$$

The phase of the interference between the reference and measurement fields, U_R and U_S can then be evaluated by

$$\phi = \tan^{-1}\left[\frac{\mathrm{Im}(U_R^* U_S)}{\mathrm{Re}(U_R^* U_S)} \right]. \tag{3.43}$$

Intuitively, any relative displacement between the coverslip and the objective should result in no phase variation if the coverslip is illuminated by a plane wave. This fact can be also observed in the model. By definition, the plane wave has an infinite wavefront curvature, i.e., $R(z_S) = R(z_R) \to \infty$, so, for a constant $z_S - z_R$, the phase remains constant at $\phi = k(z_S - z_R) - (\eta(z_S) - \eta(z_R))$.

Based on this model, the numerical simulation was performed and confirmed by the experimental result. SD-OCPM beam was focused onto the top surface of the coverslip (No. 0) with a FWHM diameter of ~0.6 μm, and the phase was recorded as the objective scans from –1.25 μm to 1.25 μm along the optical axis. Figure 3.10 shows the phase change as a function of the displacement of the objective. The simulation and experimental results had different offsets due to the uncertainty of refractive index and physical thickness of the coverslip, but were subtracted to overlap two curves. The results showed an excellent agreement between the theory and experiment in that the slopes of the phase change are approximately the same as ~0.435 rad/μm. Because of the use of focused beam with a high NA objective, the phase varied significantly even with the small relative displacement between the coverslip and objective.

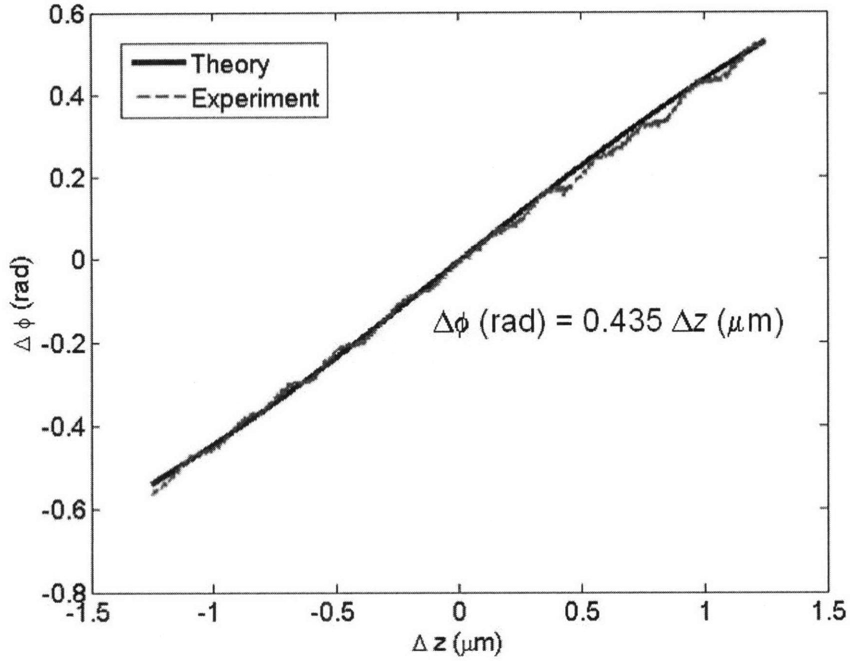

Figure 3.10: Calculated and measured phase change due to the displacement of the objective. For a probe beam with a FWHM diameter of ~0.6 μm, the phase change is approximated as ~0.435 rad/μm.

In the SD-OCPM implementation, the objective is mounted onto the PZT transducer, which is controlled by the PI controller (E-665.CR LVPZT controller, Physik Instrumente). SD-OCPM acquisition program sends out 16-bit analog waveform to the PZT controller, which then applies input signal to the actuator accordingly.

Inside the PZT controller, a capacitive sensor reads the position of the objective for a feedback control, and this signal can be examined through the MONITOR channel in the front panel. The MONITOR signal was measured at a sampling rate of 500 Hz by use of a low noise digital oscilloscope. The data was in Volts, and converted into displacement by multiplying the scale factor (25 μm/V). Figure 3.11 shows the motion jitter of the PZT measured for 20 seconds. The spectral analysis of this measurement showed a white-noise characteristic. The standard deviation was measured as ~6 nm. Based on this measurement, the phase stability due to the axial motion can be estimated by the relationship

$$\sigma_{\Delta\phi} \sim 0.435 \cdot \sigma_{\Delta z} \qquad (3.44)$$

, which gives ~0.2 nm in optical path-length.

In a separate estimation for an objective with an NA of 0.5, the phase change was estimated as ~0.15 rad/μm, and the ~6 nm displacement noise in the objective results in the phase stability of ~57 pm in air, which is close to that reported in Ref. [10]

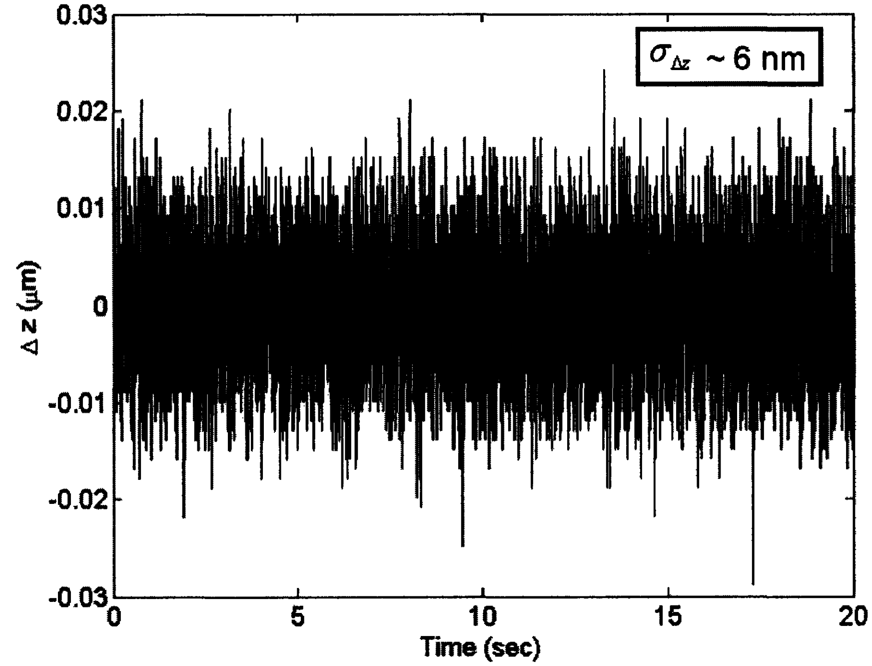

Figure 3.11: Measured motion jitter of the PZT transducer for 20 seconds. The standard deviation was obtained as ~6 nm.

3.6. Summary

The phase noise performance of the SD-OCPM setup was discussed by considering the contributions from the interferometer detection and the scanners. By use of spectrally dispersed detection of interferograms, it was found that SD-OCPM operates in shot-noise limited regime, and in which case, the factors that determine the SNR were described.

The importance of SNR was elucidated by examining its role in the phase measurement. We obtained a functional relationship of the phase PDF with SNR, and confirmed our theory with the experimental results. In short, the higher SNR, the higher phase precision one can achieve.

The effects of the scanner dynamics to the phase stability were also discussed. The transverse displacement of the beam during the integration time leads to degradation both in spatial resolution and SNR. SNR reduction was quantitatively discussed in theory and experiment. The main noise source in terms of axial direction is the relative motion jitter induced by the PZT transducer. We derived a mathematical model based on Gaussian beam solution, and estimated the magnitude of phase change as a function of the displacement in the axial direction. For a high-resolution 3D imaging, it necessitates a high spatial resolution, but it puts stricter requirement on the noise performance of the scanners employed.

3.7. Reference

1. N. Nassif, B. Cense, B.H. Park, S.H. Yun, T.C. Chen, B.E. Bouma, G.J. Tearney, and J.F.de Boer, "*In vivo human retinal imaging by ultrahigh-speed spectral domain optical coherence tomography,*" Optics Letters. **29,** 480-482 (2004).

2. W.V. Sorin and D.M. Baney, "*A simple intensity noise reduction technique for optical low-coherence reflectometry,*" IEEE Photonics Technology Letters. **4,** 1404-1406 (1992).

3. A.F. Fercher, W. Drexler, C.K. Hitzenberger, and T. Lasser, "*Optical coherence tomography - principles and applications,*" Reports on Progress in Physics. **66,** 239-303 (2003).

4. J.F.de Boer, B. Cense, B.H. Park, M.C. Pierce, G.J. Tearney, and B.E. Bouma, "*Improved signal-to-noise ratio in spectral-domain compared with time-domain optical coherence tomography,*" Optics Letters. **28,** 2067-2069 (2003).

5. M.A. Choma, A.K. Ellerbee, C. Yang, T.L. Creazzo, and J.A. Izatt, "*Spectral-domain phase microscopy,*" Optics Letters. **30,** 1162-1164 (2005).

6. B.H. Park, M.C. Pierce, B. Cense, S.-H. Yun, M. Mujat, G. Tearney, B. Bouma, and J.F.de Boer, "*Real-time fiber-based multi-functional spectral-domain optical coherence tomography at 1.3 μm,*" Optics Express. **13,** 3931-3944 (2005).

7. J.W. Goodman, *Statistical Optics*. 1985, New York: John Wiley & Sons, Inc.

8. S.H. Yun, G.J. Tearney, J.F.de Boer, and B.E. Bouma, "*Motion artifacts in optical coherence tomography with frequency-domain ranging,*" Optics Express. **12,** 2977-2998 (2004).

9. A. Yariv, *Optical Electronics in Modern Communications*. 5 ed. 1997, New York: Oxford University Press.

10. C. Joo, K.H. Kim, and J.F.de Boer, "*Spectral-domain optical coherence phase and multiphoton microscopy,*" Optics Letters. **32,** 623-62 (2007).

Chapter 4:

SD-OCPM + MPM: Integration of quantitative phase-contrast and multi-photon fluorescence imaging modalities

4.1. Introduction

Spectral-domain optical coherence phase microscopy (SD-OCPM) employs a common-path spectral-domain optical coherence interferometer to achieve highly sensitive detection of phase changes. Owing to the improved sensitivity and speed of spectral-domain OCT [1-3], SD-OCPM exhibits sub-nanometer phase sensitivity and is capable of producing quantitative phase images on biological specimens.

While SD-OCPM as well as other phase imaging modalities described in Chapter 1 produces high contrast images of transparent specimens without the need for exogenous contrast agents, the lack of specificity makes it difficult to understand and interpret the images, especially for complex biological specimens, i.e., cells. The contrast provided by the phase images arises from the structural variation in the size and the refractive index inside the sample, not from a signature of particular molecules. On the other hand, the advent of green fluorescent protein (GFP) and its derivatives has significantly reformed fluorescence microscopy and its use in cell biology because of the availability of the intrinsic fluorescent specimens with much lower photo-toxicity [4]. The integration of fluorescence imaging capability with quantitative phase contrast method therefore not only provides a means to interpret the quantitative phase images, but also offers complementary information on the composition and functions of the specimen. Recently, intensity-based OCM was combined with multi-photon microscopy (MPM) [5, 6], and diffraction phase and fluorescence microscopy was also demonstrated [7].

In this Chapter, we present a novel multi-modal microscope capable of simultaneous quantitative phase contrast and multi-photon fluorescence imaging by incorporating multi-photon microscopy into SD-OCPM. The detailed description for MPM implementation and performance is presented, followed by MPM and OCPM images simultaneously obtained on stained cells.

4.2. Experimental setup: hardware

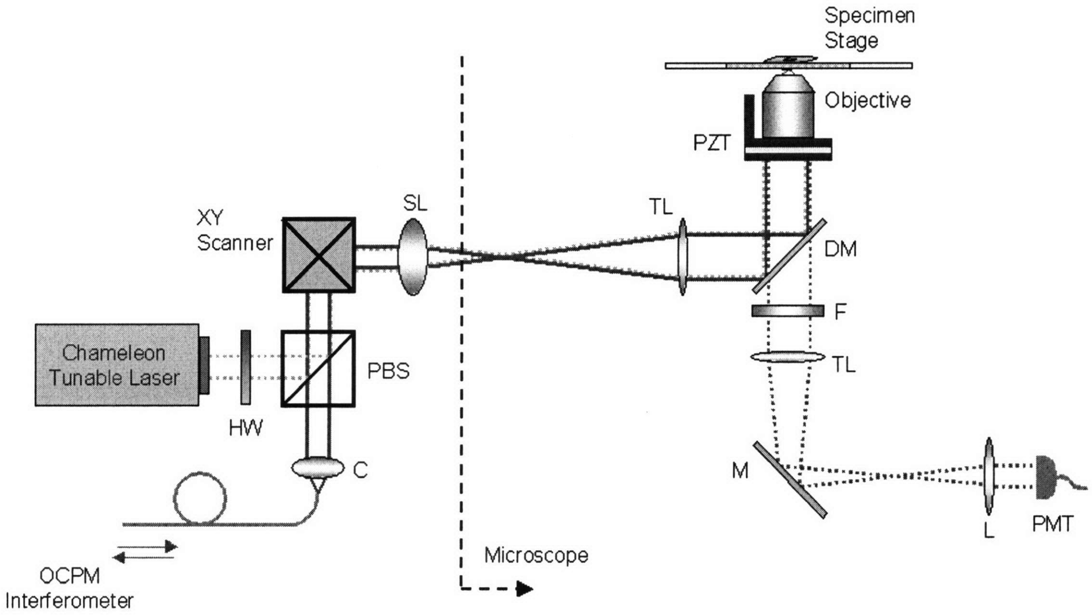

Figure 4.1: Experimental setup for SD-OCPM + MPM; (HW) half-wave plate; (C) collimator; (PBS) polarizing beam splitter; (SL) scan lens; (TL) tube lens; (PZT) piezo-electric transducer; (DM) dichroic mirror; (F) filter; (M) mirror; (L) lens; (PMT) photo-multiplier tube.

The experimental setup for the combined SD-OCPM + MPM is depicted in Figure 4.1. In addition to the SD-OCPM beam path described in Chapter 2, a tunable Ti:Sapphire pulsed laser with a pulse duration of 140 fsec and 90 MHz repetition rate (Chameleon™, Coherent Inc., CA) was employed for MPM setup. The solid and dashed lines represent the beam path for OCPM and MPM, respectively. The half-wave plate in front of the Chameleon tunable laser combined with the polarizing beam splitter offers a means to control the beam power at the specimen (1 mW ~ 10 mW). Combined at the polarizing beam splitter (PBS), both OCPM and MPM beams pass through the XY galvanometer beam scanners, and are introduced to the microscope through its back port. The beam is then deflected by the dichroic mirror and focused onto a specimen via a microscope objective.

For MPM imaging, the fluorescence photons emitted in the backward direction are collected by the microscope objective, and transmit through the dichoric mirror and an emission filter for a desired wavelength. The beam is then guided to the side port by the flip mirror. Outside the microscope, a lens (L) with a focal length of 75 mm is positioned at a focal length away from the intermediate image plane such that the beam is collimated and detected by the PMT in the Fourier plane. The beam diameter, D_L, incident on the PMT is determined by the ratio of the focal lengths of the lens (L) to the tube lens and the size of the back-aperture of the objective (D_{OBJ}), i.e., $D_L = D_{OBJ} \cdot (f_L / f_{TL})$. For a 20× microscope objective, D_L is approximated as 3.75 mm, smaller than the active detection area of the PMT (8 mm).

The PMT module (Hamamatsu Corp., H7155-20) is a compact photon counting head device consisting of a metal package PMT equipped with a high-speed photon counting circuit and a high-voltage supply. It has an internal prescaler of division by four, and improves the count linearity four-fold compared to its un-prescaled version. The PMT module sends out TTL pulses corresponding to incident photons, and the counter board (NI PCI-6602) in the host computer detects the number of pulses based on the gate signal provided by the pixel rate in the user program. The counter board can measure the pulses up to 80 MHz with a size of 32 bit. The PMT has a spectral range of 300 nm ~ 650 nm, which does not overlap with that of OCPM laser source.

Figure 4.2 shows the pictures of the back and front views of the SD-OCPM + MPM setup in the laboratory. The microscope and all the optical components are covered by the enclosure to avoid any stray light and noise from the environment.

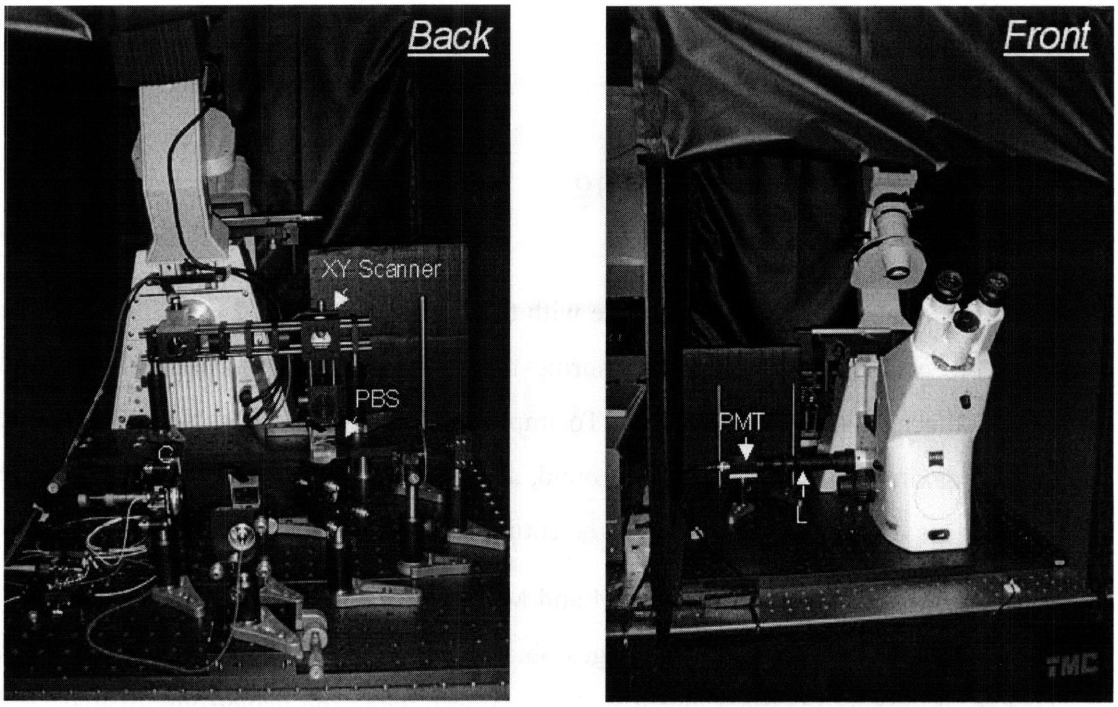

Figure 4.2: Back and front side views for SD-OCPM + MPM setup. (C) collimator; (PBS) polarizing beamsplitter; (PMT) photo-multiplier tube. All the optical components and microscope are covered by the enclosure to avoid any stray light from the environment.

4.3. Experimental setup: software

In order to acquire SD-OCPM and MPM images simultaneously, the SD-OCPM acquisition program was modified accordingly. Besides the task described earlier, the counter board initialization was included in the initialization code. A counter in the PCI-6110 board receives a frame triggering signal from PCI-6733, and sends out the gating TTL pulses with a length of number of pixels to the counter board (PCI 6602). The counter board counts the number of pulses generated by the PMT module, which is then saved into a node structure in a separate link list. A new display was added to visualize the MPM image during the measurement. The range and offset of the image can be changed through the main panel of the program to vary the image contrast *in situ*.

4.4. MPM image processing

MPM image processing was done with the codes implemented in MATLAB. The images were generated simply by measuring the number of photon counts detected in each pixel during the integration time. To improve the contrast, the offset is set to the median or maximum value of the background, and the dynamic range is usually set to the 75 % of the maximum count value over the entire FOV.

The co-registration of SD-OCPM and MPM images was conducted separately by performing cross-correlation of the images obtained by two imaging modalities. Ideally, the images should be identical, but it is the case only when the wavefronts of two laser beams at the back focal plane of the objective are identical, which is difficult to achieve in practice. Generally, to achieve the best co-registration, a fluorescent resolution target (Fluorescent USAF 1951 target, Edmund Optics, NJ) was imaged to produce high contrast SD-OCPM intensity and MPM fluorescence images, and the number of pixels (typically less than 10 pixels in each direction) to shift is determined before recording the cellular specimens.

4.5. Performance characterization

1.1.13. TPM response curve

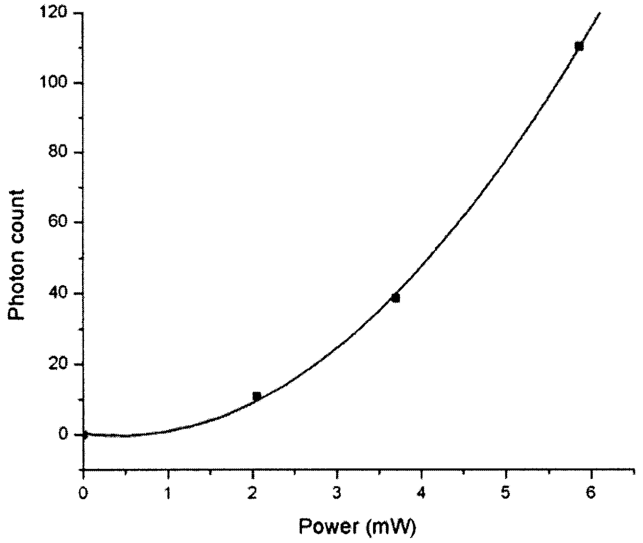

Figure 4.4: Response of emission photons vs. excitation power. It can be seen that a quadratic dependence of emission photons on the excitation power confirms two-photon absorption of the fluorophores.

Two-photon absorption of fluorescent molecules is a quadratic process, and the number of photons absorbed by a fluorophore per pulse, n_a, is given by [8]

$$n_a \approx \frac{p_0^2 \delta}{\tau_p f_p^2} \left(\frac{NA^2}{2\hbar c \lambda} \right)^2 \tag{4.1}$$

where τ_p is the pulse duration, δ is the fluorophore's two-photon absorption cross-section at wavelength λ, p_0 is the average laser power, f_p is the pulse repetition rate, NA is the numerical aperture of the focusing objective, and $\hbar$ and c are Planck's constant and the speed of light, respectively. Eqn. (4.1) demonstrates that, for the same average laser power and repetition rate, the excitation probability is increased by use of higher NA and by reducing the pulse width of the laser.

The ideal approach to confirm the proper function and to characterize the efficiency of the current TPM instrumentation is measuring the number of photons absorbed by a fluorophore and comparing it with the number estimated by Eqn. (4.1).

However, this evaluation requires the experimental characterization of the laser employed in the TPM setup as well as the two-photon absorption cross-section of the fluorescent molecules itself. To confirm the detection of two-photon absorption of our TPM setup, we examined the response curve of fluorescence emission as a function of excitation power.

The red-fluorescent polystyrene microspheres in water (R25, 0.028 μm in diameter, Duke Scientific Corp.) were used as fluorescent specimen, and the emission signal was measured as a function of the laser power at the specimen. Figure 4.4 shows the response curve of emission photons as a function of excitation beam power. The emission photons demonstrate a quadratic dependence on the excitation power, confirming the two-photon absorption of the fluorescent molecules.

1.1.14. Dynamic range

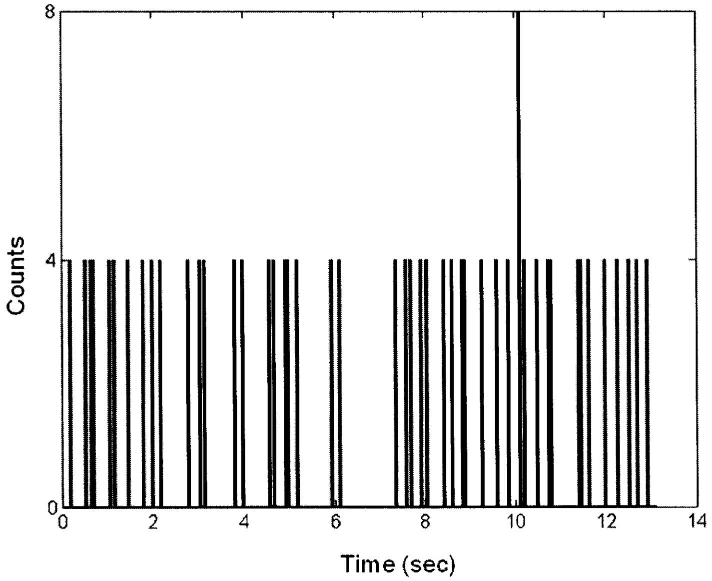

Figure 4.5: Measured dark count rate. The count was multiplied by four to take into account the prescaler in the PMT module.

Our MPM setup operates in photon-counting mode to achieve higher signal-to-background ratio and excellent linearity over a wide range. The lower limit of the count rate linearity is determined by the dark current rate. We measured the dark count rate of our setup by measuring the counts from the PMT about 30 minutes after it was turned on in the room temperature (~25 °C). Figure 4.5 shows the measured dark count at a pixel rate of 10 kHz. The count was multiplied by four to take into account the pre-scale factor in the PMT module. The average measured dark count rate was ~128 Hz, which is consistent with the specification from the manufacturer.

The maximum count rate, on the other hand, depends on the pulse-pair resolution of the photon-counting module and on the maximum pulse rate measurable by the counter board. In our MPM setup, the pulse-pair resolution is 10 ns (100 MHz), whereas the maximum pulse rate that can be measured by the counter board is 80 MHz. More stringent condition is set by the pulsed excitation characteristic for MPM. If it is assumed that the counter cannot distinguish two photons arriving at the same time, the counter should receive less than a single emission photon upon the single pulse excitation. In that case, one can conclude that the maximum count rate is 90 MHz because the pulse repetition rate of Chameleon source is 90 MHz. However, most events in the photon-counting regime usually occur at random obeying the Poisson distribution, and so there is a chance that more than one photon can arrive at the detector. To avoid this error, it is safe to operate at a lower level of power such that the count rate is about one tenth of the pulse repetition rate, i.e, 9 MHz.

1.1.15. Resolution

Unlike a confocal microscope, TPM offers intrinsic 3D imaging capability based on its nonlinear excitation probability. Eqn. (4.1) indicates that the probability is proportional to the square of excitation laser power, implying that two-photon absorption is the highest at the focal volume, where the photon flux is the highest. The spatial resolution in lateral and axial dimensions can be estimated by Eqns (2.9) and (2.10), respectively.

The spatial resolution of our TPM was examined experimentally for the objectives with NAs of 0.5 (Plan-NEOFLUAR, 20×/0.5, Zeiss) and 0.75 (LD Plan-NEOFLUAR, 63×/0.75, Zeiss). For the characterization, fluorescent microspheres (0.2 μm in diameter) mixed with agarose gel was used as a specimen, and the averaged value for 10 measurements was taken as the representative resolution. The measured lateral and longitudinal resolution were 0.7 μm and 4.8 μm for 0.5 NA, and 0.5 μm and 2.5 μm for 0.75 NA, respectively. Figure 4.6 shows an exemplary TPM fluorescence image obtained with 0.75 NA objective and its corresponding PSF.

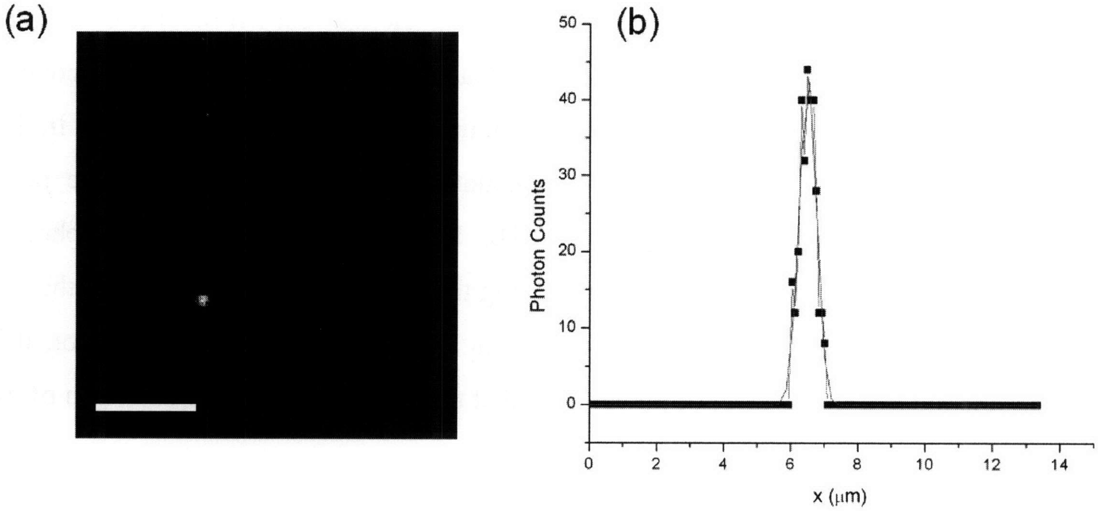

Figure 4.6: TPM fluorescence image of fluorescent microsphere mixed with agarose gel (a), and its corresponding PSF (b). The image was acquired with the objective with an NA of 0.75, and the lateral resolution was measured as 0.5 μm. The scalebar in (a) denotes 10 μm.

4.6. Experimental result: Simultaneous SD-OCPM and TPM imaging on fixed cells

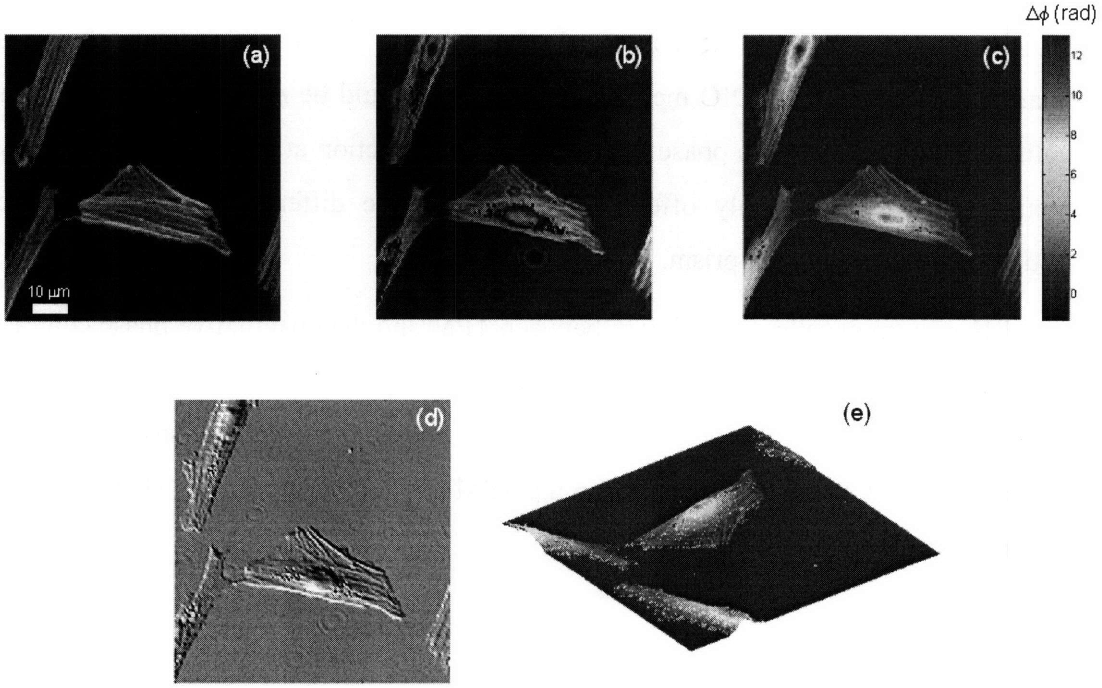

Figure 4.7: Images of fixed and stained muntjac skin fibroblast cells. Two-photon fluorescence image (a) shows the distribution of actin filaments labeled with Alexa Fluor 488 phalloidin. The images (b) and (c) are the intensity and quantitative phase contrast images obtained in reflection with SD-OCPM, respectively. The color bar to the right of the phase contrast image denotes the phase distribution in radians. The computed phase gradient and 3D representation of the phase image are shown in (d) and (e). The scale bar represents 10 μm.

The simultaneous quantitative phase and multi-photon imaging capability of SD-OCPM + MPM was assessed by imaging prepared muntjac skin fibroblast cells (FluoCells #6, Invitrogen, CA). For TPM imaging, the center wavelength of the Chameleon tunable laser was set to 800 nm. The pixel rate or A-line rate was 10 kHz, and the total acquisition time was ~5 seconds for an image size of 232×232 pixels. Figure 4.7

shows the images acquired by SD-OCPM + MPM. The TPM image (a) clearly shows the distribution of actin filaments inside the cells, labeled with Alexa Fluor 488. The two-photon excitation in nuclei labeled with TO-PRO®-3 was not observed because the two-photon absorption cross-section of the flurophore is low at the wavelength used for imaging. Figure 4.7 (b), (c), (d) represent the intensity, phase, and phase difference images of the same cells, respectively. The phase gradient image was obtained by taking two-dimensional gradient of the phase image and adding the vectors in each pixel to provide a projection view at 45 degrees. In some sense, the phase gradient scheme is similar to the conventional DIC method. However, it should be noted that our image is quantitative, and can provide phase difference in any direction at any sectional plane by computation, while DIC only offers a qualitative phase difference map in the one direction determined by DIC prism.

There is an excellent correlation between TPM and the quantitative phase contrast images in aspects of actin filament distribution, which suggests label-free visualization of actin filaments by SD-OCPM. Moreover, the nuclei and other subcellular structures were observed in SD-OCPM images, but not in the TPM image. Figure 4.7 (e) shows the 3D representation of the phase image.

4.7. Summary

A multi-modal microscope capable of simultaneous quantitative phase contrast and multi-photon fluorescence imaging was developed by incorporating MPM capability into the SD-OCPM. The lateral and longitudinal resolution of the MPM and its dynamic range in photon counting were characterized. Simultaneous imaging on fixed and stained muntjac skin fibroblasts showed that the morphological information in the quantitative phase contrast and the computed phase gradient images agreed in terms of the actin filament distribution observed in the TPM image. Moreover, the phase contrast image revealed the quantitative information of unstained subcellular structures, which can be utilized as complementary information in biological studies.

4.8. Reference

1. Leitgeb, R., C.K. Hitzenberger, and A.F. Fercher, *Performance of fourier domain vs. time domain optical coherence tomography.* Optics Express, 2003. **11**: p. 889-894.

2. de Boer, J.F., et al., *Improved signal-to-noise ratio in spectral-domain compared with time-domain optical coherence tomography.* Optics Letters, 2003. **28**(21): p. 2067-2069.

3. Choma, M., et al., *Sensitivity advantage of swept source and Fourier domain optical coherence tomography.* Optics Express, 2003. **11**(18): p. 2183-2189.

4. Pierce, D.W., N. Hom-Booher, and R.D. Vale, *Imaging individual green fluorescent proteins.* Nature, 1997. **388**: p. 338

5. Beaurepaire, E., et al., *Combined scanning optical coherence and two-photon-excited f luorescence microscopy* Optics Letters, 1999. **27**: p. 969-971

6. Vinegoni, C., et al., *Integrated structural and functional optical imaging combining spectral-domain optical coherence and multiphoton microscopy.* Applied Physics Letters, 2006. **88**: p. 053901.

7. Park, Y., et al., *Diffraction phase and fluorescence microscopy.* Optics Express, 2006. **14**(18): p. 8263.

8. So, P.T.C., et al., *Two-photon excitation fluorescence microscopy.* Annual Review of Biomedical Engineering, 2000. **02**: p. 399-429.

Chapter 5:
SD-OCPM for cellular dynamics investigation

5.1. Introduction

Quantitative measurement of cellular structures and dynamics at its diverse physiological conditions and metabolic stages is of great importance in a broad range of biological and medical applications, ranging from the understanding of biological processes to cellular disease diagnosis and assessment of drug efficacy and delivery [1-4].

One of the distinctive and powerful features of SD-OCPM is its sensitivity to minute variations of cellular structures, allowing for access to distributions and fluctuations in amplitude and phase inside the specimens. Despite its thin and small size (on the order of tens of microns), cells are complex structures, with extra- and intracellular dynamics ranging over length scales from several nanometers to microns. SD-OCPM is an attractive technique for studying these tiny but important processes in the extracellular and intracellular regimes.

In this Chapter, we describe SD-OCPM as a tool for quantitative investigation of cellular dynamics. We first propose a SD-OCPM field-based dynamic light scattering technique (F-DLS) that is able to measure parameters related to the motion of scattering particles inside a focal volume. An autocorrelation function based on the complex-valued SD-OCPM interference signal is described, from which the physical parameters regarding the dynamics can be extracted. The feasibility of SD-OCPM F-DLS is first evaluated by Brownian motion measurement, followed by demonstration of intracellular dynamics detection in ovarian cancer cells. We show the existence of different diffusive regimes in the intracellular dynamics, and measure the change in intracellular dynamics caused by ATP-depletion and introduction of an anti-cancer drug, Colchicine.

SD-OCPM imaging is further used to quantify slow dynamics of cellular specimen. Based on the optical sectioning capability of SD-OCPM, we present images of cells at different sectioning planes and in different physiological conditions, We show dynamic and independent sub-domains inside the cells that fluctuate at various dominant frequencies, frequency contents, and magnitude of changes.

5.2. SD-OCPM for field-based dynamic light scattering

Dynamic light scattering (DLS), also known as Quasi-elastic Light Scattering (QELS) and Photon Correlation Spectroscopy (PCS), is a well-established technique for measuring translational, rotational, and internal motions of small particles of sizes over the range of a few nanometers to a few microns in suspension [5, 6].

In DLS, a coherent source of light such as laser is directed at the moving particles. Light scattered by the particles at a particular detection angle to the incident beam is collected and measured at a detector where photons are converted to electrical pulses. Particles undergoing Brownian motion modulate the amplitude and phase of the scattered light, causing fluctuations in the scattered light intensity. This fluctuation in scattered light intensity has a time scale that is related to the speed of the movement of the particles, and information about the sample properties can be extracted from the power spectrum or temporal correlation function of the detected signal.

Until now, DLS information has been obtained by analysis of the intensity of the scattered light. Here, we explore the feasibility of employing an electric-field based technique to measure diffusion of small particles, essentially by applying SD-OCPM interferometry. Field-based DLS (F-DLS) by SD-OCPM has several notable features.

First, we can achieve localized measurement of diffusion of particles. The measurement volume in SD-OCPM is determined by both the focusing optics and coherence gate, which can be as small as ~1 femtoliter. Since it is based on low-coherence interferometry that has optical-path length sensitivity, the measurement is confined to within the confocal and coherence gates, and largely operates in the single scattering regime. Secondly, the use of a common-path interferometer enables us to obtain stable phase information of the scattered light. As will be shown later, the availability of stable and reliable phase information of the scattered light allows us to access an important parameter, time-averaged displacement of particles.

5.2.1. Theoretical description

We begin with a basic theoretical formulation based on conventional DLS theory. The derivation presented here is based on the discussion in Refs [5, 7].

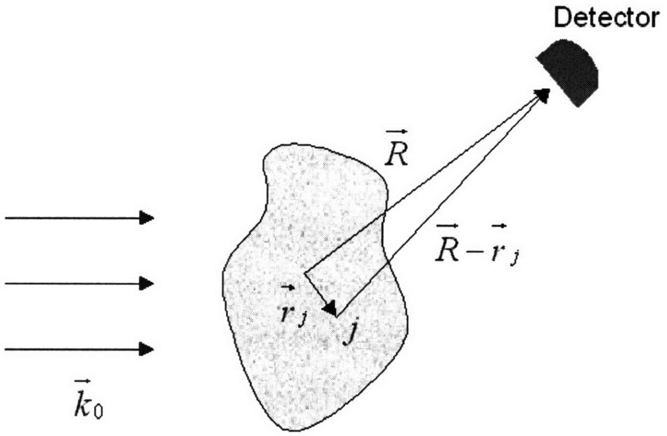

Figure 5.1: The total radiated field at the detector is the superposition of the fields scattered from the particles at position $\vec{r_j}$ with respect to the center of the scattering volume. The detector is at position $\vec{R}$ with respect to the center of the scattering volume.

Consider a dilute solution of N colloidal particles. We will denote the position of each particle j, where $1 \leq j \leq N$, as a function of time by $\vec{r_j}(t)$. Coherent light with wavevector $\vec{k_0}$ illuminates the sample and each photon is assumed to scatter at most once, i.e., single scattering limit. Light that is scattered through an angle θ will subsequently have a different wavevector, $\vec{k_s}$. The scattering wave vector, $\vec{q} = (\vec{q}_x, \vec{q}_y, \vec{q}_z)$, is then defined to be

$$\vec{q} \equiv \vec{k_s} - \vec{k_0}. \tag{5.1}$$

Under the assumption of quasi-elastic scattering, $\left|\vec{k_s}\right| \approx \left|\vec{k_0}\right|$, in which case the magnitude of $\vec{q}$ is given by

$$q \equiv 2k_0 \sin\left(\frac{\theta}{2}\right), \tag{5.2}$$

with θ, the angle between $\vec{k_0}$ and $\vec{k_s}$. If the magnitude of the electric field of the laser light scattered from a particle j is denoted by E_j, then the amplitude of total electric field, E_S, from the sample can be written as the superposition of the scattered fields from all N particles (Figure 5.1):

$$E_S(t) = \exp(ik_s R)\sum_{j=1}^{N} E_j \exp\left[i\vec{q}\cdot\vec{r_j}(t)\right]. \tag{5.3}$$

where R denotes the distance from the center of the scattering volume to the detector plane. The constant pre-factors were ignored for simplicity. The argument in the exponential represents the phase shift introduced by the scattering and depends on the position of each particle. Because the position of each particle is a function of time, the phase of the scattered electric field from each particle varies as a function of time. If the magnitude of the scattered light does not change in time, the intensity fluctuation in the scattered light is purely due to the random motion of particles in suspension, which is the main quantity of investigation for conventional dynamic light scattering technique.

In SD-OCPM F-DLS, we measure not only amplitude fluctuations but also phase changes of the particles by use of a low-coherence spectral interferometer. The use of low-coherence light minimizes the effect of multiple scattering in the measurement, and the phase stability due to the common-path configuration allows for obtaining reliable phase information. A complex valued interference signal at an optical path length of z in an SD-OCPM depth scan can be described as

$$\begin{aligned} F(t) &= E_R^* E_S(t) \\ &= E_R^* \exp(ik_s R)\sum_{j=1}^{N} E_j \exp\left[i\vec{q}\cdot\vec{r}_j(t)\right] \end{aligned} \tag{5.4}$$

where the reference electric field was assumed to be constant in time. Fluctuations caused by dynamic events in the scattering volume can be characterized by the temporal autocorrelation function of $F(t)$. We define the temporal auto-correlation function $R(\tau)$ as

$$R(\tau) = \frac{\left\langle F(t+\tau)F^*(t)\right\rangle}{\left\langle F(t)F^*(t)\right\rangle}. \tag{5.5}$$

Inserting Eqn. (5.4) into Eqn. (5.5) leads to

$$R(\tau) = \frac{\left\langle \left|E_R\right|^2 \sum_{j=1}^{N}\sum_{k=1}^{N} E_j E_k^* \exp\left[i\vec{q}\cdot\left(\vec{r}_j(t+\tau)-\vec{r}_k(t)\right)\right]\right\rangle}{\left\langle \left|E_R\right|^2 \sum_{j=1}^{N}\sum_{k=1}^{N} E_j E_k^* \exp\left[i\vec{q}\cdot\left(\vec{r}_j(t)-\vec{r}_k(t)\right)\right]\right\rangle}\ . \tag{5.6}$$

For the case of non-interacting (uncorrelated) particles, the cross terms $j \neq k$ vanish, to give

$$R(\tau) = \left\langle \exp\left[i\vec{q}\cdot\overrightarrow{\Delta r}(t)\right]\right\rangle \tag{5.7}$$

where $\overrightarrow{\Delta r}(t) \equiv \vec{r}(t+\tau) - \vec{r}(t)$. If it is assumed that each directional component in $\Delta\vec{r}(t)$, is a Gaussian random variable with mean and variance of $\mu_{\Delta l}(\tau)$ and $\sigma_{\Delta l}^2(\tau)$, $l = x, y, z$, respectively, Eqn. (5.7) becomes [8]

$$R(\tau) = \exp\left[-\frac{\left(q_x^2\sigma_{\Delta x}^2(\tau) + q_y^2\sigma_{\Delta y}^2(\tau) + q_z^2\sigma_{\Delta z}^2(\tau)\right)}{2} \right] \exp\left(i\vec{q} \cdot \overrightarrow{\mu_{\Delta r}}(\tau)\right). \tag{5.8}$$

Here, $\overrightarrow{\mu_{\Delta r}}(\tau)$ is defined by

$$\overrightarrow{\mu_{\Delta r}}(\tau) \equiv \left(\overrightarrow{\mu_{\Delta x}}(\tau), \overrightarrow{\mu_{\Delta y}}(\tau), \overrightarrow{\mu_{\Delta z}}(\tau)\right) \tag{5.9}$$

and represents the time-averaged mean displacement of the particles in the l direction in τ, whereas $\sigma_{\Delta l}^2(\tau)$ is the time-averaged displacement variance in the l direction in τ. The mean squared displacement, which is defined as $MSD_l(\tau) = \left\langle \left(l(t+\tau) - l(t)\right)^2 \right\rangle$, can then be evaluated by

$$MSD_l(\tau) = \sigma_{\Delta l}^2(\tau) + \mu_{\Delta l}^2(\tau). \tag{5.10}$$

For the case of standard Brownian motion, $\overrightarrow{\mu_{\Delta r}}(\tau) = (0, 0, 0)$ and $\sigma_{\Delta l}^2(\tau) = 2D_l\tau$, where D_l is the diffusion coefficient along the l direction [9]. Thus, our final form of Eqn. (5.8) for the pure Brownian motion in an isotropic medium (i.e., $D_x = D_y = D_z = D$) becomes

$$R(\tau) = \exp\left[-\frac{\tau}{\tau_D} \right] \tag{5.11}$$

where $\tau_D \equiv 1/Dq^2$ is the time constant for the decay of $R(\tau)$. Here, we assumed $q_x = q_y = q_z = q/\sqrt{3}$.

In conventional (intensity based) DLS measurements, one measures $|R(\tau)|^2$, so one cannot obtain the information about the mean displacement. However, in F-DLS measurement, examination of the phase of the auto-correlation function (Eqn. (5.8)) enables to measure the mean displacement of the particle motions.

5.2.2. Brownian motion measurement

In order to assess the utility of F-DLS, a sample that exhibits pure Brownian motion was first examined. Intralipid solution was prepared as a test sample, by diluting intravenous fat emulsion (Liposyn, Hospira, Inc.) in distilled water to obtain 1% concentration. The focus was positioned at ~ 10.4 μm above the top surface of a coverslip, and the interference signal between light reflected from focal volume and from the bottom surface of the coverslip was measured as a function of time. The acquisition rate and the integration time were 5 kHz and 100 μsec, respectively.

Figure 5.2 shows representative magnitude and phase curves of the complex auto-correlation function based on the intralipid solution measurement. The red line in Figure 5.2(a) represents the first-order exponential fit with a time constant of ~2.75 msec as determined by least square estimation. It can be seen that the magnitude curve fits well with the first-order exponential function, demonstrating Brownian dynamics of intralipid solution. Further confirmation can be made by referencing the phase of auto-correlation function (Fig. 5.2(b)). The phase, or time-averaged mean displacement of the particles, was found to be approximately zero within $0 \leq \tau < 10^{-2}$ sec, which is characteristic of random Brownian motion. In other words, the particles that exhibit Brownian motion have an equal probability to move in all directions, so the time-averaged displacement is zero.

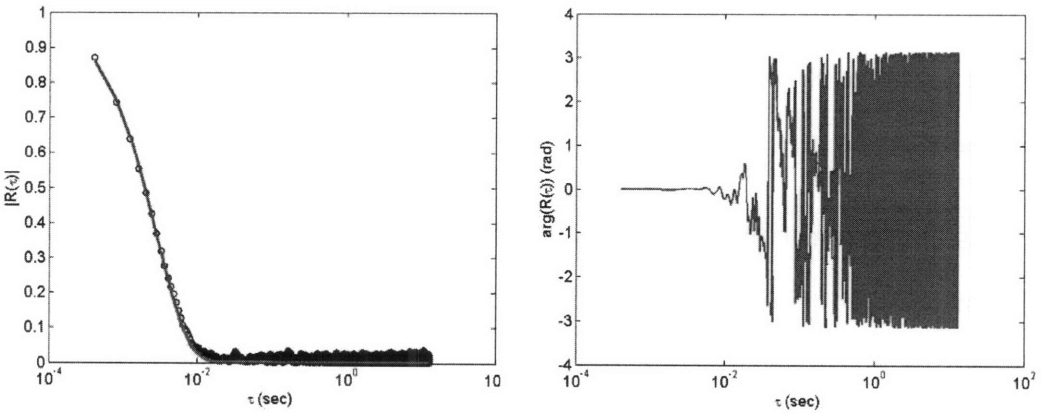

(a) (b)

Figure 5.2: Magnitude and phase plots for the complex autocorrelation function based on intralipid solution measurement. The red line in (a) shows the first-order exponential fit to the measurement, showing a pure Brownian dynamics of the sample. The time constant was obtained

as ~2.75 msec. The phase plot (b) shows that phase is approximately zero within the time constant, demonstrating no mean displacement, which is the characteristic of random Brownian motion.

We further confirmed Brownian dynamics of the intralipid solution by evaluating the mean squared displacement, $MSD(\tau)$. By use of Eqn. (5.8) and (5.10), $MSD(\tau)$ can be calculated by

$$MSD(\tau) = \frac{-\ln\left(R(\tau)R^*(\tau)\right)}{q^2} + \frac{\tan^{-1}\left(R(\tau)\right)}{q} \tag{5.12}$$

where $q = 2k_0$ was used to take into account the back-scattering configuration. Figure 5.3 shows the calculated MSD along the fit, found by the least square estimation using the power-law relation, $D\tau^{\alpha}$. As can be noted, the exponent was close to 1, which proves that the intralipid solution exhibits Brownian dynamics.

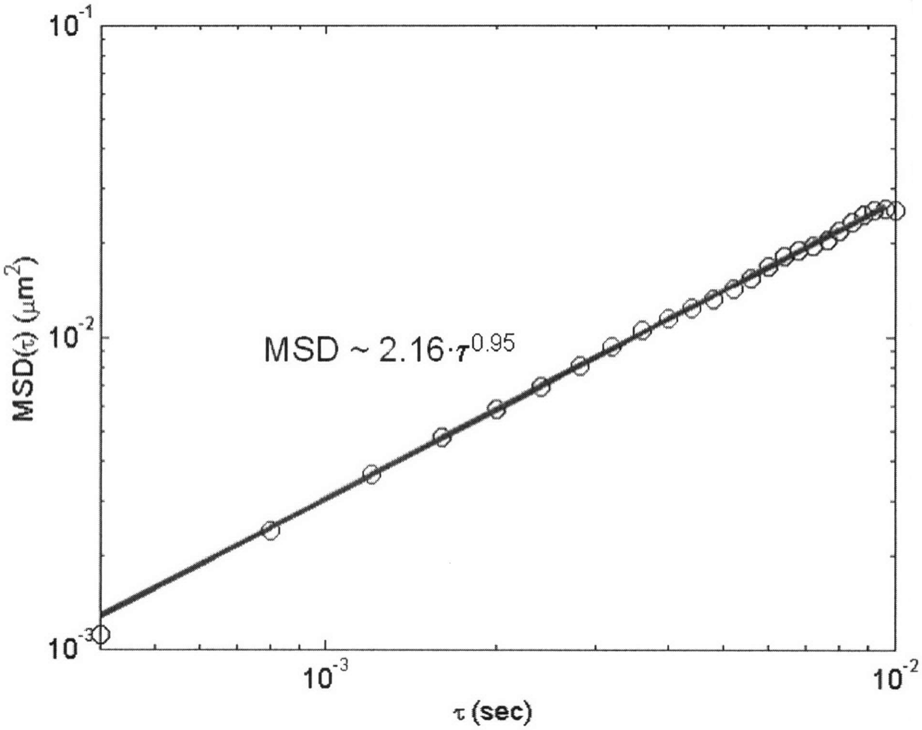

Figure 5.3: Calculated mean squared displacement along with the fit determined by the least square estimation. The power-law, $D\tau^{\alpha}$, was used for the fit. The exponent was found as 0.95, which demonstrates Brownian dynamics of the intralipid solution.

5.2.3. Intracellular dynamics

Unlike the colloidal suspensions in which the main source of fluctuations is thermal energy defined by $k_B T$, extra- and intracellular motions are influenced by the combination of a non-Newtonian cytoplasmic environment and motions of subcellular structures regulated by thermal energy and ATP-hydrolysis. The investigation of the property of intracellular dynamics by use of the F-DLS technique is the scope of this Section.

Material

Human ovarian cancer cells (OVCAR-3) provided by Drs. Thomas Stepinac and Tayyaba Hasan (Harvard Medical School, MA) were used for this study. OVCAR-3 cells were plated in 35 mm collagen-coated coverslip base dishes (MatTek Corporation, Ashland, MA) at a density of $8\text{-}10\times10^4$ cells/dish and cultured in DMEM containing 10% fetal calf serum (FCS) at 37°C in a humid 5% CO_2 atmosphere. After incubation for 24 hours, the cells were measured.

Methods

Approximately 61 measurements over 15 OVCAR-3 cells were performed. Two-dimensional cellular images were first examined to identify the cytoplasmic region. Once the region of interest was located, the focus was positioned at a desired location in a three-dimensional space by means of XY galvanometer scanners and a PZT transducer. In this study, the focus was positioned at ~3.4 μm above the top surface of a coverslip. The sampling rate was 5 kHz, and the integration time was ~190 μsec. The total acquisition time was ~26 seconds, generating 130,560 data points in each measurement.

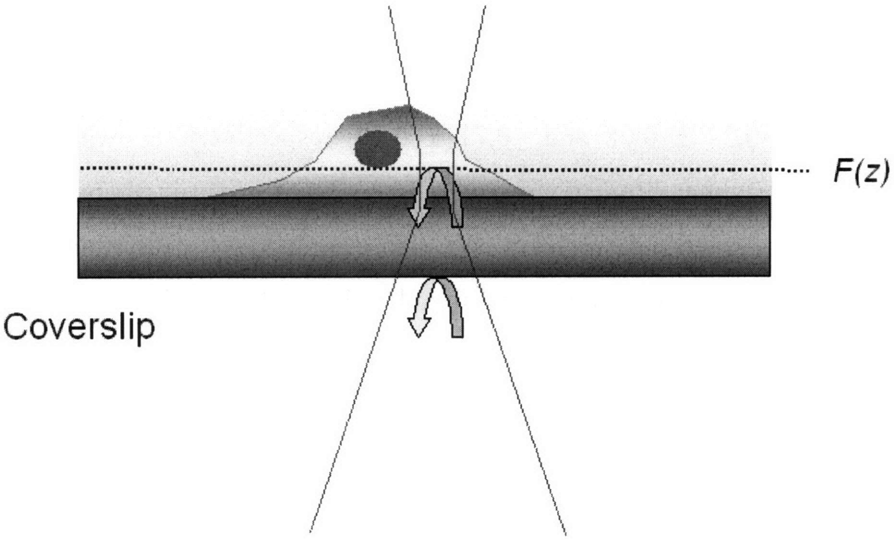

Figure 5.4: SD-OCPM F-DLS measurement for intracellular dynamics. The focus is located at ~3.4 μm above the top surface of the coverslip, and complex interference signal in focus is examined as a function of time.

Results and Discussion

Figure 5.5 shows a representative example of the magnitude of the temporal auto-correlation function, the time-averaged displacement, and MSD obtained from an OVCAR-3 cell. The time-averaged displacement was obtained by taking the argument of complex correlation function and by dividing it by q, and the MSD was calculated by use of Eqn. (5.12). The red and green lines in Figure 5.5(c) represents the power-law fits determined by the least square estimation. The magnitude plot (Fig. 5.5(a)) did not fit well with the first-order exponential function, demonstrating anomalous diffusion characteristic of intracellular dynamics. The examination of the time-averaged displacement and MSD plots reveals that there exist two distinct regimes of diffusion. At short times ($\tau < 0.1$ sec), the mean displacement was in the range of 0.3 nm, and the exponent in the power-law fit was ~0.32. However, the mean displacement changed markedly, and the exponent increased to 0.79 at longer times ($\tau \geq 1$ sec).

We also examined the dynamics of other measurements, and the results are summarized in Figure 5.6. In all 61 measurements, we observed the existence of two different regimes in diffusion characteristics, even though the exponents varied depending on location and time of measurement. The average exponents in short and long timescales were ~0.27 ± 0.08 and ~0.71 ± 0.20, respectively, showing the obvious difference in two regimes. Remarkably, we observed superdiffusive behavior ($\alpha > 1$) at long time scales in some measurement. We also examined the distribution of diffusion coefficients at two different regimes, and found a change by ~10 %, while the exponent increased by a factor of 3.

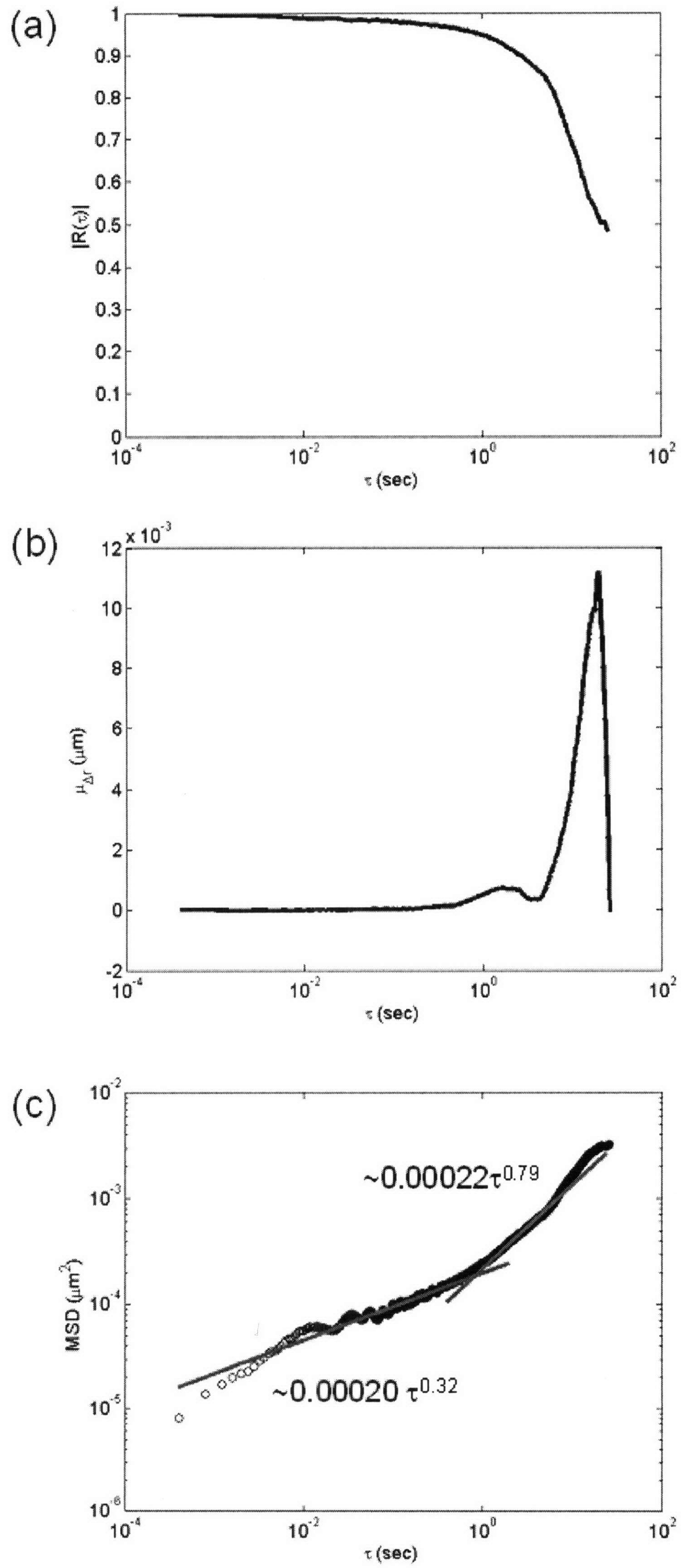
(a)
|R(τ)|
1
0.9
0.8
0.7
0.6
0.5
0.4
0.3
0.2
0.1
0
10^-4
10^-2
10^0
10^2
τ (sec)
(b)
x 10^-3
μ_Δr (μm)
12
10
8
6
4
2
0
-2
10^-4
10^-2
10^0
10^2
τ (sec)
(c)
MSD (μm^2)
10^-2
10^-3
10^-4
10^-5
10^-6
~0.00022τ^0.79
~0.00020 τ^0.32
10^-4
10^-2
10^0
10^2
τ (sec)

Figure 5.5: Representative dynamics of an OVCAR-3 cell. (a) Magnitude for the complex autocorrelation function, (b) the time-averaged mean position, and (C) the calculated MSD from the correlation function. The red and green lines in (c) represent the power-law fits found by least square estimation. It shows the existence of two difference regimes in time-scaling, and demonstrates that the cell exhibits the transition from low to high diffusive regimes around 0.1 ~ 1 second, at which the mean position curve (b) also shows a remarkable change.

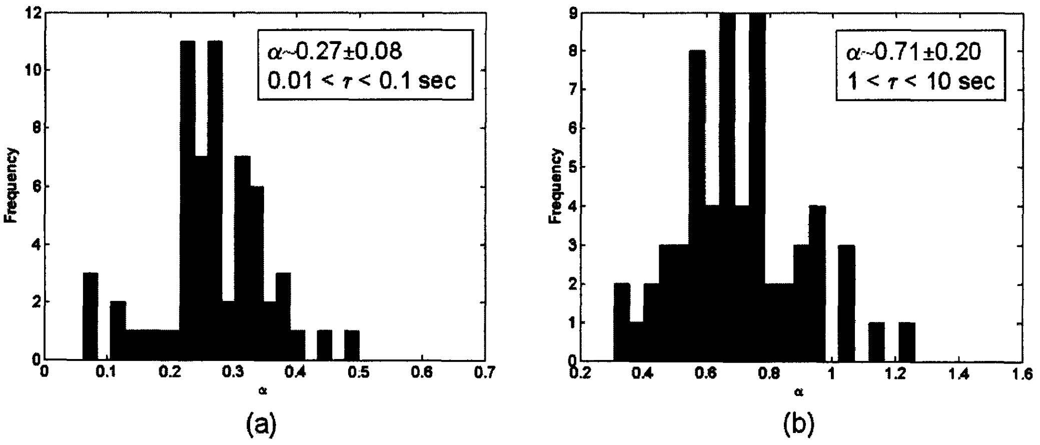

Figure 5.6: The histograms of the exponents in two different diffusive regimes. The exponents were estimated by a least-square fit of a power law to the MSD data. (a) The exponent distribution at short times ($\tau < 0.1\,\text{sec}$); (b) The exponent distribution at short times ($1 < \tau < 10\,\text{sec}$). The mean exponents were estimated as 0.27 and 0.71, respectively.

Bursac *et. al.* reported the existence of an intermittent metastate and the transition from the subdiffusive to superdiffusive regime in cytoskeletal dynamics [10]. They measured the track of microspheres inside the human airway smooth muscle cell, and noted that the spontaneous bead motions were subdiffusive at short times but superdiffusive at longer times. Remarkably, the time scale of the transition is consistent with our result. The transition reflects nanoscale cytoskeleton rearrangements, and depends on ATP hydrolysis. A physical picture capturing these dynamics uses an energy landscape to describe all possible microconfigurations of the cytoskeleton. Thermal energy is typically insufficient to push the system over the energy barriers into different microconfigurations; this is analogous to a jammed state. Through intermittent transitions from one metastate to another, the system evolves slowly into more stable microconfigurations. For cells, ATP-dependent rearrangements of the cytoskeletons modify the microconfigurations themselves, providing a means of exploring new configurations; ATP-hydrolysis can drive both protein conformational changes and polymerization/depolymerization cycles, either of which could conceivably resolve the constraints and drive structural rearrangements.

Though the time scale of the transition between two different diffusive regimes agrees with our measurement ($0.1 < \tau < 1$ sec), there is a discrepancy in that we measured the transition from subdiffusive ($\alpha < 0.5$) to another subdiffusive regimes ($\alpha > 0.5$), while Bursac *et. al.* reported a subdiffusive ($\alpha < 1$) to superdiffusive transition ($\alpha > 1$). The measurements by Bursac *et. al.* were confirmed by others, using the same approach, the particle tracking [11].

We hypothesize the reason for this difference to be as follows. In a particle tracking method, it tracks and measures the displacement of a single particle, which is embedded in a cytoplasmic environment. Therefore, it would reflect the rearrangement of cytoskeleton by a fast motion of the particles at the transition between two different diffusive regimes. In our case, however, the measurement is based on light scattered from, in principle, many scatterers inside the focal volume. While some portions of the structures such as vesicles may travel around just like microspheres, the other structures such as cytoskeletal structures stay and displaces within the focal volume. If that is the case, each structure inside the focal volume would have different dynamic behavior (subdiffusive or superdiffusive) and contribute differently to the measurement results. This compounding effect would be the quantity of our measurement.

5.2.4. Effect of Colchicine on OVCAR-3 intracellular dynamics

We further investigated the change in intracellular dynamics caused by the introduction of cellular agents. The motivation of this work is to appreciate the contributions of vesicle trafficking along the microtubules to our experimental results as well as to investigate the change in cellular processes due to internalization of drugs, which is critical toward the design of therapeutic agents.

We hypothesize that the observed intracellular dynamics in OVCAR-3 cells is in part due to the microtubule-based vesicle transport. In order to validate our hypothesis, we employed an anti-cancer drug, *Colchicine*.

Colchicine is a highly poisonous alkaloid, originally extracted from plants of the genus Colchicum. Originally used to treat rheumatic complaints and especially gout, it is being investigated for its potential use as an anti-cancer drug. Colchicine inhibits microtubule polymerization by binding to tubulin, one of the main constituents of microtubules. Therefore, we hypothesize that the introduction of Colchicine to OVCAR-3 cell lines would modify the characteristics of intracellular dynamics because of the inhibition of polymerization of microtubules along which vesicles travel. Ref. [12] studied the efficacy of Colchicine to glial cells, and reported that while it is effective to disrupt all microtubules, it has no effect on actin filament dynamics [12]. To insure that we observe dynamics related to microtubule-related transport, the optical focus was positioned in the middle of the cell in this measurement.

Materials and Method

The cell lines and methods are identical to those described in the previous section, except that the cells are treated with Colchicine. After 24-hour incubation after plating, cells were incubated in a 25 μM Colchicine-mixed medium for 3 hours prior to measurement.

Results and Discussion

We made ~58 F-DLS measurements over 15 Colchicine-treated cells. Representative magnitude of the temporal auto-correlation function, the time-averaged displacement, and MSD are presented in Figure 5.7. Colchicine-treated cells also exhibited anomalous diffusion characteristics, and most measurements showed the existence of two different diffusive regimes, as in the control cells. However, we noticed that the exponent decreased compared to the control cells.

In order to perform quantitative and statistical comparison in cellular dynamics between control and Colchicine-treated cells, we extracted the exponents from each measurement at short $(0.01 < \tau < 0.1 \text{ sec})$ and long times $(1 < \tau < 10 \text{ sec})$, and generated histograms. Figure 5.8 shows the histograms for the exponents for the control and Colchicine-treated cells at short and long timescales. At the short timescales, we found the change of mean exponent from 0.27 to 0.30, but observed that the exponent at the long timescales decreased by 20 % by the introduction of Colchicine. We also run the student *t*-test on the exponent distributions for the long timescales, and found that their mean values are statistically different, $p << 0.05$.

Our results are consistent with the observation in the literatures. The reduction of the exponent has been observed by the inhibition of cytoskeleton polymerization [13]. According to Fabry *et. al.* [11], the theory of soft glassy materials predicts that a phase change occurs as the power-law exponent describing the correlation time dependence of the elastic and viscous properties of the cell moves between 1 and 0. Here, an exponent of 1 describes entirely fluid-like behavior, whereas an exponent of 0 represents entirely solid-like behavior. If soft glassy materials are an appropriate model for the cell, our observation that the exponent decreased by ~20 % leads to the conclusion that Colchicine moves the cell towards a solid-like status.

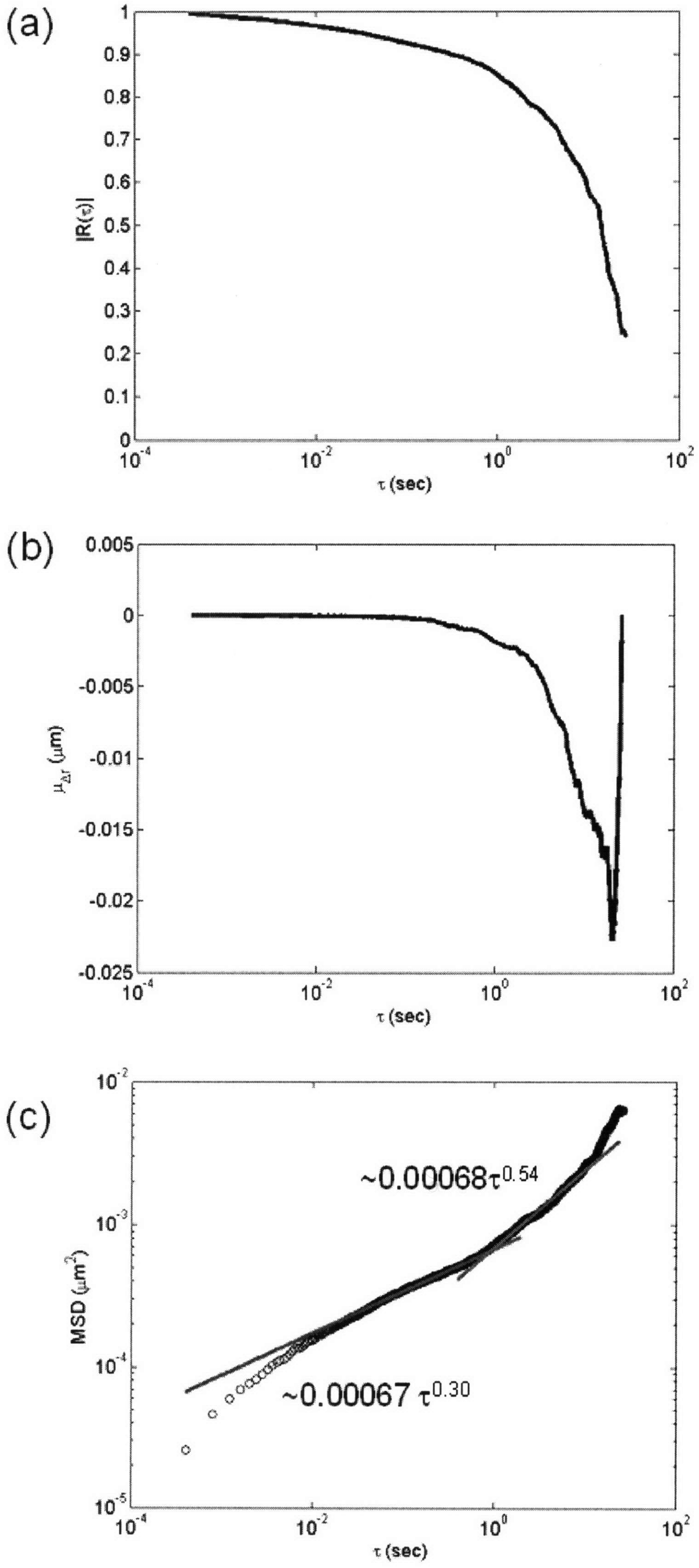
(a)
1
0.9
0.8
0.7
0.6
0.5
0.4
0.3
0.2
0.1
0
|R(τ)|
10^{-4}
10^{-2}
10^{0}
10^{2}
τ (sec)
(b)
0.005
0
-0.005
-0.01
-0.015
-0.02
-0.025
$\mu_{\Delta r}$ (μm)
10^{-4}
10^{-2}
10^{0}
10^{2}
τ (sec)
(c)
10^{-2}
10^{-3}
10^{-4}
10^{-5}
MSD (μm^2)
~0.00068τ$^{0.54}$
~0.00067 τ$^{0.30}$
10^{-4}
10^{-2}
10^{0}
10^{2}
τ (sec)

Figure 5.7: Representative dynamics of a Colchicine-treated OVCAR-3 cell. (a) Magnitude for the complex autocorrelation function, (b) the time-averaged displacement, and (C) the calculated MSD from the correlation function. The red and green lines in (c) represent the power-law fits found by least square estimation. It shows the existence of two difference regimes in time-scaling, and demonstrates that the cell exhibits the transition from low to high diffusive regimes around 0.1 ~ 1 second, at which the mean displacement curve (b) also shows a remarkable change.

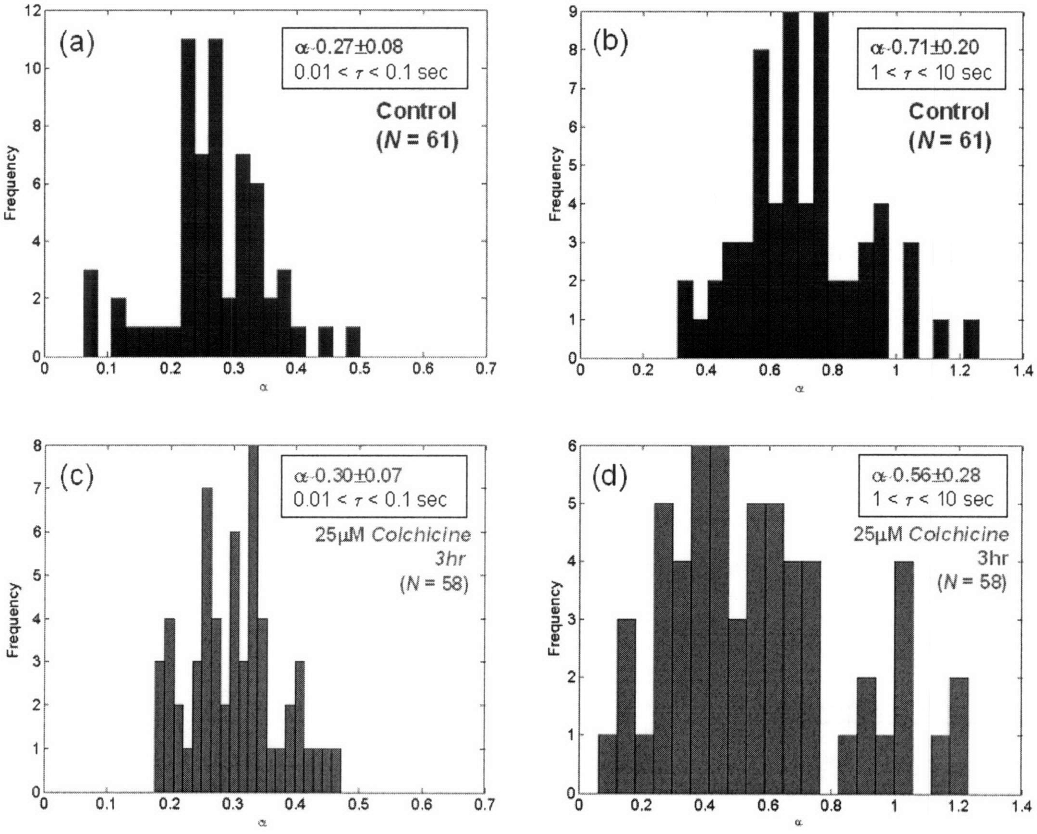

Figure 5.8: Histograms of α determined from ~61 measurements of ~15 control ovarian cancer cells (Sec. 5.2.2) and ~58 measurements of ~15 Colchicine-treated cells. (a) and (b) represent the histograms of α for control cells at short and long timescales, and (c) and (d) are the corresponding histograms for Colchicine-treated cells. Compared to the control cells, the exponent decreased by ~20 % at long timescales, demonstrating the decrease in intracellular dynamics due to the inhibition of microtubule polymerization.

5.2.5. Effect of ATP depletion on OVCAR-3 intracellular dynamics

If the transition in intracellular dynamics is caused by ATP dependent cytoskeletal rearrangements and organelle transport at long times, it is expected to observe decrease in intracellular dynamics at the long timescales for ATP-depleted cells, whereas no significant change is observed at short timescales. In order to confirm the validity of our measurement as well as ATP-induced dynamics at long timescales, we conducted F-DLS measurements on ATP-depleted OVCAR-3s.

Materials and Method

The ovarian cancer cells were ATP-depleted, following the protocols described in Ref. [10]. After 24-hour incubation, the cells were treated by 2 mM deoxyglucose and 2 mM sodium azide (NaN_3) to deplete ATP.

Results and Discussion

We made ~67 measurements over 10 cells, and the results are summarized in Figure 5.9. Figure 5.9(a) and (b) are the replica of the results for the control cells (Figure 5.6), and Fig. 5.9(c) and (d) are the histograms for the ATP-depleted cells at the two different timescales. It can be noted that the exponent at the short timescales showed only ~7% difference compared to the control cells, but the exponent at long timescales (which is thought to be ATP-dependent) showed ~40 % decrease. The student *t*-test showed that there is a correlation in terms of the exponent for short timescales, but the mean values of the exponents for the control and ATP-depleted cells at long timescales are significantly different in statistical sense, exhibiting, $p << 0.05$.

We still could observe the transition between two different diffusive regimes for the ATP-depleted cells. This may be explained by that ATP concentration was still found as 2~7% of that in control samples as reported in Ref. [10].

Overall, the results presented in this section demonstrates that the intracellular dynamics at long timescales is ATP-dependent, and F-DLS allows us to directly measure the change in intracellular dynamics.

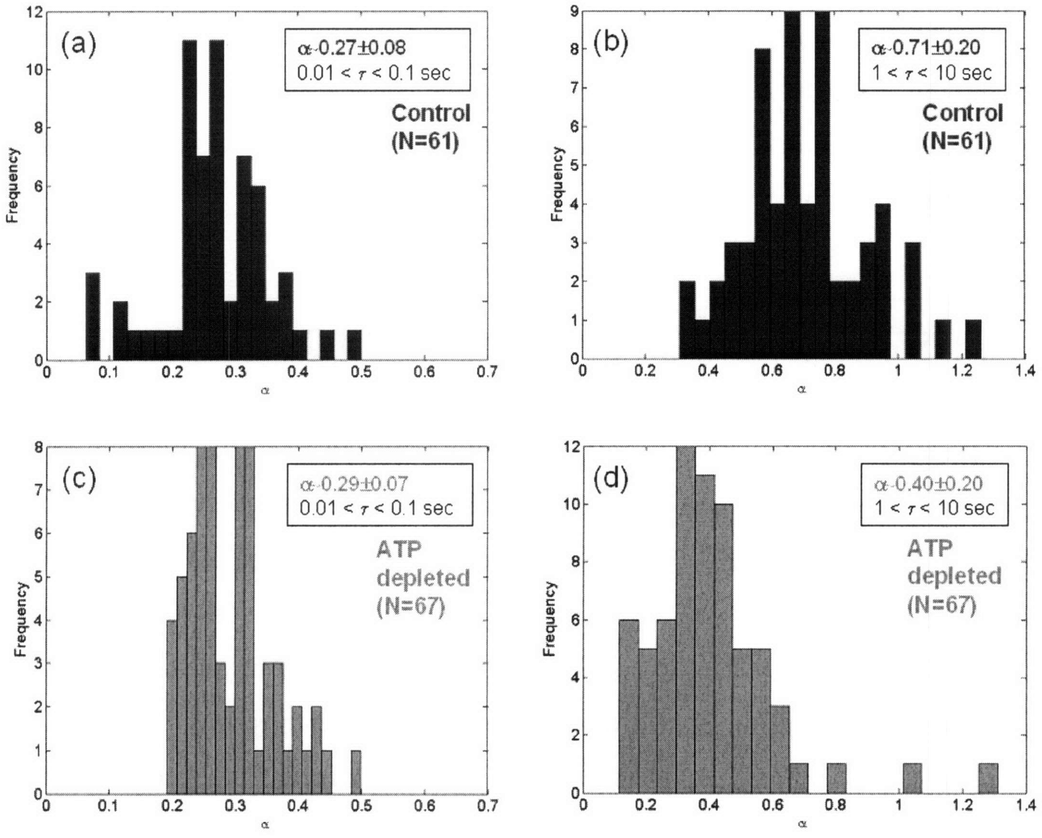

Figure 5.9: Histograms of α determined from ~61 measurements of ~15 control ovarian cancer cells (Sec. 5.2.2) and ~67 measurements of ~10 ATP-depleted cells. (a) and (b) represent the histograms of α for control cells at short and long timescales, and (c) and (d) are the corresponding histograms for ATP-depleted cells. Compared to the control cells, the exponent decreased by ~40 % at long timescales, demonstrating the decrease in intracellular dynamics due to ATP-depletion.

5.3. SD-OCPM for slow cellular dynamics

In this section, an application of SD-OCPM imaging to investigate slow dynamics of cellular specimens is described. The previous method provides localized measurement of intracellular dynamics with high spatial and temporal resolution, but does not offer an overview on cellular dynamics over the whole sample space. Here, we present quantitative information of cellular dynamics over the whole sample space by exploiting the imaging capability of SD-OCPM.

5.3.1. Slow dynamics of top surface of OVCAR-3

Based on the optical sectioning capability of SD-OCPM, the structural variation around the top surface of a single ovarian cancer cell was examined by taking the images with the focus positioned at ~10 μm above the coverslip. To generate images, the focal volume was raster-scanned over the specimen while acquiring the interference spectrum. Based on the refractive index of the medium (~1.35) and the physical position of the focal volume, the points of interest were identified in the depth-resolved A-line intensity profile, and their amplitude and phase information were extracted to generate the images.

The image acquisition speed per frame was typically ~13 seconds with an image size of 256×256 (A-line rate: 5 kHz for sustained data transfer), and the total time for the image acquisition of 100 frames was ~ 22 minutes.

For measurement, the amplitude and phase information at 8 μm and 10 μm above the coverslip was examined. Figure 5.10 shows representative time-lapsed images acquired by SD-OCPM. The images (a), (b), and (c) are the intensity, phase, and phase gradient images, respectively. Adding the intensity information at two depth locations generated the intensity image, whereas the phase image was constructed by taking the difference between the two unwrapped phase images. The image (c) was obtained as described in Chapter 2, i.e., by taking gradient of phase image (b) and adding two vectors. Note that only the top portion of the cell structures is observed because of the sectioning capability of SD-OCPM by means of confocal and coherence gatings. The intensity image provides rather qualitative reflectivity information of the top portion of the cell, but the phase image reveals distinct features through phase distribution, which are not obvious in the intensity image. Based on the significant optical phase delay at the center compared to the other cellular region, it is believed that the structure in blue represents the nucleus.

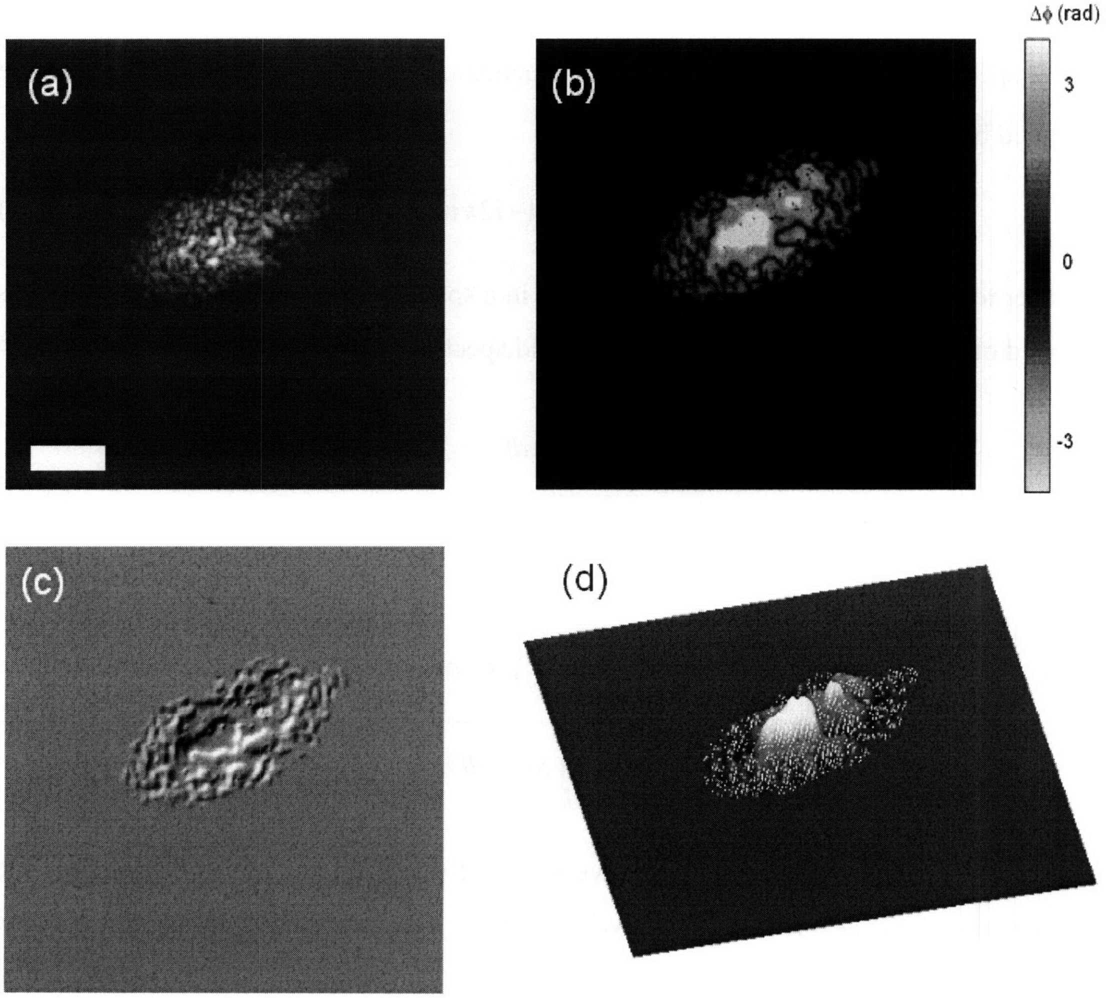

Figure. 5.10: SD-OCPM images of the top surface of a live OVCAR cell. The image processing method is described in text. (a) Intensity; (b) phase, along with the phase distribution in radians; (c) phase gradient image; (d) 3D surface map based on the phase information (b). The intensity image shows rather qualitative information about the strength of the back-reflected beams, while the distinctive phase changes across the specimen are shown in the phase image. Based on the significant optical phase delay, the structure at the center is thought to be the nucleus. The scalebar in (a) denotes 10 μm.

Using the time-lapsed quantitative phase images, spectral analysis was performed to examine the low-frequency dynamics related to the vicinity of cell membrane. The spatially resolved temporal autocorrelation function is defined as

$$R(x,y;\tau)=\int\phi(x,y;t)\phi(x,y;t+\tau)dt, \tag{5.13}$$

where $\phi(x,y;t)$ denotes the phase information at a position, (x,y) and time t. Thus, the power spectrum function $S(f)$ of the phase fluctuations in each point of the image can be obtained by

$$S(f)=\int R(x,y;\tau)\exp(-i2\pi\tau)d\tau. \tag{5.14}$$

In order to characterize the phase fluctuations in a spatially resolved manner, the cell was mapped out in terms of the mean frequency and spectral variance as:

$$f_0=\frac{\int_0^{f_{\max}} f\,S(f)\,df}{\int_0^{f_{\max}} S(f)\,df} \tag{5.15}$$

$$\sigma_f^2=\frac{\int_0^{f_{\max}} (f-f_0)^2\,S(f)\,df}{\int_0^{f_{\max}} S(f)\,df}\quad. \tag{5.16}$$

The mean frequency is the representative speed of phase fluctuation in each point, and the spectral variance provides the diversity of the frequency contents centered at the mean frequency. The phase variance image was also generated to show the magnitude of phase fluctuations. The images shown in Figure 5.11 (a), (b), and (c) are the mean frequency, spectral variance, and phase variance images, respectively. Notice that the perimeter region of the nucleus exhibits fast and broad dynamics compared to the other cellular regions based on the mean frequency and spectral variance images (a) and (b). On the other hand, the magnitude of phase fluctuations is more significant in the nucleus region as shown in the phase variance image (c) because the phase change in the nucleus is higher than in the other cellular structures.

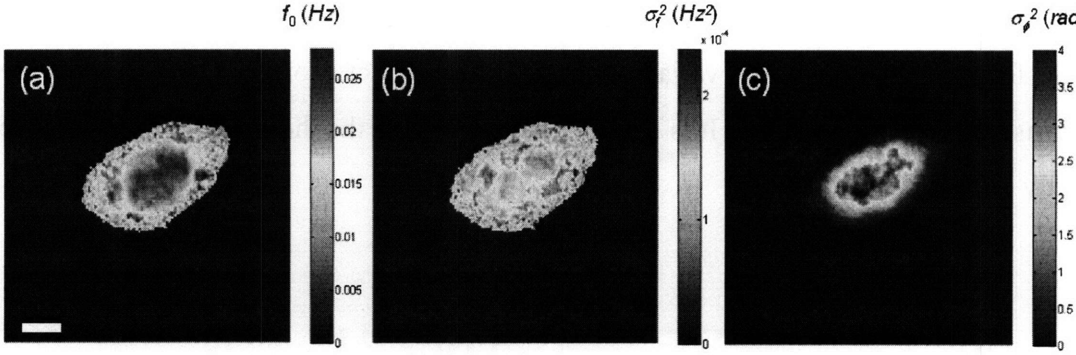

Figure. 5.11: Calculated mean frequency (a), spectral variance (b), and phase variance (c) images based on the time-lapsed quantitative phase images of the top surface of the ovarian cancer cell. The images were masked to remove the noise in the background. It can be noted that the perimeter regions of the nucleus exhibit fast and broad dynamics compared to the nucleus. The magnitude of the phase change, on the other hand, is more significant in the nucleus as can be seen in phase variance map (c).

5.3.2. Slow dynamics of OVCAR-3s at different physiological conditions

We further employed SD-OCPM to examine the slow intracellular dynamics in different physiological conditions. OVCAR-3 cells at different temperatures, 37 °C and 25 °C were used for this measurement. The focus was positioned at ~4.2 μm above the top surface of the coverslip, and the complex-valued information related to two depth locations in focus were used to generate the mean frequency, spectral variance, and phase variance images. In Figure 5.12, the images (a), (b), and (c) represent the mean frequency, spectral variance, and phase variance images for 37 °C respectively, and the images (d), (e), and (f) are the corresponding images for 25 °C. The comparison of the images for mean frequency and spectral variance shows reduced activity at 25 °C compared to 37 °C. In this case, the scattering from the nucleus was weak, which may be due to the fact that the focus is in the middle of the nucleus. The mean frequency and spectral variance averaged over the cell region were obtained as ~3.9 mHz and ~72.2 μHz for 37 °C, and ~1.3 mHz and ~25.6 μHz for 25 °C, respectively. Interestingly, the mean frequency and spectral variance decreased by a factor of ~3 for a temperature decrease from 37 °C to 25 °C. It is remarkable, noting that the thermal energy difference is only ~3 %.

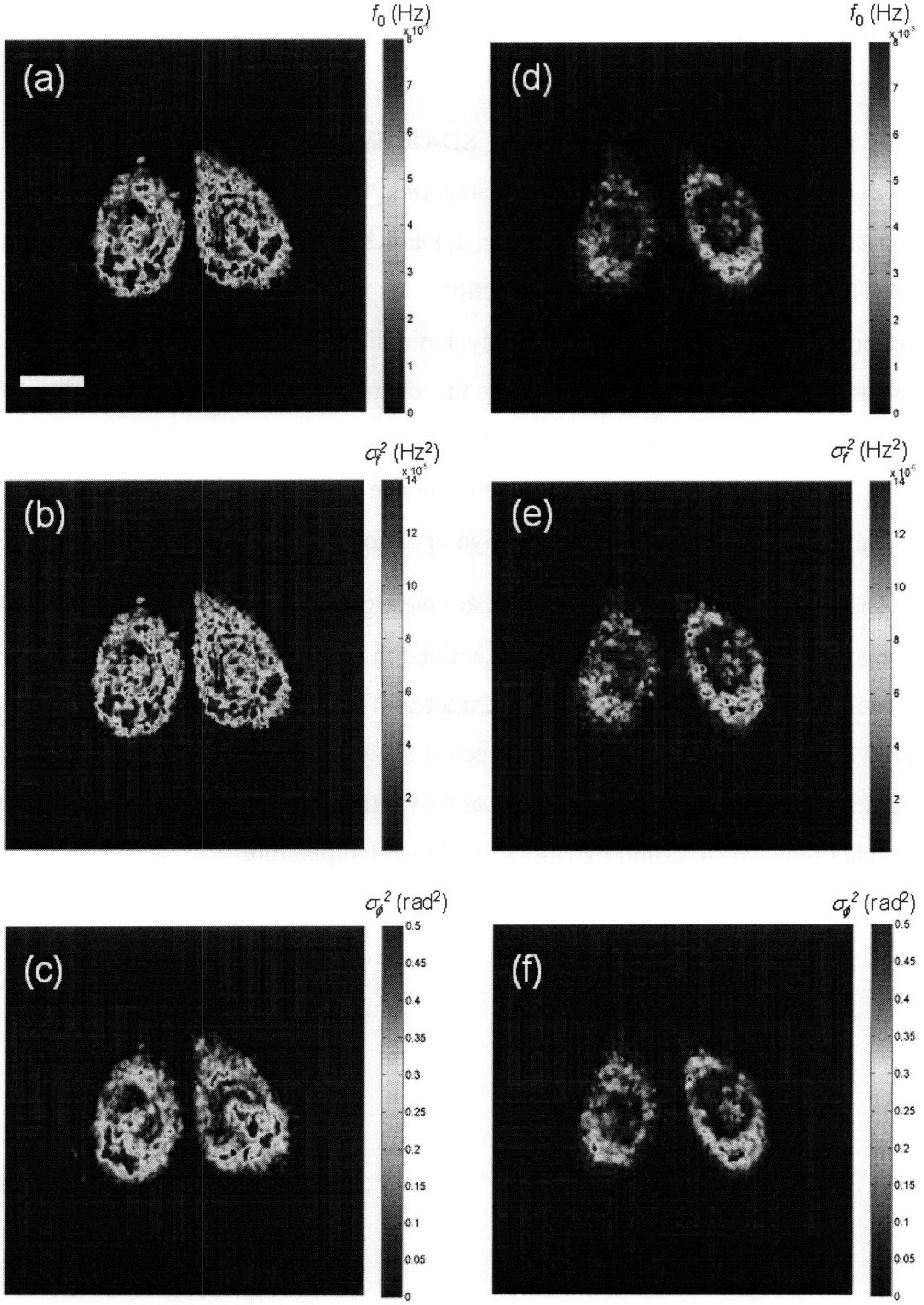

Figure. 5.12: Calculated mean frequency (a,c), spectral variance (b,d), and phase variance (c,e) images for 37 °C and 25 °C. The reduced activity can be observed for 25 °C compared to that for 37 °C based on the mean frequency and spectral variance images. There was no significant difference in terms of the magnitude of phase fluctuations. The scalebar represents 10 μm.

5.4. Summary

In this Chapter, the capability of SD-OCPM for quantitative investigation of cellular dynamics was described in two categories: localized measurement of diffusive characteristics associated with intracellular dynamics, and an imaging method for slow (or low frequency) dynamics investigation. As for localized diffusion property measurement, we proposed field-based dynamic light scattering by SD-OCPM, and demonstrated its feasibility for measuring the diffusion characteristics of a Brownian sample and cellular specimens. We observed the existence of two different regimes in intracellular dynamics in living cells, and the change in intracellular activity when ATP-depleted and treated with a microtubule polymerization inhibitor, Colchicine.

The slow cellular dynamics were also investigated in conjunction with the optical sectioning capability of SD-OCPM. We examined the dynamics in the vicinity of the top membrane of cells, and found that the perimeter of the nucleus exhibited fast motions compared to the other regions by use of spectral analysis. By placing the focal volume in the middle of the cells, cellular dynamics at two different temperatures were examined; that revealed reduced structural dynamics at a lower temperature.

5.5. Reference

1. R.L. Margolis and L. Wilson, "*Addition of colchicine-tubulin complex to microtubule ends: The mechanism of substoichiometric colchicine poisoning,*" Proceedings of National Academy of Sciences. **74,** 3466-3470 (1977).

2. R.P. Kulkarni, D.D. Wu, M.E. Davis, and S.E. Fraser, "*Quantitating intracellular transport of polyplexes by spatio-temporal correlation spectroscopy,*" Proceedings of National Academy of Sciences. **102,** 7523-7528 (2005).

3. R.P. Kulkarni, K. Castelino, A. Majumdar, and S.E. Fraser, "*Intracelluar transport dynamics of endosomes containing DNA polyplexes along the microtubule network,*" Biophysical Journal. **90,** L42-44L (2006).

4. F. Vazquez, S. Matsuoka, W.R. Sellers, T. Yanagida, M. Ueda, and P.N. Devreotes, "*Tumor suppressor PTEN acts through dynamic interaction with the plasma membrane,*" Proceedings of National Academy of Sciences. **103,** 3633-3638 (2006).

5. P.J. Berne and R. Pecora, *Dynamic Light Scattering*. 1976, New York: Wiley.

6. D.A. Boas, K.K. Bizheva, and A.M. Siegel, "*Using dynamic low-coherence interferometry to image Brownian motion within highly scattering media,*" Optics Letters. **23,** 319-321 (1998).

7. W. Brown, *Dynamic Light Scattering: The Method and Some Applications*. 1993, Oxford: Clarendon Press.

8. J.W. Goodman, *Statistical Optics*. 1985, New York: John Wiley & Sons, Inc.

9. H.C. Berg, *Random Walks in Biology*. 1993, New Jersey: Princeton University Press.

10. P. Bursac, G. Lenormand, B. Fabry, M. Oliver, D.A. Weitz, V. Viasnoff, J.P. Butler, and J.J. Fredberg, "*Cytoskeletal remodeling and slow dynamics in the living cell,*" Nature Materials. **4,** 557-561 (2005).

11. B. Fabry, G.N. Maksym, J.P. Butler, M. Glogauer, D. Navajas, and J.J. Fredberg, "*Scaling the microrheology of living cells,*" Physical Review Letters. **8714,** 148102 (2001).

12. B.S. Spooner, K.M. Yamada, and N.K. Wessells, "*Microfilaments and cell locomotion,*" Journal of Cell Biology. **49,** 595-613 (1971).

13. E.J. McDowell, A.K. Ellerbee, M.A. Choma, B.E. Applegate, and J.A. Izatt, "*Spectral-domain phase microscopy for local measurements of cytoskeletal rheology in single cells,*" Journal of Biomedical Optics. **12,** 044008 (2007).

14. P. Bursac, B. Fabry, X. Trepat, G. Lenormand, J.P. Butler, N. Wang, J.J. Fredberg, and S.S. An, "*Cytoskeleton dynamics: Fluctuations within the network,*" Biochemical and Biophysical Research Communications. **355,** 324-330 (2007).

Chapter 6:
SD-OCPM for highly sensitive molecular recognition

6.1. Introduction

In this Chapter, SD-OCPM is presented as a highly sensitive optical sensor for molecular interaction. Owing to its high sensitivity to phase (or optical thickness) variation of a surface in a sample, SD-OCPM is able to detect minute phase change at a sensor surface caused by molecular absorption and desorption. More importantly, its intrinsic imaging capability allows for monitoring multitude of activated sites on the sensor surface with high spatial and temporal resolution. Basic operation of SD-OCPM as molecular sensor is described, and the experimental results conducted to explore its potential as a biosensor are presented.

6.2. Background

Real-time detection of minute traces of molecules (e.g., pesticides, viruses, and organic toxins) on activated sensor surfaces is of great importance in many applications such as medical diagnostics, disease screening, and environmental monitoring. For instance, medicine has a need for highly sensitive detection method for viruses, and early detection of chemicals and pathogens (e.g., anthrax) that could trigger corrective action is very important in a broad range of environmental applications and bio-defense.

Such detection has often been conducted by fluorescent methods [1]. Though these label-based techniques could potentially achieve single molecular level detection, they require additional specimen preparation, which is time-consuming and may affect molecular structures or interaction properties. Label-free methods detect physical absorption of molecules on a sensor surface. Surface plasmon resonance (SPR) [2] and resonant microcavity [3] sensors exploit the change of the resonant SPR angle and the optical frequency due to the alteration of the refractive index at the sensor surface upon molecular absorption, respectively.

Optical interferometric methods for molecular recognition have been extensively sought since they enable label-free detection with high speed and sensitivity. Those techniques include porous silicon-based interferometry [4], reflectometric interference spectroscopy [5], integrated Young's interferometry [6], and the optical biological compact disk (BioCD) [7, 8].

We describe a novel application of SD-OCPM to highly detection of molecular interaction. Based on a low-coherence interferometer, SD-OCPM sensor allows the identification of the sensor surface of interest by means of coherence gating, and confines the reflection signal from the sensor surface to within the coherence length of the source. The signal related to the surface is thus not influenced by the reflection from other surfaces, but detects the optical thickness change due to molecular absorption or desorption at that surface. The sensing region for the SD-OCR sensor can be as small as the size of a diffraction-limited beam spot, enabling detection with significantly reduced amount of probe molecules. We demonstrate the sensitivity of SD-OCR sensor by measuring the optical thickness change of SiO_2 layer as it is etched by diluted hydrofluoric acid solution, and present its utility as a biosensor by monitoring biotin-streptavidin binding in a microfluidic channel.

Using its imaging capability, we also explore the potential of SD-OCPM as multiplexed molecular array scanner. A SiO_2 etch pattern as a model sensor surface is first imaged to assess its sensitivity, followed by the imaging of protein arrays on SiO_2 substrate.

6.3. Method

The experimental implementation of SD-OCPM for molecule sensing is identical to that for cellular imaging, except that the specimen is replaced by a molecule-activated sensor surface or fluidic device (Figure 1). For typical operation, the probe beam is focused on the activated sensor surface via a microscope objective (Carl Zeiss, 5×/0.13) with a measured lateral resolution of ~2.5 μm in FWHM, and the depth-resolved information is obtained by taking an inverse Fourier transform of the interference spectrum measured at the spectrometer. The intensity map is used to locate a specific complex coherence function related to the molecule-coupled sensor surface, and the phase (or optical thickness) of that signal is monitored to examine molecular absorption. The other interference signals denoted by "2-3" and "1-3" in Figure 6.1 are not selected, because their phase information is also influenced by the reflection from other surfaces and the change in the refractive index of the solution.

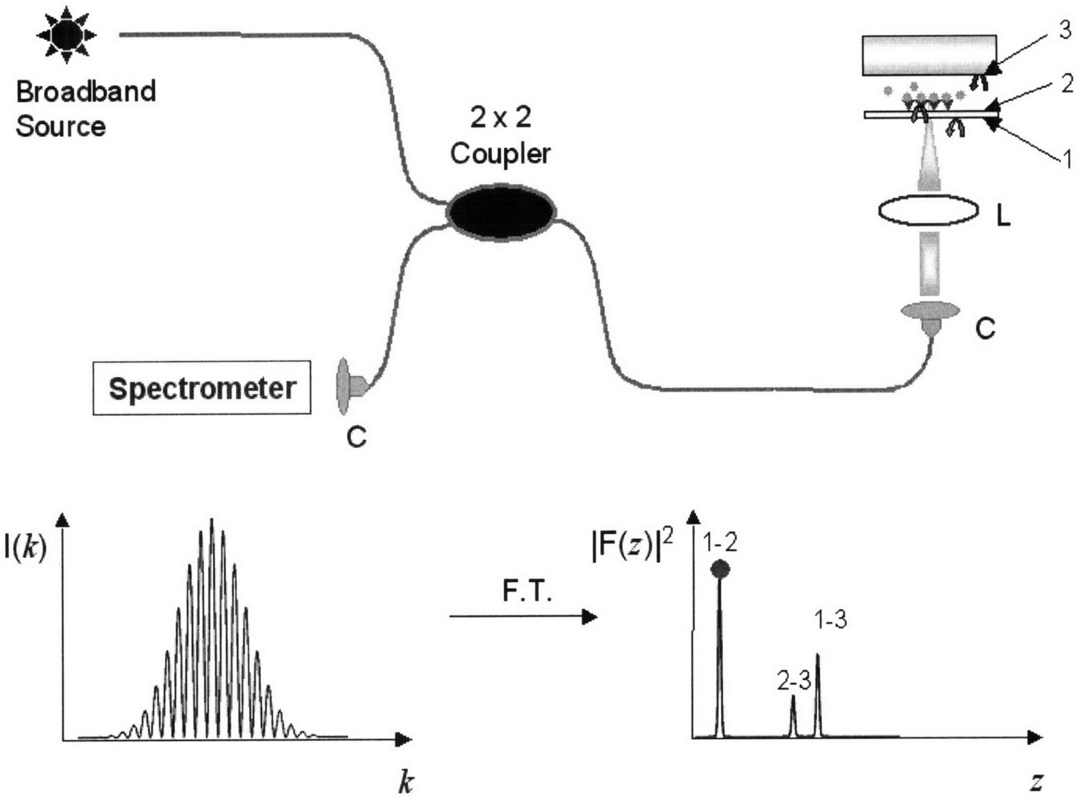

Figure 6.1. Schematic of SD-OCPM sensor. Using the intensity information, the interference signal related to the molecule-coupled sensor surface is identified (marked with a red circle), and the phase of that signal is examined to monitor molecular absorption. The other interference signals denoted by "2-3" and "1-3" are not used since their phase information are also influenced by the reflection from other surfaces and the change in solution refractive index. C: collimator; L: focusing lens.

6.4. SD-OCPM as a real-time molecular sensor

Sub-femtomole detection of SiO2 removal

The capability of the SD-OCPM sensor for detecting traces of small molecules in real-time was first assessed by examining the etching process of a SiO_2 layer by a diluted hydrofluoric (HF) acid solution. SiO_2 can be regarded as a representative of small molecules with a molecular weight (MW) of ~60 Da, which is much less than that of bovine serum albumin (BSA, MW: 60 kDa). For the measurements, a SiO_2-bottom container was filled with de-ionized water, and then a diluted HF solution was introduced into the container to obtain a desired HF concentration. Figure 6.2(a) shows the change of optical thickness at a HF volume concentration of ~0.07%. The sampling rate was 50 Hz. It can be noted that the optical thickness decreases significantly upon injection of the HF solution, giving a measured etch rate of ~51 nm/min. We also examined the etch rate as a function of HF volume concentration (Fig. 6.2(b)). It shows a dramatic etch rate increase when HF concentration is more than 0.02%, which has not been observed in the literature to our knowledge. The noise equivalent optical thickness change (δp) in this experiment was ~0.1 nm at a SNR of 57 dB, whereas the theoretical sensitivity is ~64 pm in air at this SNR. The difference may be due to external disturbances such as vibration during the measurement. Using the weight density of 2.2 g/cm^3 [9] and the refractive index of 1.46 for SiO_2, we estimate the surface density and the optical thickness of one monolayer as $\sim 8\times10^{14}$ cm^{-2} and 0.51 nm, respectively, assuming that a single SiO_2 molecule occupies a cubic volume. The noise-equivalent thickness can then be approximated as ~0.2 layer, which corresponds to ~0.05 fmol on the sensor surface.

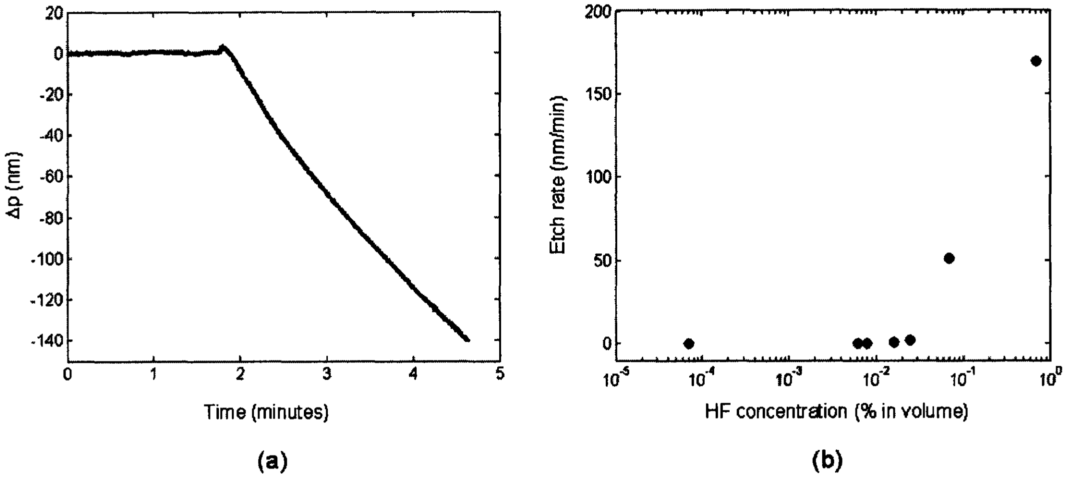

Figure 6.2. Real-time detection of SiO_2 etch by diluted HF solutions. (a): The optical thickness change was measured as a function of time at a HF volume concentration of 0.07%. The etch rate

was measured as ~51 nm/min. (b): The etch rate as a function of HF volume concentration was examined, showing a dramatic increase at more than 0.02% in HF concentration.

Real-time detection of biotin-streptavidin interaction

The SD-OCPM sensor was further applied to real-time detection of protein binding in a microfluidic channel. A single-channel microfluidic device was fabricated from a coverslip and Polydimethylsiloxane (PDMS) based on a standard PDMS casting and bonding techniques [10]. The channel was 100 μm wide, 30 μm deep, and 50 mm long.

The inner channel of the device was functionalized by a low concentration biotinylated BSA solution (bBSA, 250 nM). For the measument, the beam was focused on the top surface of the coverslip, the phase of the interference of light reflected from the top and bottom surfaces of the coverslip was recorded at a sampling rate of 50 Hz. The acquired phase fluctuation was processed by a moving-average filter with a size of 10 points (time constant: 200 msec). Figure 6.3(a) shows the experimental result for the bBSA-activated fluidic channel. Initially, the introduction of buffer solution (phosphate buffered saline, PBS) did not change the optical thickness, but a noticeable change was observed after the streptavidin solution with a concentration of 250 nM flowed through the device. This optical thickness change is due to the binding of streptavidin to the immobilized bBSA layer, and its magnitude was measured as ~1.3 nm at the equilibrium state. The discrepancy between the measured optical thickness and the size of streptavidin (4 ~ 5 nm) as reported in Ref. [11] may be in part accounted by the incomplete surface coverage of bBSA layer over the sensing region. After ~20 minutes, we switched back to PBS, and could observe no signal change, which proves strong binding between bBSA and streptavidin. We also conducted control experiment with a non-activated channel (Fig. 6.3(b)). In this case, the flow of the streptavidin solution with the same concentration did not induce an optical thickness change, demonstrating specific binding affinity of streptavidin to biotin.

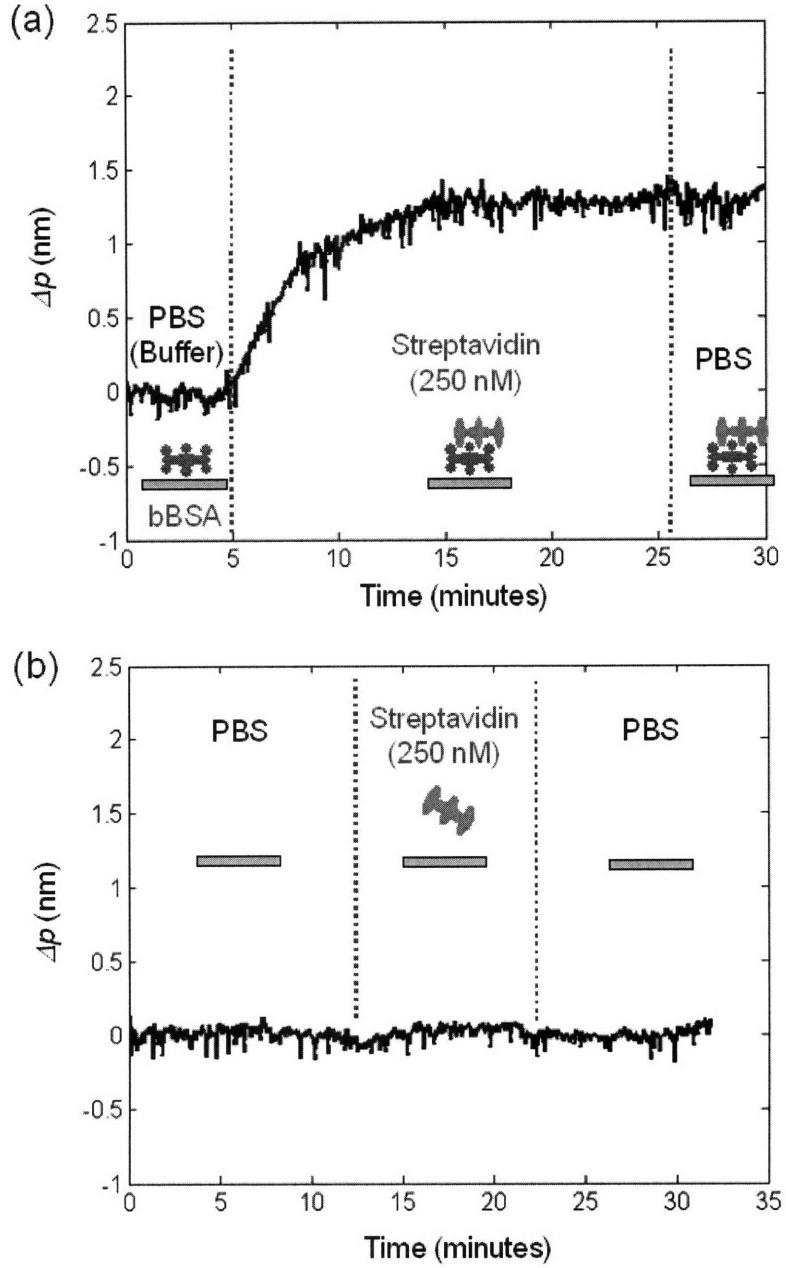

Figure 6.3: Measured bBSA-streptavidin binding in a microfluidic device by the SD-OCR sensor. Using bBSA-activated surface, the introduction of streptavidin (250 nM) led to an optical thickness increase due to the binding of streptavidin to the bBSA layer in the channel. However, in the case of a non-functionalized fluidic channel, even with the same concentration of streptavidin solution, we did not observe a noticeable signal change.

6.5. SD-OCPM as a biochip scanner

The virtue of SD-OCPM molecular sensor is that it can be easily extended to imaging multiplexed protein/DNA arrays by scanning the beam across a sensor surface activated with different protein/DNA patterns. Since its lateral resolution can be in principle diffraction-limited, SD-OCPM can detect hundreds to thousands of activated sites to monitor spatially distributed reactions with high spatial and temporal resolution (Figure 6.4). Moreover, due to its 3D imaging capability, we may envision 3D bioassay with a stack of sensor surfaces, enabling massive 3D protein screening. Including a new active binding site onto a sensor surface can easily allow the detection of new chemical and biological species. This section describes the collaborative work with Prof. Selim Unlu's group at Boston University to explore this exciting opportunity.

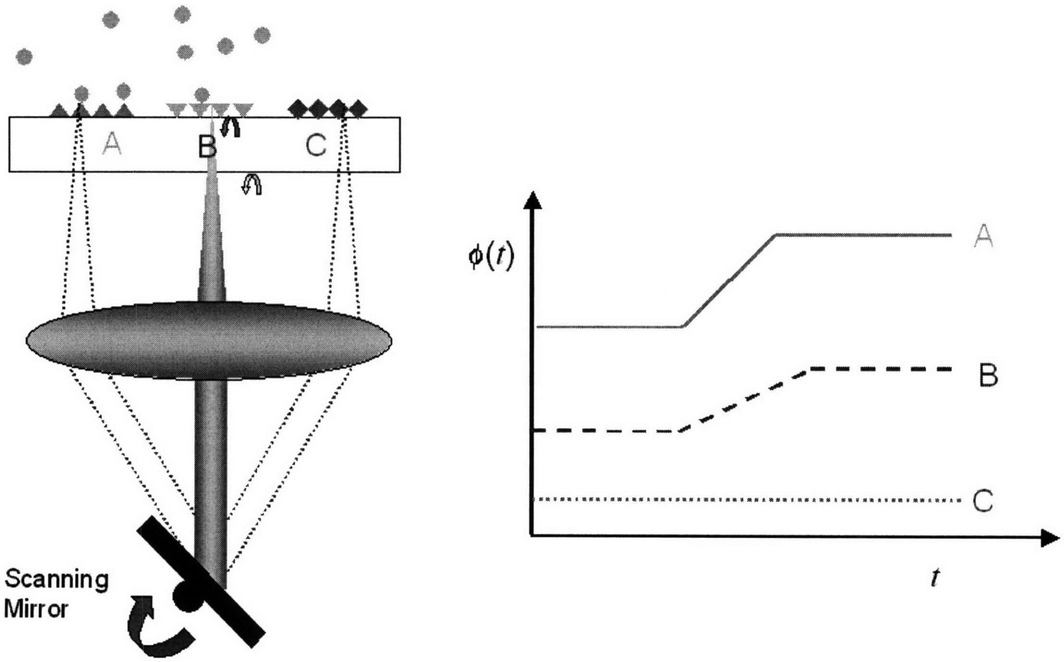

Figure 6.4: Model of SD-OCPM for multi-channel molecular detection. Different probe molecules are patterned onto a sensor surface with small feature, and the probe beam is scanned across the sensor surface to examine molecular binding at different probe regions.

SiO2 square etch pattern array

We first performed phase imaging on a SiO_2 etch pattern array designed and fabricated to model protein array chips. In a typical biochip assay, the analytes bind to the ligands on the surface, and the average signal change over the multiple activated sites is measured for quantitative determination of binding events.

The sample employed was a ~10 μm thick SiO_2 substrate into which 5×5 square patterns were etched. It was prepared by a standard photo-lithographic method. A positive photoresist (S1805) was spun on the SiO_2 substrate of thickness 10 μm, baked for ~1.5 min in the oven, and exposed to UV light under the chromium mask. The mask had 5×5 square patterns inside which small squares were distributed so that the amount of open squares can control the density of depressions. After development, the sample was etched with BOE (Buffered oxide etch - HF) solution, and the little squares in the big square (in the mask) determined the density of depressions on the sample after etching.

Figure 6.5 shows the quantitative image of the model sample acquired by SD-OCPM. For imaging, the beam was focused on the surface where the feature is etched with a measured resolution of 2.5 μm. The image size was 512×512 pixels, and the total acquisition time was ~27 seconds with a pixel integration time of ~4 μsec. The quantity presented in the image is the physical thickness in nanometer, which is obtained by using a refractive index of 1.46 for SiO_2. Note that SD-OCPM visualized the density of depressions clearly, and especially the small square patterns inside the larger square were observed. Based on the quantitative information, 3D surface map was generated as shown in Figure 6.4(b). The average phase delay across the 100×100 pixels was calculated and plotted based on the density of depressions pre-determined from the mask design (Figure 6.5). The 0 % in the density of depression means no etching in the region. The noise-equivalent thickness was estimated by taking the standard deviation in the region with no features, and found as 24 pm. In comparison, the same sample was separately measured by the method developed Prof. Selim Unlu's group, and both results were consistent with a sub-nanometer difference.

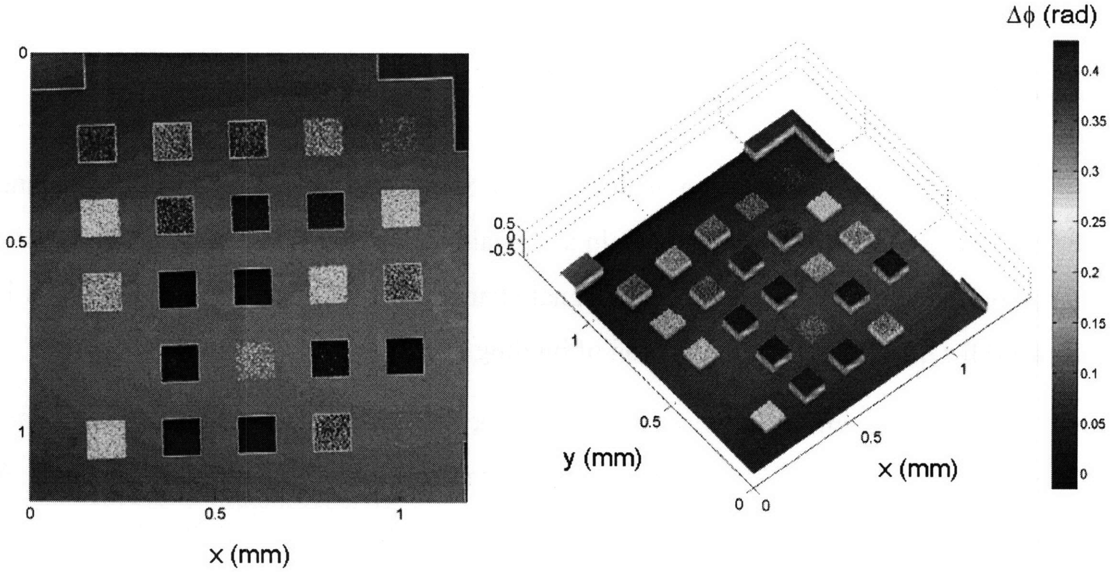

Figure 6.5: SD-OCPM phase image of 5×5 SiO_2 square etch patterns. The etch patterns were provided by Prof. Selim Unlu's group at Boston University to model the protein arrays. The square pattern has a maximum etch depth of ~7 nm and a size of 100 μm × 100 μm.

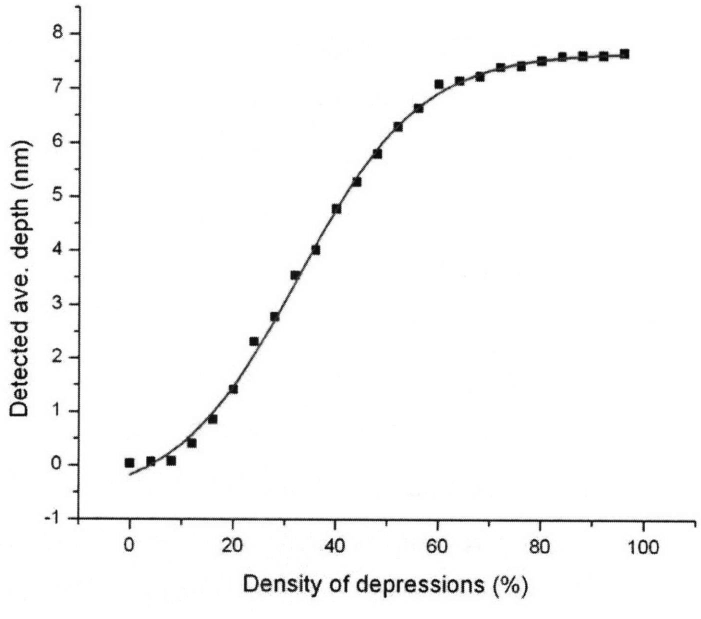

Figure 6.6: SD-OCPM phase image of 5×5 SiO_2 square etch patterns. The etch patterns were provided by Prof. Selim Unlu's group at Boston University to model the protein arrays. The square pattern has a size of 100 μm × 100 μm.

BSA protein pattern array

As an exemplary demonstration of protein chip imaging, an array of BSA patterns on a SiO_2 substrate was imaged by SD-OCPM. The SiO_2 substrate was functionalized with epoxy group for covalent bond of proteins, after which BSA (Sigma-Aldrich Co., >99% pure, 1% BSA (w/v) in PBS, 2.5% glycerol) solution was spotted and bound to the surface. After O/N incubation, the substrate was washed 3× with PBS containing 0.1% Tween-20 (Sigma-Aldrich Co., Mo), 3× with PBS, and 1× with deionized water. The sample was then dried under an inert gas before measurement.

Figure 6.6 shows the quantitative phase image of the BSA array and the phase distribution along the line denoted in the image. It can be noted that the BSA circular features were clearly visible with high contrast. The image seems to exhibit more roughness and noise compared to the previous experiment (Section 6.5.1), which may be accounted for by the chemical treatment of the surface. The average phase delay due to the presence of BSA patterns was measured as ~0.03 rad, which corresponds to ~1.4 nm in physical thickness, with the BSA refractive index of 1.4. The noise-equivalent thickness was estimated by the standard deviation of non-activated region (30 × 30 pixels), and found as ~0.003 rad. The measured SNR was ~ 50 dB.

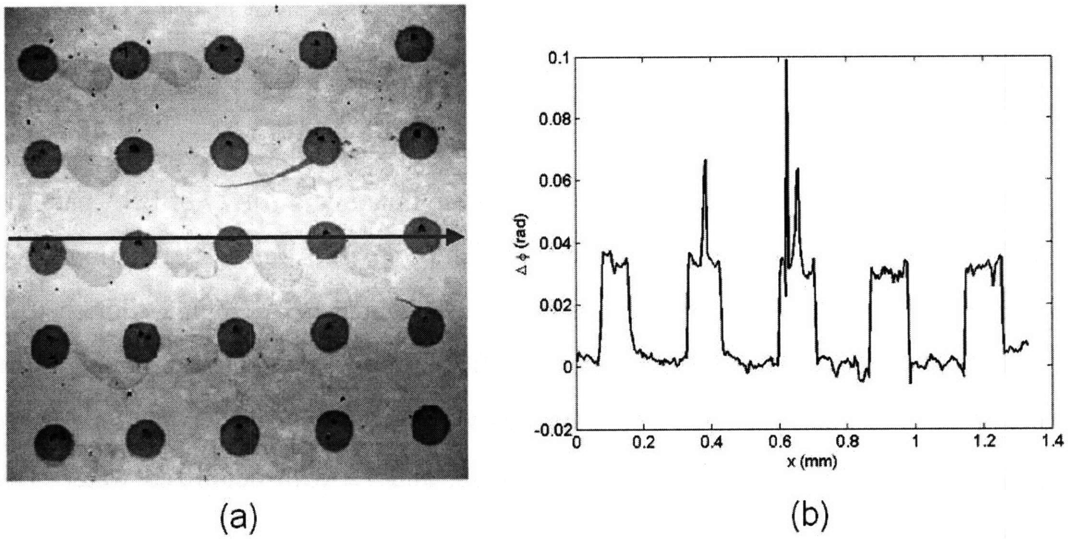

(a) (b)

Figure 6.7: SD-OCPM phase image of a circular BSA pattern on SiO_2 substrate (a), shown with the phase distribution along the direction denoted by the line (b). The average phase change caused by the BSA patterns was measured as ~0.035 radians, while the noise-equivalent phase was ~0.003 radians. The BSA protein array was provided by Prof. Selim Unlu's group at Boston University.

6.6. Summary

We presented SD-OCPM as an optical method for highly sensitive molecular recognition. Using the capability of sensor surface identification by use of the coherence gating and high phase sensitivity provided by SD-OCPM interferometer, SD-OCPM measures the phase alteration caused by molecular absorption or desorption without the effect of other surfaces and the solution concentration fluctuation.

In order to demonstrate its sensitivity and feasibility as a real-time molecular sensor, the SD-OCPM sensor was utilized to measure the etch process of SiO_2 molecules, and demonstrated sub-femtomole detection sensitivity for SiO_2 molecules. We also applied SD-OCPM to detect the binding of biotin-streptavidin in a micro-fluidic device. SD-OCPM could detect non-reversible biotin-streptavidin binding, and the validity of the measurement was confirmed by a control experiment.

Further, we explored its potential as molecular array scanner by use of its intrinsic imaging capability. SD-OCPM imaged a 5 × 5 square etch pattern on a SiO_2 substrate, and demonstrated its capability in imaging nanometer-level features on the substrate with a precision of 24 pm (calculated over 50×50 pixels). SD-OCPM was further utilized to image BSA patterns on the substrate. It visualized the nanometer-level BSA features with high contrast.

With the help of multiplexed protein arrays with different probe molecules, SD-OCPM should be able to serve as a powerful bioassay tool.

6.7. Reference

1. B.H. Park, M.C. Pierce, B. Cense, S.-H. Yun, M. Mujat, G. Tearney, B. Bouma, and J.F.de Boer, "*Real-time fiber-based multi-functional spectral-domain optical coherence tomography at 1.3 μm,*" Optics Express. **13,** 3931-3944 (2005).

2. J. Homola, S.S. Yee, and G. Gauglitz, "*Surface plasmon resonance sensors: review,*" Sensors and Actuators B. **54,** 3-15 (1999).

3. F. Vollmer, D. Braun, A. Libchaber, M. Khoshsima, I. Teraoka, and S. Arnold, "*Protein detection by optical shift of a resonant microcavity,*" Applied Physics Letters. **80,** 4057-4059 (2002).

4. E.A. Swanson, D. Huang, M.R. Hee, J.G. Fujimoto, C.P. Lin, and C.A. Puliafito, "*High-speed optical coherence domain reflectometry,*" Optics Letters. **17,** 151-153 (1992).

5. J. Piehler, A. Brecht, and G. Gauglitz, "*Affinity detection of low molecular weight analytes,*" Analytic Chemistry. **68,** 139-143 (1996).

6. A. Brandenburg, R. Krauter, C. Knzel, M. Stefan, and H. Schulte, "*Interferometric sensor for detection of surface-bound bioreactions,*" Applied Optics. **39,** 6396-6405 (2000).

7. L. Peng, M.M. Varma, F.E. Regnier, and D.D. Nolte, "*Adaptive optical biocompact disk for molecular recognition,*" Applied Physics Letters. **86,** 183902 (2005).

8. M. Zhao, D. Nolte, W. Cho, F. Regnier, M. Varma, G. Lawrence, and J. Pasqua, "*High-speed interferometric detection of label-free immunoassays on the biologial compact disc,*" Clinical Chemistry. **52,** 2135-2140 (2006).

9. D.R. Lide, ed. *Handbook of Chemistry and Physics*. 2005, CRC Press.

10. G.M. Whitesides, "*The origins and the future of microfluidics,*" Nature. **442,** 368-373 (2006).

11. A. Arakaki, S. Hideshima, T. Nakagawa, D. Niwa, T. Tanaka, T. Matsunaga, and T. Osaka, "*Detection of biomolecular interaction between biotin and streptavidin on a self-assembled monolayer using magnetic nanoparticles,*" Biotechnology and Bioengineering. **88,** 543-546 (2004).

Chapter 7:

Summary and Future Directions

7.1. Dissertation summary

In this thesis, we have introduced a novel quantitative phase imaging modality, referred to as spectral-domain optical coherence phase microscopy (SD-OCPM). The method is based on a common-path SD-OCT interferometer, and is capable of producing amplitude and quantitative phase images of biological specimens with high sensitivity. To summarize our accomplishments in this thesis:

In Chapter 2, we presented the details about the design, implementation, and the performance characteristics of current SD-OCPM. Current SD-OCPM implementation is based on a fiber-based SD-OCT interferometer, and exhibited diffraction-limited spatial resolution and sub-nanometer path-length sensitivity for a good reflector. We demonstrated its quantitative phase imaging capability by imaging calibrated phase target and fixed and live cellular specimens.

Chapter 3 is devoted to the analysis on the factors that contribute to the phase stability of SD-OCPM. We first examined the noise components in SD-OCPM interferometer, and proved that its operation is shot-noise limited. Based on this finding, the phase probability density function was derived and experimentally confirmed. The phase stability is an explicit function of SNR, so it is very important to obtain high SNR to achieve high phase sensitivity. The noise contributions due to the scanners were also investigated. The transverse scanning of the beam reduces the effective lateral resolution and SNR, whereas the axial motion jitter of piezo-electric transducer induced phase changes in the measurement. For high-resolution 3D imaging, it necessities high-spatial resolution, but it puts stricter requirements on the performance of the scanners.

In order to facilitate understanding of SD-OCPM images and to provide complementary information for functional studies, a multi-photon fluorescence imaging modality was combined with SD-OCPM (Chapter 4). As in Chapter 2, we described the detailed information about the implementation and performance characteristics of the multi-modal imaging method, and demonstrated simultaneous imaging capability by showing the images recorded on fixed and stained muntjac skin fibroblast cells.

We utilized SD-OCPM to conduct quantitative studies in the area of cellular and molecular biology.

In Chapter 5, quantitative studies on intracellular dynamics by SD-OCPM were presented. Based on the high sensitivity to localized amplitude and phase fluctuations inside the cellular specimen, we performed temporal autocorrelation analysis and observed the existence of two different regimes in intracellular dynamics. We further investigated the change in intracellular dynamics of human ovarian cancer cells due to ATP-depletion and introduction of an anti-cancer drug, Colchicine. In both studies, we found the reduction of dynamic characteristics inside the cells, confirming that our measurement reflects ATP induced dynamics as well as organelle transport along the microtubules.

Based on the optical sectioning capability of SD-OCPM, quantitative phase imaging was performed to examine slow dynamics of living cells. Through time-lapsed imaging and spectral analysis on the cellular dynamics, we observed the existence of dynamic and independent sub-domains inside the cells that fluctuate at various dominant frequencies with different frequency contents and magnitudes.

Chapter 6 describes an application of SD-OCPM as a molecular sensing platform. The method is based on the fact that phase varies as analyte molecules bind to the immobilized probe molecules at the sensing surface and SD-OCPM can measure small phase alteration at any surface with high sensitivity. We have measured non-reversible binding of streptavidin on a biotin-activated substrate in a micro-fluidic device.

Moreover, SD-OCPM was extended to image protein array chips, demonstrating its potential as a multiplexed protein array scanner.

7.2. Future directions

SD-OCPM is a highly sensitive imaging method that can provide a unique platform for quantitative studies in cellular and molecular biology. Indeed, there are numerous scientific questions that SD-OCPM can potentially help answer, and there are still many aspects to improve in terms of instrumentation and performance.

7.2.1. Speeding up SD-OCPM

At present, we are working on a next generation SD-OCPM equipped with a faster data acquisition system. Our main limitation in terms of the speed of acquisition is its slow data transfer rate to the hard disk. With the maximum line rate of current line scan camera, the data transfer rate is expected to be ~120 MB/sec, which the current acquisition system cannot support. Recently, a new computer with RAID controller has arrived, and expects to sustain the transfer rate more than 250 MB/sec. With this new system completed, the frame rate is expected to be ~0.4 frame/seconds. Further improvement can be realized either by a faster line scan camera [1] or by using SD-OCPM implementation based on wavelength-swept laser sources. Conventional wavelength-swept lasers have poor phase stability due to the poor repeatability of the mechanical motion of the tunable filter, and the amplified spontaneous emission background of the gain medium [2]. However, recently, picometer-level displacement sensitivity was demonstrated by using Fourier domain mode-locked lasers at up to 370 kHz A-line rate [3, 4]. With this line rate, the frame rate becomes 5 frames/second, which enables particle tracking such as lipids inside the cells.

7.2.2. Single source multi-modal imaging

Quantitative phase imaging techniques such as SD-OCPM can be more attractive in combination with other imaging modalities such as fluorescence microscopy. Even though we demonstrated simultaneous quantitative phase and multi-photon fluorescence imaging, the use of separate light sources required a co-registration procedure in the post image processing. Moreover, with the current setup, it may be difficult to detect and co-register the fast dynamics at a single location in the specimen because two probe beams may not overlap in a three-dimensional space. In this respect, the use of a single source for simultaneous OCPM and fluorescence imaging is desirable.

With the single source multi-modal imaging method, one of the applications of great interest is to examine and interrogate neural action potential propagation optically. Akkin [4, 5] and other researchers [6, 7] have demonstrated the measurement of nanometer-level transient phase fluctuations of the nerve cellular membrane during the action potential propagation. However, optical measurement of this functional activity is still at the early stage, and so requires verification with other methods such as electric current measurement by placing electrode in the nerve chamber. Moreover, it is unclear that the phase change is due to the physical displacement or the concentration variation inside the specimen. The combined quantitative phase and fluorescence imaging technique can be a method of choice to probe this process. For instance, calcium ions bind to a fluorescent probe such as Fura-2, Fluo-3 or Calcium Green, and the change of ion concentration leads to the change in the fluorescence intensity. Therefore, focusing the probe beam on a region of interest in the sample, simultaneous imaging and interrogation of neural functional activity can be done since SD-OCPM provides an optical phase change during the action potential propagation, whereas fluorescence channel presents the change in the ion concentration in the probe region. With the photon-counting mode, it is also possible to quantify the concentration inside the probe volume (or focal volume) employing the concept of Fluorescence Correlation Spectroscopy [8].

7.2.3. Contrast enhancement using highly scattering nanoparticles

While SD-OCPM could measure extra- and intracellular dynamics without exogenous contrast agents, the sensitivity to the structural variation is still limited by a low signal-to-noise ratio, typically in the range of 10 dB ~ 20 dB. One approach to the sensitivity improvement is to use contrast agents that exhibit high scattering at the wavelengths of use. For instance, there have been remarkable advances in nano-particle fabrication. The nano-particles are very small and do not have problems such as photo bleaching in fluorescent molecules, but can be engineered to bind to particular structures with high scattering potential [9, 10]. Therefore, with the help of nano-particles, it should be possible to measure structural variation on the scale of sub-cellular structures such as protein motors and microfilaments inside the cell with high sensitivity.

Finishing up this thesis, we feel that this is just the beginning of SD-OCPM. Based on the plethora of information such as spectroscopic amplitude and phase distribution, together with the optical sectioning capability, there are numerous applications where SD-OCPM can be utilized to investigate quantitatively. With the improvement in performance along with the demonstration of the possible applications suggested above, SD-OCPM is believed to stand up as a tool of choice for quantitative analysis and imaging.

7.3. Reference

1. Y. Zhang, B. Cense, J. Rha, R.S. Jonnal, W. Gao, R.J. Zawadzki, J.S. Werner, S. Jones, S. Olivier, and D.T. Miller, "*High-speed volumetric imaging of cone photoreceptors with adaptive optics spectral-domain optical coherence tomography,*" Optics Express. **14,** 4380-4394 (2006).

2. R. Huber, M. Wojtkowski, K. Taira, J.G. Fujimoto, and K. Hsu, "*Amplified, frequency swept lasers for frequency domain reflectometry and OCT imaging: design and scaling principles,*" Optics Express. **13,** 3513-3528 (2005).

3. R. Huber, M. Wojtkowski, and J.G. Fujimoto, "*Fourier Domain Mode Locking (FDML): A new laser operating regime and applications for optical coherence tomography,*" Optics Express. **14,** 3225-3237 (2006).

4. D.C. Adler, R. Huber, and J.G. Fujimoto, "*Phase-sensitivie optical coherence tomography at up to 370,000 lines per second using buffered Fourier domain mode-locked lasers,*" Optics Letters. **32,** 626-628 (2007).

5. T. Akkin, C. Joo, and J.F.de Boer, "*Depth-Resolved Measurement of Transient Structural Changes during Action Potential Propagation,*" Biophysical Journal. **93,** 1347-1353 (2007).

6. C. Fang-Yen, M.C. Chu, H.S. Seung, R.R. Dasari, and M.S. Feld, "*Noncontact measurement of nerve displacement during action potential with a dual-beam low-coherence interferometer,*" Optics Letters. **29,** 2028-2030 (2004).

7. C. Fang-Yen, S. Oh, Y. Park, W. Choi, S. Song, H.S. Seung, R.R. Dasari, and M.S. Feld, "*Imaging voltage-dependent cell motions with heterodyne Mach-Zehnder phase microscopy,*" Optics Letters. **32,** 1572-1574 (2007).

8. D. Magde, E. Elson, and W.W. Webb, "*Thermodynamic Fluctuations in a Reacting System—Measurement by Fluorescence Correlation Spectroscopy* " Physical Review Letters. **29,** 705 - 708 (1972).

9. A.V. Failla, S. Jäger, T. Züchner, M. Steiner, and A.J. Meixner, "*Topology measurements of metal nanoparticles with 1 nm accuracy by Confocal Interference Scattering Microscopy,*" Optics Express. **15,** 8532-8542 (2007).

10. J.S. Aaron, J. Oh, T.A. Larson, S. Kumar, T.E. Milner, and K.V. Sokolov, "*Increased optical contrast in imaging of epidermal growth factor receptor using magnetically actuated hybrid gold/iron oxide nanoparticles,*" Optics Express. **14,** 12930-12943 (2006).